Miniaturised, High-Reliability Lasers for Quantum Technologies

Rachel Cannon

A thesis presented for the degree of

Doctor of Engineering

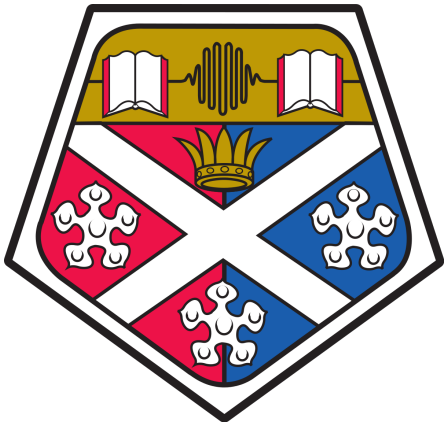

Department of Physics

University of Strathclyde

2024

Abstract

This thesis describes the experimental characterisation of the Flame laser module within the context of quantum technologies. Alter UK have developed a compact module designed for frequency stabilisation of a laser, measuring 6 cm x 4 cm x 1.5 cm. The Flame module employs an internal saturation absorption spectroscopy setup to lock a distributed Bragg reflector laser diode to an integrated alkali vapour source. This eliminates the necessity for external optical components specifically in the laser locking process, resulting in a reduction of the experimental footprint. The Flame's compact design makes it particularly well-suited for the advancement of deployable atomic sensors, aligning with the industry drive towards more efficient and portable quantum technology solutions.

We explore a device's frequency stability, revealing a σ_τ value of 5×10^{-12} at a 1 second integration time, which verified the module's suitability for laser cooling applications. The Flame was integrated into a portable cold-atom system to showcase its practicality and durability outside a laboratory setting. We investigate the module's adaptability, utilising 780 nm and 852 nm devices to fabricate two respective optically pumped magnetometers. The first system exhibited promise as a co-magnetometer, while the second proved more suitable for portable magnetic sensing applications, delivering a sensitivity of 3 $pT/\sqrt{Hz}$.

Acknowledgements

Let me begin by giving thanks to the many people who made this thesis and my EngD journey possible. To my academic supervisors, Erling Riis and Paul Griffin, I am so thankful. I feel privileged to have had such supportive and approachable supervisors. The drive, dedication and expertise of you both is unmatched. I am deeply grateful to my industrial supervisor, Una Marvet, who is sadly no longer with us. She was incredibly encouraging every step of the way and it was a true honour to have known her.

I had the pleasure during my EngD to work with some really great scientists and people, too many to be named individually. Special thanks to Sean Dyer, with whom I collaborated on the three-cornered hat experiment. Thank you to Oliver Burrow, who worked with me on the portable cold atom system - and provided lots of other help along the way! Deserving of a shout-out also is Marcin Mrozowski who designed the Flame's trans-impedance amplifier used in this thesis. Thank you Douglas Bremner for answering all of my Flame related questions. It was great to work with you, and even greater sharing the odd drink!

To my family - my mum, dad and sister. Thank you for your endless support and love and telling me it would all eventually be worth it.

Finally, thank you Allan for everything - I loved sharing this journey with you and I am so excited for our future.

Contents

Acronyms

AC alternating current

AOM acousto-optic modulator

AlGaAs aluminium gallium arsenide

BEC Bose-Einstein Condensate

COTS commercial off the shelf

DAQ data acquisition

DAVLL dichroic atomic vapour laser locking

DBR distributed Bragg reflector

DC direct current

DFB distributed feedback

DFT discrete Fourier transform

DLC diode-laser controller

ECDL extended cavity diode laser

EOM electro-optic modulator

EQOP Experimental Quantum Optics and Photonics

FAC fast-axis collimator

FC fibre coupling

FID free induction decay

FM frequency modulation

FPGA field-programmable gate array

FWHM full-width half-maximum

GPS Global Positioning System

GRIN gradient-index

gMOT grating magneto-optical trap

GUI guided user interface

HW half-width

HWP half wave-plate

IEC international electrotechnical commission

LIA lock-in amplifier

LPF low-pass filter

MEMS micro-electro mechanical systems

MOT magneto-optical trap

ND neutral density

N_2 nitrogen

OI optical isolator

OD optical density

OPM optically pumped magnetometer

PBS polarising beam-splitter

PCB printed circuit board

PID proportional-integral-derivative

QWP quarter wave-plate

RF radio-frequency

RSD root-spectral density

SAC slow-axis collimator

SAS saturation absorption spectroscopy

SERF spin-exchange relaxation-free

SMA SubMiniature version A

SNR signal to noise ratio

SWaP size, weight and power

TEC thermoelectric cooler

TIA trans-impedance amplifier

TEM transverse-electromagnetic mode

TS telescope

TTL time-to-live

UHV ultra-high vacuum

UoS University of Strathclyde

USB universal serial bus

VCSEL vertical-cavity surface-emitting laser

VCO voltage controlled oscillator

ZIF zero insertion force

Chapter 1

Introduction

The invention of the laser in 1960 [1] welcomed a rapid evolution in atomic physics. Laser-light generation marked a substantial improvement over the previously developed discharge lamps, which lacked the vital attributes of coherence and tunability [2]. The ensuing decades witnessed revolutionary progress from an initial proposal that laser light could possibly exert a force to decelerate atoms in the 1970s [3], to experimentally achieving the cooling and trapping of atoms in the 1980s by several research institutes [4–7]. Research capabilities were therefore transformed by the laser and its ability to manipulate and interrogate atoms.

To this day, a considerable amount of funding and research is directed at developing atomic sensors for devices in atom interferometry, atomic clocks and optically pumped magnetometers. These devices have applications in gradiometry [8], gravimetry [9], rotation sensing [10, 11] and precision timing [12]. To capitalise fully on their sensing potential, these technologies must be transported from the laboratory to real-world environments. This involves massively reducing the size, weight and power (SWaP) of the setups and, therefore, the individual components with which they are comprised. Research in the past decade has geared towards this particular goal. This has encompassed addressing the size of lasers, optics [13, 14], vapour cells [15, 16] and vacuum systems [17, 18].

The introduction of semiconductor laser diodes [19,20] paved the way for inexpensive and widely accessible laser sources. The capabilities of diode lasers in the last few

decades alone have advanced rapidly, with typical output powers of around 10 mW in the 1990s [21], to kWs in the 2010s [22]. The substantial progress made in atomic physics during the 1900s could be advanced with diode lasers which are considerably compact devices.

The main challenge in integrating the standard laser diode into application areas in atomic physics, specifically those employing cold atoms, is the stringent set of characteristics that the laser must possess. A requisite for the laser linewidth is that the laser be much narrower than the natural linewidth of the atoms being probed. For rubidium the natural linewidth is around 6 MHz, meaning a typical laser linewidth of $<$1 MHz is essential [23,24]. Additionally, the frequency stability over time should stay within a few MHz [25] for suitability in experiments which are to be operated continuously. Optical feedback methods ensure a laser diode operates at a single frequency while reducing its inherent linewidth. However, laser diodes operating as "free-running" still exhibit linewidths rendering them unsuitable for precision measurements involving laser cooled atoms. Additionally, their frequency inevitably drifts through external factors. Active laser frequency stabilisation is therefore essential, with atomic transitions deemed as exemplary candidates in laser stabilisation schemes attributed to being extremely stable frequency references. Laser frequency stabilisation techniques based on atomic vapour cells are the logical choice for lasers which are to be used in quantum sensors and are therefore the most commonly employed method.

Saturation absorption spectroscopy is a commonly used laser stabilisation method, requiring a limited number of components and space to operate. However, setups within a laboratory can still occupy a considerable amount of space when implementing. It prompts the consideration of employing compact laser sources, such as laser diodes, when external and large setups are required for the laser to meet the specifications of stability and linewidth. This point effectively leads us to the purpose of this thesis, and the introduction of the Flame laser module.

Alter UK have fabricated a module capable of frequency stabilising a diode laser while occupying only 6 cm x 4 cm x 1.5 cm in volume. The Flame module has an internal configuration of saturation absorption spectroscopy to lock the laser to an integrated

alkali vapour source. To achieve this, the package includes a temperature stabilised distributed Bragg reflector laser, a glass-blown vapour cell, internal photodiode and accompanying optics, and outputs over 150 mW of optical power. This eliminates any need for external optical components for laser locking, leading to a huge reduction in the experimental foot-print. This is consistent with the field goals of reducing the SWaP of components, beginning with the laser itself.

There are, however, applications in quantum technology that do not necessarily require frequency stabilised lasers. Optically pumped magnetometers (OPMs) which employ vapour cells with the inclusion of a buffer gas have less demanding requirements for the laser used, than previously mentioned cold-atom experiments. The buffer gas is added to mitigate the spin destruction of the atoms, at the cost of broadening and frequency shifting the atomic optical resonances. Manipulating and probing the atomic states can therefore be achieved with free-running, larger-linewidth lasers, in the range of 100 MHz [26] for OPMs operating with cells containing buffer gas. The Flame module's compactness and ample optical power, however, make it an ideal candidate for use in portable OPMs, where a high intensity laser is beneficial for spin-polarising more atoms and augmenting the overall detected magnetic measurement signal. This makes the Flame an attractive and versatile laser product, suitable for integration with other quantum technology components in the development of compact and deployable atomic sensors.

Alternative, state-of-the-art laser systems commonly used in quantum technologies include frequency-doubled telecom lasers [27–31]. These systems are highly popular due to the well-established maturity of fibre-components in the telecom C-band range (1530-1565 nm). This is effective in meeting the deployment goals in the field as fibre components help ensure setups remain compact and robust. These telecom lasers are frequency doubled to address alkali atoms such as rubidium and potassium, atomic species used widely in laser cooling experiments. However, this technology begins to falter when alternative alkali species, such as caesium, are required, as they necessitate seed lasers in the 1700 nm range. Additionally, these systems typically require optical amplification, which are widely available but expensive components. Alter's Flame

lasers, on the other hand, operate directly at the resonant wavelengths for a given atomic species. They deliver high optical power (>150 mW), thereby eliminating the need for additional optical amplification and components such as frequency doubling, non-linear crystals. This thesis details two Flame laser modules, one operating at 780 nm for use with rubidium atoms and the other at 852 nm for caesium.

The work in this thesis was conducted in the Experimental Quantum Optics and Photonics (EQOP) group at the University of Strathclyde using Flame lasers fabricated by Alter UK engineers. This thesis outlines Flame modules in various experimental setups to demonstrate the efficacy of the laser product as a whole. The experiments undertaken in this project delve into applications within the realm of quantum technologies such as laser cooling and optically pumped magnetometers. The theoretical discussions in each chapter are therefore intentionally concise, given the diverse range of topics and applications covered. Each chapter presents only the most pertinent information for basic understanding of the topics introduced and for the overall brevity of the thesis. The aim is to provide the basic understanding enabling the reader to appreciate the technical requirements for the application and how that translates into performance specifications for the laser and associated optics.

Chapter 2 introduces the operation of semiconductor lasers and their role within quantum optics. We explore atom-light interactions and their relevance in laser frequency stabilisation methods, specifically for saturation absorption spectroscopy. The chapter concludes with an overview of the Flame laser module. This includes the laser's operation and design, the future considerations and a discussion of similar devices within the field. Chapter 3 describes how overlapping Allan deviations are used to determine the frequency stability of a laser. We introduce a 'three-cornered hat' experiment in order to determine the individual stability of the Flame laser. The chapter concludes by comparing the Flame's stability when locked to an external spectroscopy setup, to the setup within its own package. Chapter 4 integrates a Flame laser with a commercial compact vacuum package to exhibit a field-deployable cold atom system. The system build, design considerations and challenges are presented. Lastly, Chapter 5, incorporates Flame modules in optically pumped magnetometer sensors. Two sepa-

rate magnetometer sensors are introduced, one employing natural rubidium atoms and the other caesium.

Chapter 2

The Flame

2.1 Semiconductor Lasers

Semiconductor lasers at their core work by electron-hole recombination in a p-n junction. Figure 2.1 gives a simple illustration of their structure and operation. The p-side of the junction accommodates an excess of holes, while the n-side possesses an excess of electrons. Metallic contacts are attached to each side of the junction. By applying a forward-bias current as depicted in Figure 2.1a, the holes and electrons will be pulled towards one another within the junction. The recombination of holes and electrons in the active region releases photons whose energy roughly matches that of the band-gap energy. Specific emission wavelengths for diode lasers are therefore achieved using materials with appropriate band-gaps. As the forward current is further increased, this process is intensified and a progressive number of photons are released. For the light to be amplified and lasing to occur, the two edges parallel to the p-n junction are cleaved. This creates an optical resonator and is what differentiates a diode laser from a typical p-n junction diode [32].

The resonator provides optical feedback and has a certain loss associated with it. When the gain of the light within the cavity exceeds the loss, lasing occurs and is sustained through stimulated emission. The light is confined in the direction perpendicular to the junction plane (transverse direction) by effectively turning the active region into a waveguide. This is fulfilled by ensuring that the active region has a higher refractive

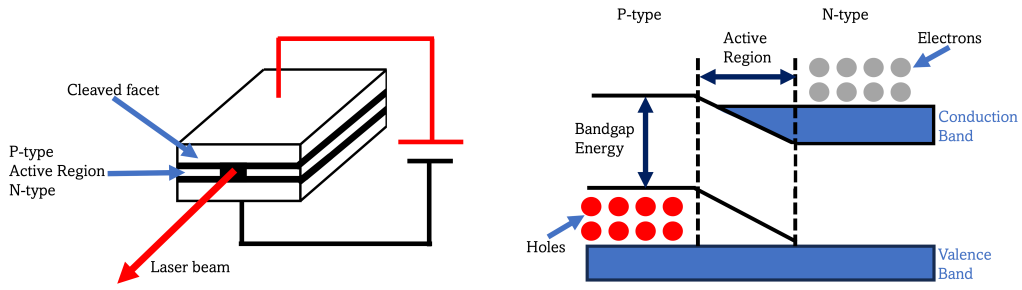

(a) (b)

Figure 2.1: (a) Illustration of a diode laser chip with a forward-biased current being applied. The lasing occurs in the active region where recombination of electrons and holes unfolds as the current applied is increased. The cleaved facet creates the laser cavity for amplification of the emitted light. (b) The p-n junction revealing the excess of holes and electrons on each side of the p-n junction. The emission wavelength of the created photons closely corresponds to the band-gap energy of the semiconductor material.

index than the cladding layers, constraining the light from escaping to the p-n regions.

Typically, a suitable semiconductor for a laser would have a direct band-gap configuration. Figure 2.2 shows a plot of commonly used semiconductor materials, their lattice constants and corresponding wavelengths. Substrate materials, additionally shown on the right hand y-axis, are paired with materials that have similar lattice constants to form alloys, which are then used to create laser diode devices. The tuning of the laser diode emission wavelength is then dependent on the ratio of the two materials in the fabrication process of the alloy material. For example, many laser diode devices operating in the visible wavelength spectrum going into infrared consist of aluminium gallium arsenide (AlGaAs). It can be seen on Figure 2.2 that AlAs and GaAs are lattice matched, with their associated wavelengths spanning from around 600 nm to 900 nm.

Lasing begins after a specific threshold current is applied to the diode. The output power then increases linearly with current, with ideally one photon being produced for each applied electron. Figure 2.3 shows a typical output power versus injection current plot for a laser diode, where it becomes apparent that following from the laser threshold there is roughly a mW increase in light for each mA applied. The threshold current is governed by the losses within the optical resonator, with the output coupling

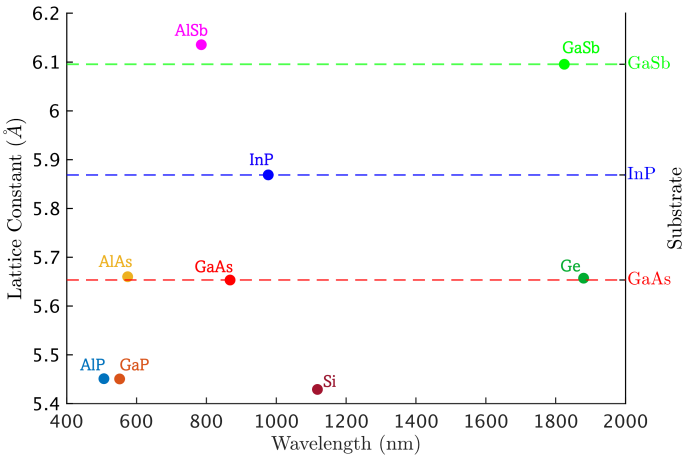

Figure 2.2: Various semiconductor materials are shown with their lattice constants and associated wavelengths. Additionally shown are commonly used semiconductor substrate materials, where lattice matching of a substrate and other semiconductor materials is crucial in fabricating laser diodes of varying emission wavelengths. The material information for plotting is from [33].

contributing as a significant loss. Typically, high-power laser diodes exhibit higher losses within the cavity which consequently increases the amount of current needed to reach lasing. This is to ensure that the laser intensity inside the cavity is not too high, which could damage the optical facet leading to laser failure. The reflectivity of the end facets are therefore important considerations when fabricating laser diodes.

A laser diode operating just above threshold is typically multi-mode, and as the current is increased further one specific mode prevails. The frequency of the laser is tuned through current injection and junction temperature variations. Temperature changes adjust the band-gap energy of the p-n junction, therefore changing the emitted photon energy. As the injection current increases, it leads to a higher carrier concentration in the active region. This, in turn, causes a modification in the refractive index of the material. These alterations to the refractive index directly impact the cavity length, thereby influencing the laser wavelength. The lasing wavelength is defined as,

$$\lambda_m = \frac{2nL}{m} \tag{2.1}$$

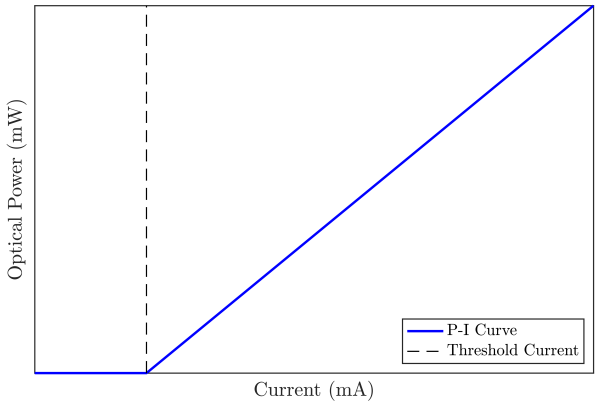

Figure 2.3: A theoretical P-I curve for a laser diode. Lasing occurs at applied currents above the threshold current.

where λ_m is wavelength of the m^{th} mode in the cavity of optical length nL. A slower effect on the refractive index also occurs in the active region with the change in temperature from the injection current and ambient temperature.

The free running linewidth of an unmodified, single-frequency diode can be as wide 100 MHz [34]. Although not a limitation for applications such as the lasers used in compact disc players, precision experiments which depend on extremely narrow-linewidths become unattainable. Specifically, for the applications discussed in this thesis the laser needs to be single-frequency, narrow-band, stable and to the order of 100s of kHz. Modifications of laser diode chips are therefore essential to overcome some of the sensitivities which stand-alone laser diodes are susceptible to.

The Schawlow-Townes Equation [35] states that there is a fundamental limit to a laser's linewidth relating to the quantum nature of light,

$$\Delta\nu = \frac{\pi h\nu \Delta{\nu_c}^2}{P} n_{sp} \tag{2.2}$$

where $h\nu$ is the photon energy in a mode, P is the power in the mode, $\Delta\nu_c$ is the bandwidth of the laser cavity and n_{sp} is the ratio of spontaneous to stimulated emission [36]. The Schawlow-Townes equation, however, it not suitable for semiconductor laser diodes. Semiconductor lasers have much larger fundamental linewidths than their

solid-state counterparts due to the refractive index variation of the semiconductor material with carrier density. This detrimentally broadens the linewidth as it couples in additional intensity and phase noise to the laser output. A modification of Equation 2.2 was proposed by Henry [37], introducing a linewidth enhancement factor α,

$$\Delta\nu = \frac{\pi h\nu {\Delta\nu_c}^2}{P} n_{sp}(1+\alpha^2). \tag{2.3}$$

Typical values of α are calculated to be between 2 and 5 [38–40], limiting how narrow a semiconductor's linewidth can be by a factor of 5 to 26 of the Schawlow-Townes limit. The dependence of a semiconductor's frequency on the applied current is therefore a limitation in achieving a narrow-linewidth laser.

The bandwidth of the laser cavity, $\Delta\nu_c$, is correlated with the lifetime of a photon in the cavity, with $\nu_c = 1/2\pi\tau_c$. The lifetime of the photon increases remarkably at longer cavity lengths [41], with the cavity length as well as the mirror reflectivity therefore having a consequence on the overall linewidth. This is intuitive when considering processes such as spontaneous emission. During spontaneous emission, photons of random phase are added to the lasing, broadening the frequency spectra. Increasing the cavity length or increasing the mirror reflectivity will therefore constitute to the spontaneously emitting photons having less significance as they result in more stimulated emission within the cavity. Therefore, a balance in mirror reflectivity must be found to ensure that the power inside the cavity is kept at safe values to protect the laser diode, as well as a photon's lifetime being prolonged for as long as possible. Disturbances to the laser light can additionally prevail from external factors, such as mechanical vibrations. The frequency of a laser is intrinsically related to the integer number of wavelengths between the mirrors which make up the cavity, as discussed. Mechanical perturbations which cause the cavity mirrors to move consequently affect the frequency. This is more impactful the shorter the cavity as any displacement of the mirrors will constitute a larger fraction of the length, resulting in a broadened frequency output.

Increasing the length of a laser cavity make it less sensitive to these effects. Implementation of frequency selective devices, such gratings, can simultaneously guarantee

the attainment of the required wavelength of light whilst reducing the laser linewidth by the cavity formed. These devices are integrated with laser diode chips to increase the length of the cavity, resulting in coherent, single frequency and narrow-linewidth laser sources.

Amongst the most used laser diode types are extended cavity diode lasers (ECDLs) [34, 42, 43], distributed feedback (DFB) lasers [44, 45], and distributed Bragg reflector (DBR) lasers [46–48]. The configuration of a DFB and DBR laser are extremely similar, with both devices integrating periodic Bragg mirrors to ensure wavelength selectivity. DFB lasers, however, have the grating structure integrated along the entire active region while DBR laser diodes have the structure separated from the active region. In contrast, ECDLs extend the laser cavity with optical components such as lenses and diffraction gratings using an external cavity outwith the laser diode.

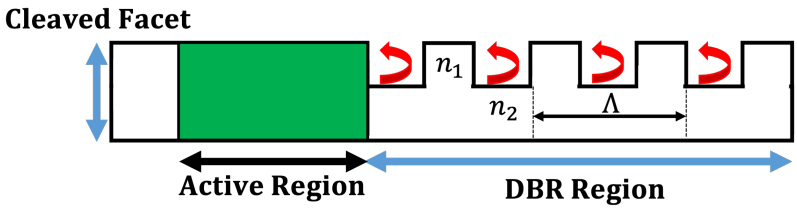

Figure 2.4: Illustration of a DBR laser diode chip, not to scale. The cavity of the laser is extended by integrating a DBR region. The reflection at each index step of the grating is approximately equal to $\frac{n_2-n_1}{n_2+n_1}$.

The Flame module's diode laser configuration is that of a DBR. The company chose to use DBR laser diodes due to the availability of high-power laser diode chips of this configuration that can be seamlessly integrated into a compact package. Figure 2.4 shows the layout for a DBR laser, not to scale. This is an optical resonator consisting of at least one Bragg mirror, an active region where amplification occurs and a cleaved facet where the laser light is output. Typically, the DBR section of the laser is around 100 μm or so [46, 49]. A Bragg reflector is a periodic structure of alternating refractive indices, n_1 and n_2. The grating has a favoured reflection wavelength, λ_{Bragg},

$$\lambda_{Bragg} = 2n_{eff}\Lambda \tag{2.4}$$

where n_{eff} is the average refractive index difference and Λ is the periodicity of the grating. The wavelength selectivity of the DBR region guarantees that a single longitudinal mode is elected, keeping the laser single frequency. Furthermore, varying n_{eff} through temperature tuning permits for the tuning of λ_{Bragg} and so the lasing wavelength.

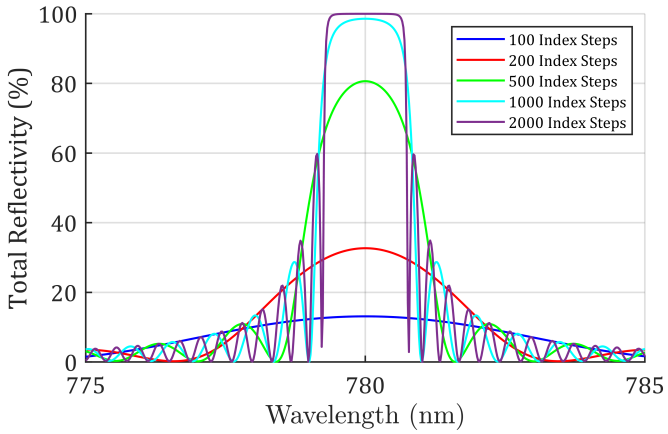

Figure 2.5: Simulated model of a Bragg reflector using software package TFCalc. Plotted is the grating reflectivity against output wavelength for various alterations to the number of index steps. The substrate material chosen in the model was AlGaAs and the refractive index difference was assumed as 0.01. The total length of the DBR section at 1000 steps was found to be 105 microns in this example.

The reflection r from each index step of the grating is approximately equal to $\frac{n_2-n_1}{n_2+n_1}$. The smaller Δn, the smaller the reflection at each step therefore a greater number of index steps are required for maximum reflectivity of the grating. The total reflection of the Bragg mirror r_g is calculated using transmission matrix theory [50] to derive the electric field distribution in a multi-layer stack. Matrix M_n in Equation 2.5 describes the 2×2 characteristic matrix for the n^{th} layer in the Bragg stack,

$$M_n = \begin{bmatrix} cos\beta_n & iq_n{}^{-1}sin\beta_n \\ iq_n sin\beta_n & cos\beta_n \end{bmatrix} \tag{2.5}$$

where β and q are the phase thickness and optical admittance of the material, respectively, and q at normal incidence is equal to the material refractive index. As the number of index steps grows, the computational burden and complexity involved in computing each matrix from every layer escalates significantly. Fortunately, software

packages are available to model and simulate the total reflectance of the Bragg grating. To illustrate this concept, software TFCalc [51] was used. The DBR laser chip used in the Flame is a commercial product. Therefore, due to the proprietary nature of the DBR, comprehensive information regarding parameters such as Δn are not available. Figure 2.5 shows a simulated plot of total grating reflection versus wavelength for a varying number of index steps. For this example, the substrate material chosen was AlGaAs which is the material employed in the active region of the Flame's DBR. The refractive index difference between the two DBR layers was assumed to be 0.01. From the figure, it is clear that once 1000 index steps are applied to the model, the total reflectivity of the grating is maximised and centred at the Bragg wavelength of 780 nm. The total length of the Bragg reflector with 1000 stacks in this case is 105 μm, in good accordance with typical DBR lengths as mentioned. It is then observed on the figure that as the number of stacks are further increased, the DBR reflectivity begins to saturate and additional index steps are no longer necessary.

The output beam from a standard laser diode would ideally be a Gaussian beam. However, the light exits from an asymmetric, rectangular area, as depicted in Figure 2.6. This is an extremely small cross-section, typically tens of μm^2 in area [21], resulting in a substantial beam divergence at the laser output.

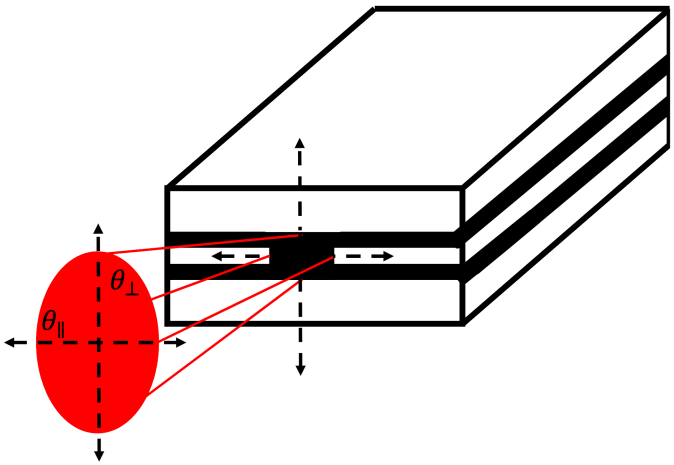

Figure 2.6: Typical output beam of a laser diode with divergence angles in the parallel and perpendicular directions shown. The asymmetry of the active area results in an elliptical output beam.

We define two spatial directions of the output beam, the direction parallel (lateral) to the junction plane and the direction perpendicular (transverse). Typically, the beam divergence of a laser is given on the specification sheet upon purchase as the angular distribution of the intensity in these two directions, usually in (°) at the full-width half-maximum (FWHM) value. Since the vertical direction of the lasing area is much shorter than the horizontal, the beam diverges much faster in the transverse direction than it does in the lateral. Collimation lenses are usually placed after the laser output to attempt to rectify the beam divergence. Typically, fast-axis collimator (FAC) lenses are chosen to collimate in the beam's transverse direction. These lenses are cylindrical, have high numerical apertures and their focal lengths can be appropriately chosen by considering the desired beam diameter and known beam-divergence in the transverse direction,

$$f_{FAC} = \frac{r}{tan(\frac{\theta_{FWHM}}{2})} \tag{2.6}$$

where f_{FAC} is the focal length of the FAC, r is the desired radius of the beam, and θ_{FWHM} is the divergence angle of the laser diode in the fast-direction. Note that the divergence angle is generally given as the FWHM angle on a data sheet, and is usually converted to the half-width $1/e^2$ angle if using $1/e^2$ terminology for the beam radius or diameter. This is roughly 85% of the FWHM angle and the factor of two on the angle denominator can be neglected.

Subsequent to this, a slow-axis collimator (SAC) can be added to collimate in the slow or lateral direction. The focal length is chosen such that the ratio of the transverse divergence angle to the lateral is equal to the focal length ratio of the SAC to the FAC,

$$\frac{\theta_{\perp}}{\theta_{\parallel}} = \frac{f_{SAC}}{f_{FAC}} \tag{2.7}$$

The Flame module consists of a commercial DBR laser diode and crucially, suitable collimation lenses had to be chosen by Alter engineers to create a collimated, Gaussian beam. The selected lenses are discussed further in Section 2.4.

2.2 Atom-Light Interactions

This thesis is based on laser modules which include an integrated atomic vapour cell for laser frequency stabilisation. Specifically, Flame devices based upon rubidium and caesium spectroscopy are included. Lasers are vital in atomic spectroscopy, where coherent, tunable and stable light permits for the manipulation and probing of atomic transitions. The implementation of semiconductor laser diodes paves the way for addressing the field requirements of reduced size, weight and power (SWaP) consumption for portable and field-tested atomic sensors. This is attributed to laser diodes being relatively compact, reliable, inexpensive and easily accessible [52]. Before the mechanisms used to achieve laser frequency stabilisation are described, the atomic structure of the species should be introduced.

2.2.1 Atomic Structure of Rubidium

Caesium and rubidium hold particular significance within the domain of quantum optics. Both species, as all alkali metals, possess a lone valence electron within their outer shells. Additionally, the atomic transitions of interest for the respective species fall within the infrared spectrum, a wavelength range well accommodated by an abundance of laser diode devices. Rubidium occurs naturally in two isotopic forms, ^{85}Rb and ^{87}Rb, with a relative abundance of 72% to 28%, respectively. In the interest of brevity, we will consider the atomic structure of ^{87}Rb only, noting that caesium and ^{85}Rb have similar structures.

We consider only the unpaired valence electron surrounding the nucleus, populating the s-shell in the ground state. Figure 2.7 shows the energy level diagram of ^{87}Rb for its ground level and first excited state, the p-shell.

The total electron angular momentum, **J**, is a contribution of the orbital angular momentum of the outer valence electron (L) and the spin (S), resulting in various values of J as $|L - S| \leq J \leq L + S$. The valence electron has spin S=1/2 and L=0 in the s-shell and therefore J=1/2. Considering now the excited state where L=1 introduces two values of J, 1/2 and 3/2. The p-shell is then split in energy from what is known

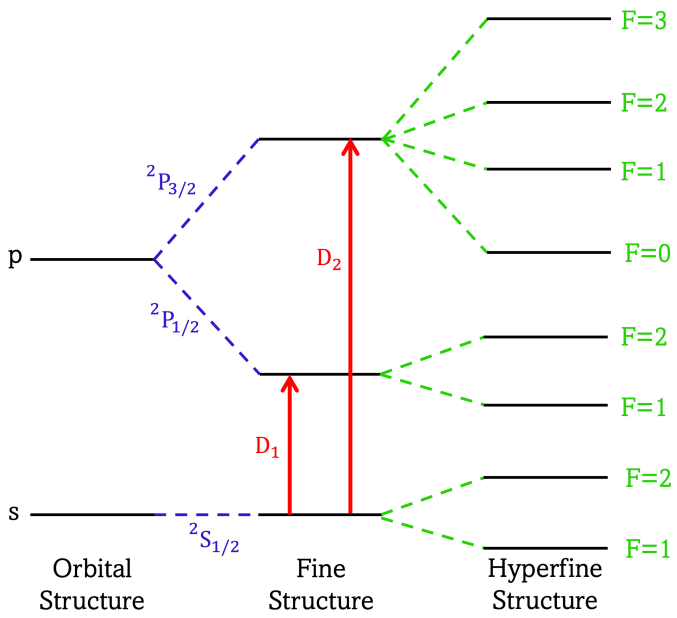

Figure 2.7: Energy diagram for ^{87}Rb, illustrating both the orbital, fine and hyperfine atomic structures. Rubidium's D1 and D2 lines occur at 795 nm and 780 nm, respectively.

as the fine structure of the atom.

Spectroscopic notation is understood as $n^{2S+1}L_J$ with principal quantum number n and L=0,1,2..., corresponding to L=S,P,D, etc. Excitations from the $5^2S_{1/2}$ ground level are therefore denoted as $5^2P_{1/2}$ (lower excited) or $5^2P_{3/2}$ (upper excited) energy states and correspond to what are coined the D1 and D2 transitions, respectively. These resonances occur at 795 nm for the D1 line and 780 nm for the D2 of rubidium [53]. The Flame modules used in this thesis are concerned only with D2.

Beyond the fine-structure splitting exists further splitting of the D1 and D2 transitions. This is the hyperfine structure of the atom arising from the coupling of the total angular momentum of the nuclear spin, **I**, and **J**. The total atomic angular momentum **F** is then $\mathbf{F} = \mathbf{I}+\mathbf{J}$ and $|J - I| \leq F \leq J + I$. The magnitude of **I** for ^{87}Rb is 3/2, derived from the nuclear structure of the isotope. The corresponding values of **F** are shown in Figure 2.7.

This description has focused specifically on ^{87}Rb. The atomic structures for both caesium and ^{85}Rb are extremely similar to the discussed. For ^{85}Rb, the orbital and

fine structures are identical to ^{87}Rb and they have the same resonant wavelength. The hyperfine levels then differ as the magnitude of the nuclear spin, **I**, is 5/2 for for ^{85}Rb [54]. Caesium's resonance transitions occur at 895 nm and 852 nm for the D1 and D2 lines, respectively, with a nuclear spin of 7/2 [55].

2.2.2 Lineshape of Spectral Lines

Interacting resonant or near resonant laser light with an atomic species will see a decrease in the transmitted light as photons are absorbed by the atoms. The specific profile of the transmitted light is governed by several factors which affect the atoms both homogeneously and inhomogeneously. We will first consider the most narrow lineshape possible in laser spectroscopy experiments. This is the condition most desired in spectroscopy setups, specifically when seeking to frequency stabilise a laser. Atomic transitions manifest as exceptional frequency references, with the most narrow lineshapes constituting to the strongest laser locks and frequency stabilities.

The linewidth of the absorbed light is determined by the lifetime of the atomic transition, τ_{nat}. Heisenberg's uncertainty principle describes the broadening of the spectral lineshape,

$$\Delta E \Delta t \geq \hbar \tag{2.8}$$

where $\Delta t = \tau_{nat}$, ΔE is the energy difference of the transition and $\hbar$ is the reduced Planck's constant. Fundamentally, the finite lifetime of the transition results in a higher uncertainty of the energy levels. As,

$$E = \hbar\omega \tag{2.9}$$

$$\Delta\omega = \frac{\Delta E}{\hbar} \tag{2.10}$$

therefore,

$$\Delta\omega \approx \frac{1}{\tau_{nat}} \tag{2.11}$$

where $\Delta\omega$ is the frequency spread of the transition, usually expressed as Γ_{nat}, the

FWHM value of the spectrum. This is coined the natural broadening of an atomic transition, an example of homogeneous broadening. The resultant lineshape of this absorption spectra is a Lorentzian profile,

$$\mathcal{L}(\omega, \omega_0) = \frac{\Gamma_{nat}}{2\pi} \frac{1}{(\omega - \omega_0)^2 + (\Gamma_{nat}/2)^2)} \tag{2.12}$$

The lineshape function as a result of this mechanism is given by Equation 2.12. The parameters ω and ω_0 are the laser frequency and the resonance frequency of the transition, respectively. This gives a lineshape similar to that shown in Figure 2.8.

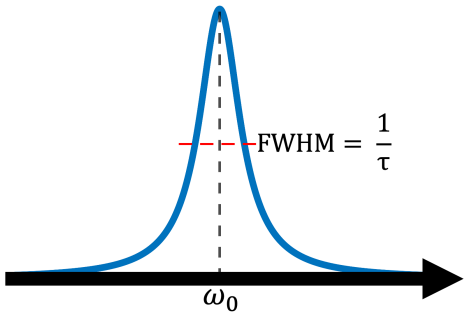

Figure 2.8: An example Lorentzian plot with the full-width half-maximum (FWHM) labelled. At its narrowest this width is about $2\pi\times6.1$ MHz for a transition in the D2 line of ^{87}Rb.

The lifetime of the ^{87}Rb $5^2S_{1/2} \rightarrow 5^2P_{3/2}$ transition is 26.2 ns [56], giving a natural linewidth of about $2\pi\times6.1$ MHz. It is then an obvious requisite that the linewidth of the laser which is to interact with the atoms is less than this value. An overview of the requirements of the laser used in spectroscopy will be discussed in Section 2.3.3.

The natural linewidth constitutes the narrowest visible feature in a laser spectroscopy setup. Additional broadening mechanisms such as pressure broadening within the atomic gas also contributes to the detected lineshape. This occurs when the atoms collide with one another as well as with the cell walls. This is also a homogeneous mechanism, and takes effect on the lineshape when the time between collisions, $\tau_{collision}$, is

shorter than τ_{nat}. Equation 2.13 shows the formula for $\tau_{collision}$,

$$\tau_{collison} \sim \frac{1}{\sigma_s P}\left(\frac{\pi m k_B T}{8}\right)^{\frac{1}{2}} \tag{2.13}$$

where σ_s is the collision cross-section, P is the pressure, m is the atom mass, T is the temperature and k_B is Boltzmann's constant. Working at low cell pressures therefore aids the prolonging of $\tau_{collision}$, keeping the linewidth near that of the Γ_{nat}. This is typically pressures in the mTorr range for cells to be used in atomic spectroscopy, where homogeneous broadening of the atomic transitions scale as 20 MHz per Torr [26].

Experimentally speaking, however, the natural linewidth is not realised using a standard laser spectroscopy setup. This is a consequence of the Doppler effect, governed by the random thermal distribution of the atoms within the atomic vapour. Moving atoms encounter laser light of varying frequency due to the Doppler effect. Figure 2.9 shows analytically the profile for the atoms in a gas as they travel in different directions with respect to the laser light. The net result of this is then a broadened profile, the distribution of which is detailed below.

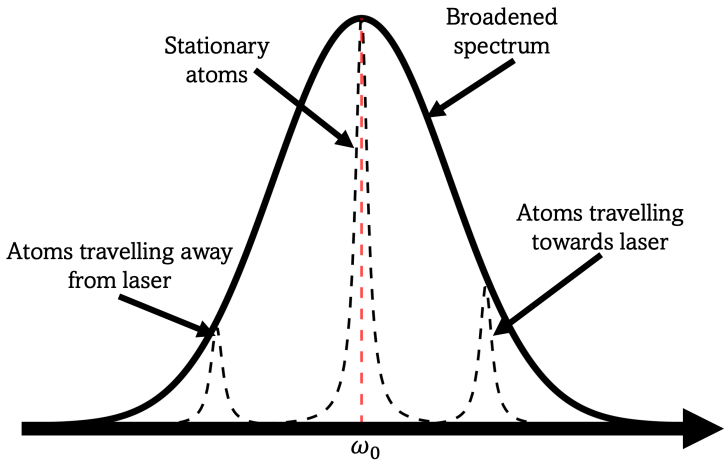

Figure 2.9: An example picture of a Doppler broadened atomic transition. The atoms travelling towards and away from the laser observe the laser frequency differently than in their rest frame due to the Doppler effect.

Equation 2.14 shows the observed frequency of an atom for when it is moving either

towards the laser light or away from it, an increase in frequency shift and a decrease, respectively.

$$\omega' = \omega_0(1 \pm \frac{v}{c}) \tag{2.14}$$

Here, ω_0 is the resonance frequency in the rest frame of the atoms, v is the velocity of an atom and c is the speed of light. The distribution of the velocities is described by the Maxwell-Boltzmann distribution, where $P(v)dv$ is the probability of an atom travelling from v to $v + dv$,

$$P(v)dv = \sqrt{\frac{m}{2\pi k_B T}} exp\left(-\frac{mv^2}{2k_B T}\right) dv \tag{2.15}$$

Substituting in $v = \frac{c(\omega-\omega_0)}{\omega_0}$ from Equation 2.14 into Equation 2.15 gives,

$$P(v)dv = \sqrt{\frac{mc^2}{2\pi k_B T {\omega_0}^2}} exp\left(-\frac{mc^2(\omega-\omega_0)^2}{2k_B T {\omega_0}^2}\right) = \mathcal{G}(\omega, \omega_0) \tag{2.16}$$

This is Gaussian distribution due to the Doppler broadened atoms, with FWHM,

$$\Gamma_{Dopp} = \frac{2\omega_0}{c}\sqrt{\frac{(2ln2)k_B T}{m}} \tag{2.17}$$

Simplifying Equation 2.16 to,

$$\mathcal{G}(\omega, \omega_0) = \frac{2\sqrt{ln2/\pi}}{\Gamma_{Dopp}} exp\left(-\frac{4ln2(\omega-\omega_0)^2}{{\Gamma^2}_{Dopp}}\right) \tag{2.18}$$

For rubidium atoms at room temperature Γ_{Dopp} is around $2\pi\times$510 MHz [57], two orders of magnitude greater than the natural linewidth of the atoms. This type of broadening is an inhomogeneous mechanism, as an individual atom's interaction with the light is contingent on its velocity with respect to the laser.

2.3 Laser Spectroscopy

2.3.1 Saturation Absorption Spectroscopy

Methods based on laser precision measurements are reliant on the laser being stable in frequency for long periods, as well as narrow in linewidth. Laser diodes such as ECDLs and DBRs, can intrinsically reach suitable linewidths as discussed in Section 2.1. Over time however, fluctuations in the laser current or temperature will consequently affect the frequency. This section will introduce laser frequency locking and the methods which can be used to achieve it.

Atomic transitions are perfect candidates for stabilising lasers to as they are extremely stable frequency references. Atomic samples at room temperature produce broadened absorption spectra due to the Doppler effect, with the typical Doppler broadening at ∼500 MHz wide leaving the hyperfine levels of ^{87}Rb's D2 line unresolved. Saturation absorption spectroscopy (SAS) allows for the hyperfine transitions of an atom to be resolved, resulting in Doppler-free measurements and the subsequent stable locking of a laser's frequency.

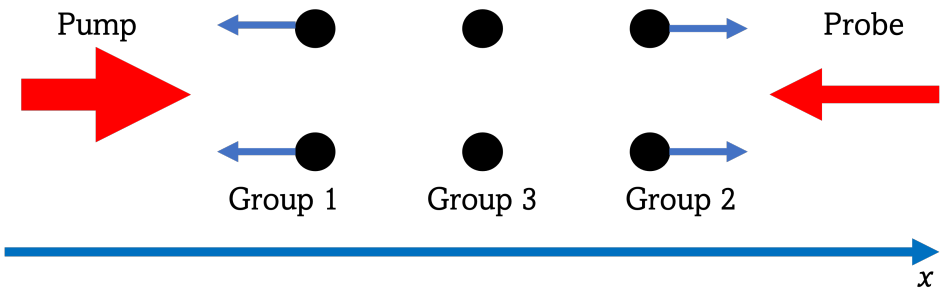

Figure 2.10: The basic setup for saturation absorption spectroscopy (SAS). Counter-propagating laser beams are directed at an atomic sample. The atoms are grouped depending on their direction of travel. Tuning the laser to ω_0 results in both beams addressing the same group of atoms. This leads to the pump depleting the ground-state atomic transitions as the laser is scanned across resonance, increasing the probe transmission through the cell.

The method can be described with reference to Figure 2.10. Two counter-propagating

laser beams are directed at a cell of atoms. Each beam is obtained from the same laser hence possess the same laser frequency. Labelled in Figure 2.10 are three groups of atoms based on their velocity within the cell. The group 1 atoms are considered as travelling in the negative x-direction, group 3 are stationary atoms and group 2 are atoms moving in the positive x-direction. For illustrative reasons only, we consider that the pump beam is more intense than the probe. This is often not the case, such as in the Flame module, where the counter-propagating laser beams are obtained by the pump beam reflecting at a mirror to double-pass the cell and act as the probe.

Saturation absorption spectroscopy can be ascribed to two main effects, saturated absorption of the atomic transitions but most dominantly, optical pumping. Primarily, let us consider that the pump and probe beams are red-detuned from resonance, with $\omega_{red} < \omega_0$. The Doppler effect declares that the atoms in group 1 will absorb the pump beam as the group 2 atoms absorb the probe. Figure 2.11 illustrates this scenario, where $N_1(v)$ and $N_2(v)$ are the population densities of the ground and excited states, respectively, as a function of atom velocity. The pump and probe beams are interacting with separate velocity groups when the laser is detuned from resonance, and each laser populates atoms from the ground to excited state.

As the laser is tuned to ω_0, the pump and probe beams both interact with the group 3, stationary atoms. Considered in Figure 2.11 and the scenario above is a two-level atom, when instead a multi-level picture should be used. Let us consider the D2 level of ^{87}Rb, as described in Section 2.2.1. If the pump beam populates atoms from F=2 to F'=1, the atoms will spontaneously decay to either F=2 or F=1. Atoms which fall to F=1 are no longer involved in the optical pumping process, and the laser interacts with less atoms. Atoms which decay to F=2 will continue to be excited by the intense pump. The probe therefore has less atoms to interact with, resulting in an increase in the probe light transmission as the pump depletes the population in F=2. As the laser frequency is scanned across resonance, a Doppler broadened Gaussian profile is observed with additional narrow peaks at the corresponding hyperfine transitions. These peaks are Lorentzian and in optimal conditions can reach that of the natural linewidth.

As well as resolving the hyperfine levels of a Doppler broadened transition, addi-

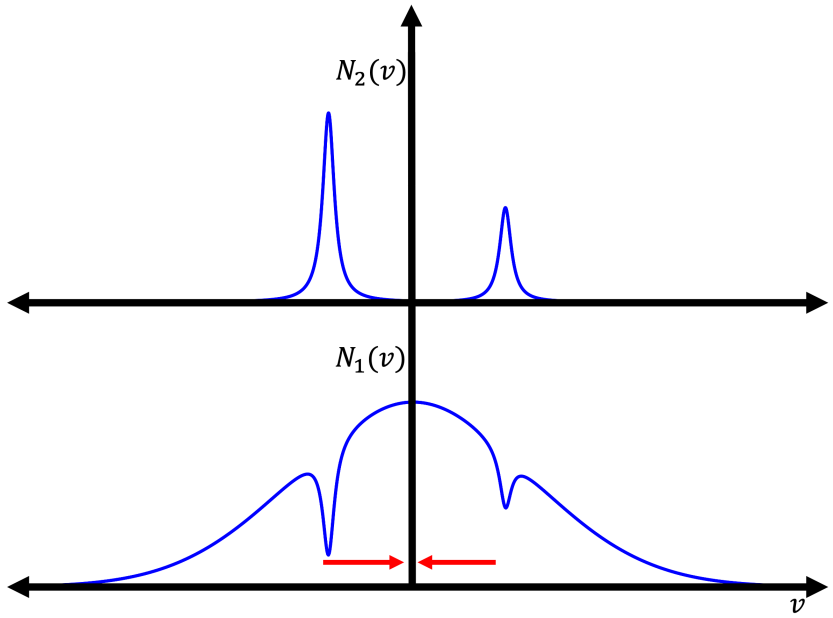

Figure 2.11: The population distribution of a two-level atom as a function of the atom velocity due to the pumping and probing laser beams. We consider the resonant velocity here to be the laser detuning from resonance over k.

tional peaks named crossover transitions are apparent. These transitions are a result of the F' levels sharing a common F ground state. Therefore, when the laser frequency is halfway between two F' levels, the group 1 and 2 atoms are excited simultaneously. The moving atoms experience being on resonance with both F' levels due to the counter-propagating beams. The symmetry of this process produces crossover peaks between two hyperfine levels. These crossover transitions are particularly convenient when it is necessary to stabilise the laser slightly off resonance from an atomic transition. This is relevant and will be discussed in detail in Chapter 4.

Figure 2.12 shows an example signal of the probe laser's transmission during SAS of ^{87}Rb, with the transitions labelled. In the following section, we will discuss how the Doppler-free spectroscopy of an atomic species can be used to provide a stable frequency reference for laser locking.

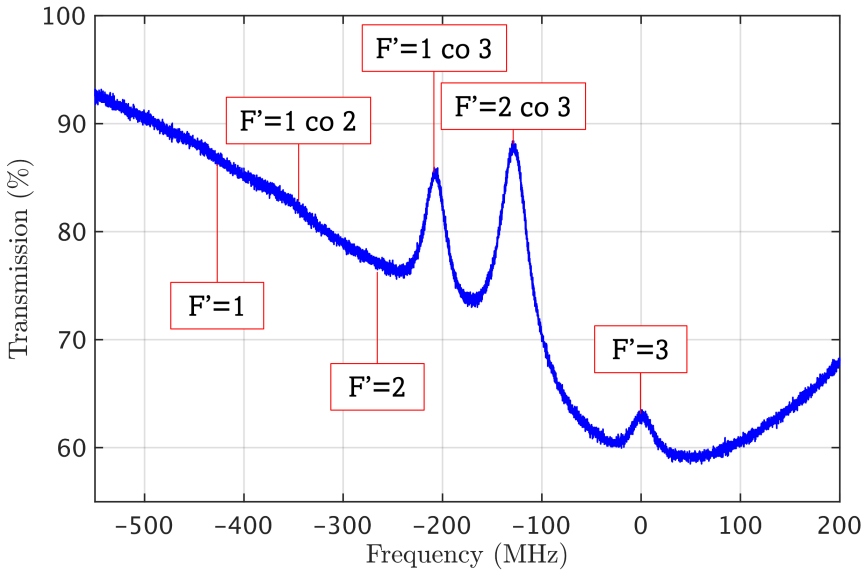

Figure 2.12: An example saturation absorption signal of ^{87}Rb for the excitation of F=2 to the F' levels. The crossover transitions are denoted as co.

2.3.2 Laser Frequency Stabilisation

Doppler-free spectroscopy permits the hyperfine transitions of an atom to be resolved. The resultant signal produces a narrow spectral feature with a known and stable frequency, which a laser can be stabilised to. A lock-in amplifier (LIA) is implemented to output a control signal, or an error signal, to stabilise the laser frequency to the peak of an atomic transition. Any drift in the laser frequency will be realised and counteracted by a proportional-integral-derivative (PID) feedback loop in the LIA, re-tuning the laser's frequency to be on resonance by the appropriate amount.

Figure 2.13 shows a simulated example signal of a Lorentzian peak and its first derivative, the error signal, which is the output of the LIA. This is a specifically desirable signal as it is asymmetric and the control loop can determine both the distance in frequency to reach resonance and the direction the feedback should be applied. When the laser is on resonance with the atomic transition, the error signal will equal zero. This stabilisation technique is achieved in this project by introducing a modulation to the laser frequency.

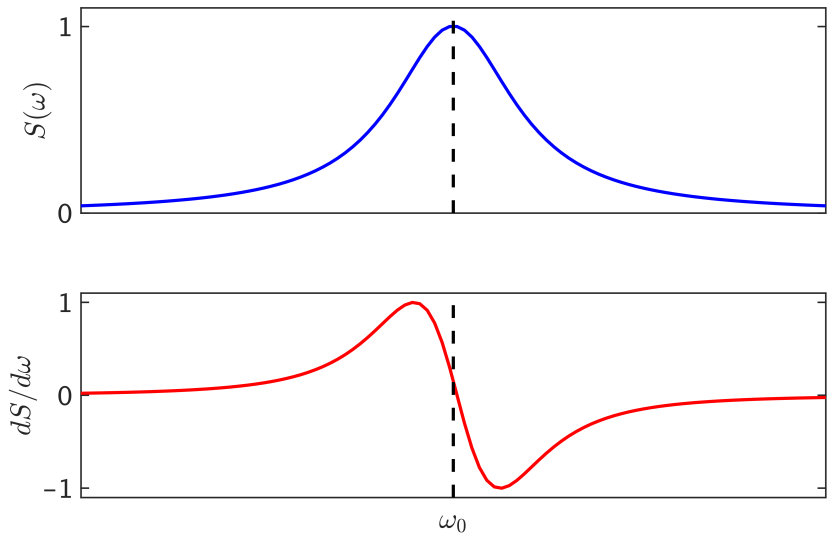

Figure 2.13: A simulated Lorentzian signal and its first derivative which is known as the error signal. This is the signal used to lock a laser to the peak of an atomic transition, advantageous as the asymmetry conveys the direction in which the laser has drifted.

Referring to Figure 2.14, a Lorentzian-like absorption peak is observed as the laser frequency ω_{Laser} is scanned and detected by a photodiode. Consider a modulation signal which takes the form,

$$S_{ref} = sin(\omega_{mod}t + \phi_{ref}) \tag{2.19}$$

where ω_{mod} is the modulation frequency, t is time and ϕ_{ref} is the signal phase.

Applying this modulation signal to the laser frequency causes periodic changes in laser frequency, $\Delta\omega$. This then induces corresponding oscillations in the light detected, ΔA. The magnitude of ΔA is then contingent on the laser frequency, and how close it is to ω_0. The amplitude of the signal can therefore be considered as,

$$\Delta A = \frac{dS}{d\omega}\Delta\omega \tag{2.20}$$

where $\frac{dS}{d\omega}$ is the derivative of the absorption signal, and $\Delta\omega$ is the modulation depth.

The detected signal S_{det} when the laser is off resonance will have amplitude ΔA

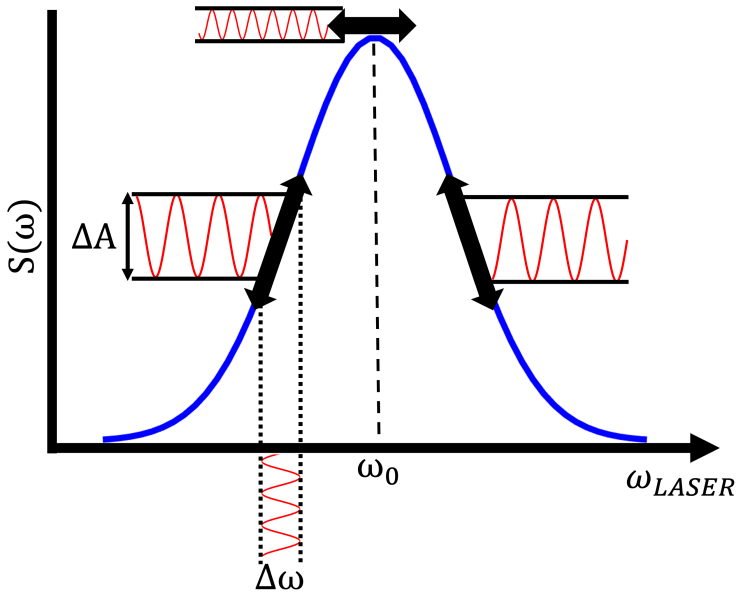

Figure 2.14: An illustrative example of a frequency modulated laser interacting with an atomic transition. The modulation depth $\Delta\omega$ directly changes the detected signal's amplitude by ΔA.

and a frequency ω_{mod} which matches that of the reference signal,

$$S_{det} = \Delta A sin(\omega_{mod} t + \phi_{sig}) \tag{2.21}$$

This is the input of the lock-in amplifier. The first stage of the LIA is to demodulate the detected signal, simply by multiplying the signal by the reference. This is executed by a mixer, and the modulated signal is multiplied by reference signal S_{ref},

$$S_{mix} = \frac{\Delta A}{2} \left(cos(\phi_{sig} - \phi_{ref}) - cos(2\omega_{mod} t + \phi_{sig} + \phi_{ref})\right) \tag{2.22}$$

The resultant mixer signal consists of a direct current (DC) term which is contingent on the phase difference between the detected signal and the reference signal, and an alternating current (AC) signal which varies at twice the modulation frequency. The second term can be eliminated by use of a low-pass filter (LPF) with a cut-off frequency lower than that of the modulation. This equation can be further simplified with some control of phase, optimised when $\phi_{sig} - \phi_{ref} = 0$ and the first term equal to 1. This

simplifies the equation to $S_{mix} = \frac{\Delta A}{2}$ or $S_{mix} = \frac{dS}{d\omega}\frac{\Delta\omega}{2}$, a DC term proportional to the derivative of the absorption signal. This is the output of the LIA, the error signal used to the stabilise the laser. Both the phase control and LPF are included components in the LIA, as shown in Figure 2.15 which overviews the integration of SAS and the use of LIAs for frequency stabilisation. When the laser is off resonance, the detected signal's frequency component does not match that of the reference signal as the applied modulation periodically shifts the laser on and off resonance. This results in a detected signal with a frequency twice that of ω_{mod} which is filtered out by the LPF after the mixing stage, giving a signal equal to zero.

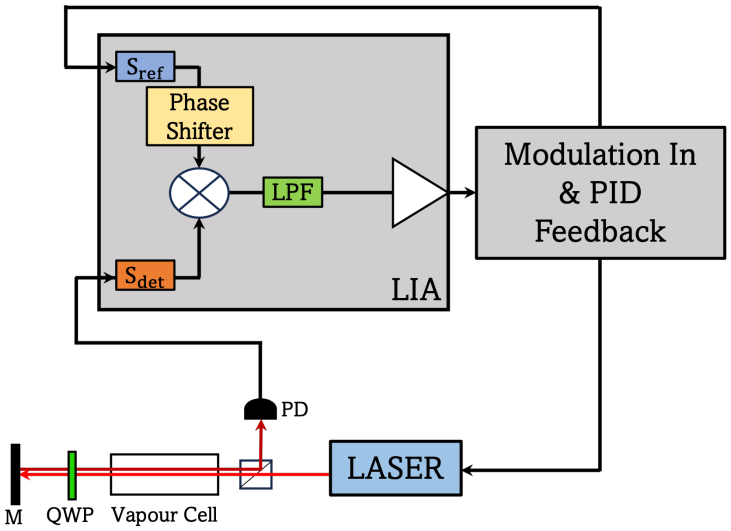

Figure 2.15: The experimental setup for frequency locking a laser. A laser is frequency modulated and employed in a saturation absorption spectroscopy setup. The detected light at the photodiode enters the LIA, S_{det}. S_{det} is demodulated by mixing the signal with S_{ref}. An LPF is then applied to attenuate terms above the modulation frequency. The result is a DC signal which is amplified and sent to a feedback loop. The feedback directly applies the necessary adjustment needed for the laser to maintain resonance by feeding it back upon the laser current.

Figure 2.15 illustrates the setup for laser locking which is used in this thesis. The laser is frequency modulated, by applying a signal S_{ref} to the laser diode's current. The output light is directed towards a double-pass spectroscopy configuration, realising SAS as described in Section 2.3.1. The light is detected at a photodiode and sent to the input of the LIA, S_{det}. The reference signal enters a phase shifter and is mixed with S_{det}. The

resultant signal is then simplified with a LPF as discussed and amplified, before being sent to a feedback loop. The output of the LIA determines if the laser is on resonance and the provided feedback is directly applied to the laser to maintain resonance. The experiments detailed in this thesis use commercial diode-laser controllers (DLCs) with integrated LIAs and feedback control to drive and lock the Flame laser.

The method described above and used in this project is known as dither locking, used in conjunction with SAS. There are of course various other laser locking methods relying on atomic frequency references which should be briefly discussed. dichroic atomic vapour laser locking (DAVLL) [58] comes with the benefit of a large capture range, meaning that the laser can experience frequency disturbances in the range of 100s of MHz [59] whilst remaining locked to the specified point. This is due to the method relying on single-beam absorption through the vapour cell. The accuracy of the lock is, however, inadequate compared to Doppler-free methods, such as dither locking via SAS, polarisation spectroscopy [60] and modulation transfer spectroscopy [61]. Each of these techniques rely on pumping and probing beams, with the latter two not requiring direct modulation of the laser which can be advantageous. Modulation transfer spectroscopy relies on modulation of the pump via electro-optic modulator (EOM) or acousto-optic modulator (AOM) which can be expensive and bulky components. Alternatively, polarisation spectroscopy often requires magnetic field cancellation [62] as the scheme relies on applying a controlled magnetic field to distribute atoms to different Zeeman levels. It is therefore sensitive to external magnetic fields in the experimental environment. Dither locking is arguably the most simplistic method of the three to implement, requiring the least amount of components or considerations meaning that the setups can be kept compact. Ultimately, quantitative measurements such as recording the stability of the laser using the selected locking method and measuring the laser linewidth are crucial in determining if the technique is adequate for the required application.

2.3.3 Laser Cooling Requirements

To give an overview of the discussed content thus far, fundamental atomic physics experiments rely on narrow-linewidth and stable laser sources. Semiconductor laser diodes serve as fundamental devices due to their attractive features, namely being inexpensive and readily accessible. To achieve the accuracy required in terms of frequency stability, the Flame uses frequency modulation in conjunction with saturation absorption spectroscopy to lock a laser to an appropriate atomic transition.

Laser cooled atoms serve as the starting point for many quantum technology applications, particularly in atomic clocks and atom interferometry. These experiments rely on atoms which have been slowed, ensuring longer probing times for highly precise measurements. To conclude this section, an outline of the typical laser requirements for the applications relating to cooled atoms will be reviewed.

The three most stringent laser parameters are the laser linewidth, the output power, and the frequency stability. As discussed, a requisite for the laser linewidth is that it is much narrower than the natural linewidth of the atoms being probed. This is around $2\pi \times 6$ MHz for rubidium and typically a laser linewidth less than 1 MHz is essential [23,24]. Additionally, the stability of the laser frequency over time should stay within a few MHz [25]. The required laser output power in cold atom applications is not as tightly defined and varies between experiments. Typically 10s of mWs [15, 63–65] is required for cold-atom clocks, increasing to 100s of mW for atom interferometers [9, 66–68], particularly for those which utilise Raman pulses [10] for manipulation of the atomic state. With these considerations in mind, let us now introduce the Flame laser.

2.4 The Flame Laser

This thesis is based upon various Flame models fabricated by Alter UK, mostly operating at 780 nm or 852 nm. In this chapter, we have focused on semiconductor laser diodes, and their vital role within atomic precision measurements and quantum technology applications. This section will describe how the Flame module is fabricated,

its operation, as well as redesigns and realisations made throughout the course of this project. We will conclude this section with a brief discussion on similar laser packages to the Flame.

Section 2.3.3 provided an overview of the conventional laser requirements for laser cooling experiments. However, it did not delve into the contemporary push towards achieving portability and compact setups in recent times. Considerable effort has been dedicated to developing compact cold-atom platforms and sensors, where it is additionally imperative to address the size of the laser system and the choice of lasers used. The unique attribute of the Flame is its ability to be frequency stabilised to within its 6 x 4 x 1.5 cm package. This surpasses standard laboratory setups for frequency locking in terms of volume, where a plethora of space and large optical components are used to laser lock. This makes the product a competitive laser source in the market as it confronts the field goal of miniaturisation. A comparison of the Flame with other compact and integrated laser systems will be discussed in Section 2.4.10.

2.4.1 Flame Characteristics

The semiconductor material employed in the active region of the laser diode is AlGaAs for Flame devices operating at 780.241 nm. Figure 2.16 show the laser current and temperature tuning rates with wavelength. In Figure 2.16a, the current was tuned from 100 mA to around 250 mA, the maximum operating current of the laser. The temperature was kept at a constant value each time and the wavelength of the output light was recorded. This was repeated for four temperature values. A linear fit was added to each iteration, giving an average current tuning rate of 0.0014 nm/mA. For Figure 2.16b, the operating current was kept at a constant value of 200 mA as the temperature of the thermoelectric cooler (TEC) was tuned from 5°C to 30°C to record the resultant wavelength. The fitted line gives a gradient of 0.059 nm/°C. The tuning range of the module (∼0.6 nm) is more than sufficient for atomic spectroscopy applications, where the target wavelength of 780.241 nm is all that is required for interacting with ^{87}Rb and ^{85}Rb's D2 line atomic transitions. This target wavelength is reproduced consistently with the laser, and the particular module tested did not experience mode

hops.

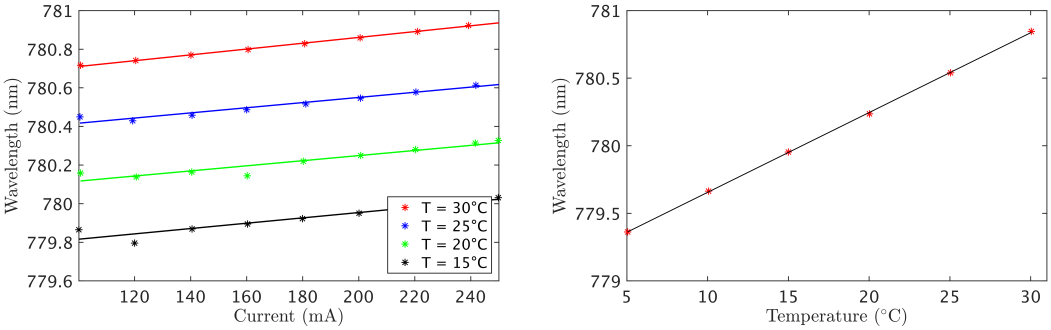

(a) (b)

Figure 2.16: (a) Current tuning against laser wavelength for a Flame device at various temperatures. A linear fit was added to each example, giving an average gradient of 0.0014 nm/mA. (b) An example of the temperature tuning rate of a Flame at a constant current of 200 mA. This results in 0.059 nm/°C based on a linear fit.

Figure 2.17 shows an example P-I curve for a Flame module. The threshold current for the DBR laser is around 60 mA, with a slope efficiency of 0.72 mW/mA. Discussed in Section 2.1, the slope efficiency of a laser represents the number of electrons to photons produced, where the optimal outcome would be one photon for every electron. A slope efficiency of 0.72 mW/mA therefore demonstrates a highly efficient laser source.

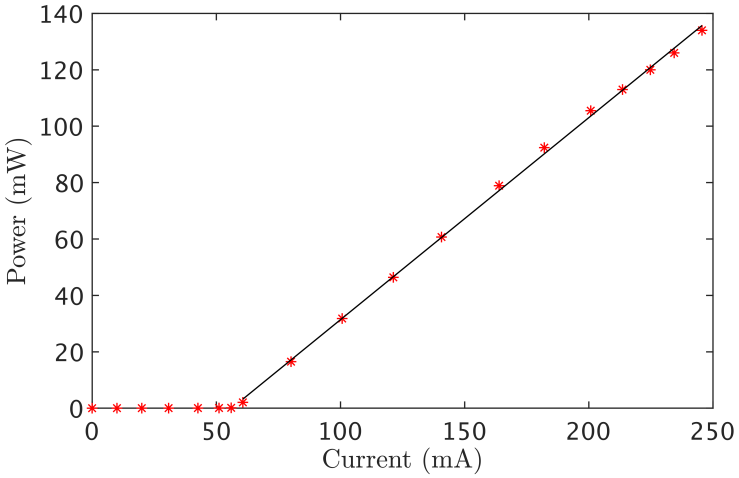

Figure 2.17: P-I curve of a Flame yields a threshold current around 60 mA with slope efficiency of 0.72 mW/mA derived from a linear fit.

The DBR's FWHM beam divergence, as given by the manufacturer, is (6 x 26)° for the lateral and transverse direction, respectively. This is conventionally converted to half-width (HW) $1/e^2$ values, (5.1 x 22.1)°. Alter engineers then chose appropriate FAC and SAC lenses using Equations 2.6 and 2.7, with 0.5 mm selected as the Flame's $1/e^2$ beam diameter. The FAC focal length calculated for the chosen beam diameter is therefore 0.6 mm, and a commercial off the shelf (COTS) FAC with this focal length was procured. For the SAC, the calculated focal length of 4.3 mm was not obtainable and the closest focal length available was selected.

Figures 2.18a and 2.18b present an example beam image of a Flame device at the module output, along with the typical beam divergence. The output of the module is considered as the distance at 0 mm, the actual distance from the laser facet is around 50 mm or so. The $1/e^2$ beam-diameter in the x-dimension and y-dimension for Figure 2.18a is 0.52 mm and 0.55 mm, respectively. These values closely resemble the desired beam diameter of 0.5 mm. The beam-diameter as a function of distance from the module output was recorded to determine the divergence of the beam. A straight line was fitted to each the x and y diameters, returning gradients of 0.0035 and 0.0036, respectively. These gradients are the beam divergence full-angles measured in radians. The half-angle divergences, as is conventionally preferred, are therefore 1.75 mrad and 1.8 mrad for the x and y dimensions.

Figure 2.18b displays that the x and y dimensions of the laser beam diverge at similar rates, exhibiting a circular beam. It is useful to additionally determine the beam quality factor [69] of a laser, the M^2 value. The M^2 value determines how perfectly Gaussian a beam is, with a value of 1 revealing a transverse-electromagnetic mode (TEM) of TEM_{00} and any value above indicating the presence of additional contributing modes.

Determining the Flame's M^2 value involved focusing the laser beam output to ascertain the beam waist, w_0, defined as the minimal beam radius. The $1/e^2$ beam

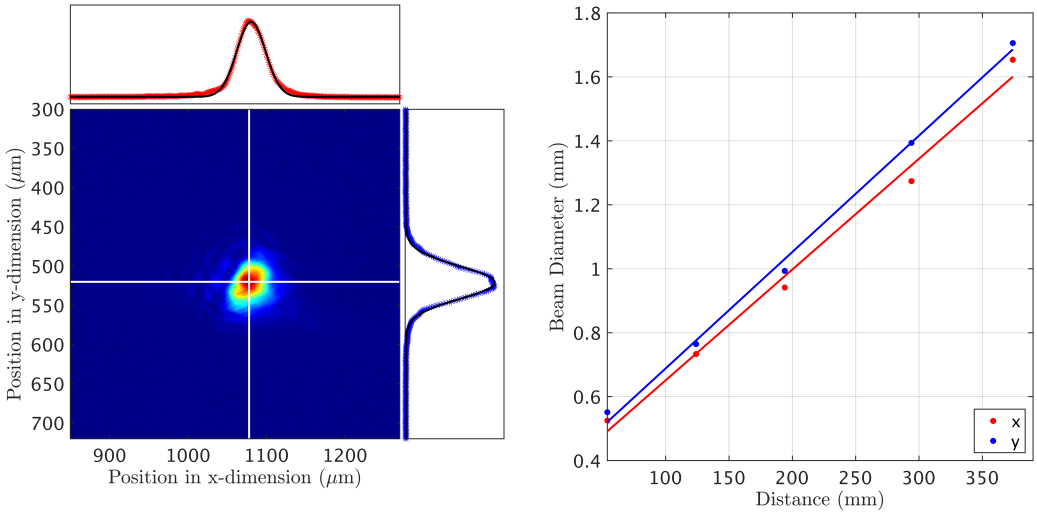

(a) (b)

Figure 2.18: (a) Image of a Flame laser beam with the Gaussian distributions plotted along the x and y dimensions. The $1/e^2$ beam-diameter for each dimension is 0.52 mm and 0.55 mm for x and y, respectively. (b) The $1/e^2$ beam-diameter in each dimension versus the distance from the laser output. The calculated divergence is 1.75 mrad and 1.8 mrad for x and y, respectively.

radius propagating along a direction z is described as,

$$w(z)^2 = {w_0}^2 \left(1 + (z - z_0)^2 \left(\frac{M^2\lambda}{\pi {w_0}^2}\right)^2\right) \tag{2.23}$$

where z_0 is the location in z where w_0 occurs. A lens of focal length 100 mm was placed in front of a Flame module. A beam profiler was positioned after the lens on a translation stage to image the beam along z. The recorded beam radii with distance (from the lens) z are plotted and displayed in Figure 2.19 for both the x and y dimensions of the laser beam. After determining w_0 and therefore z_0 from the experimental data, Equation 2.23 was used to apply a fit to the data and determine the M^2 value. Figure 2.19 uses a fixed fit value of 1 for M^2 in both the x and y dimensions. Errors in the recorded beam radii are included but are smaller than the marker size. These errors are determined by the standard deviation of the beam radii (in each dimension) after 50 frames for each distance. Figure 2.19 indicates that the

Flame laser tested has a TEM_{00} mode in both the x and y beam dimensions.

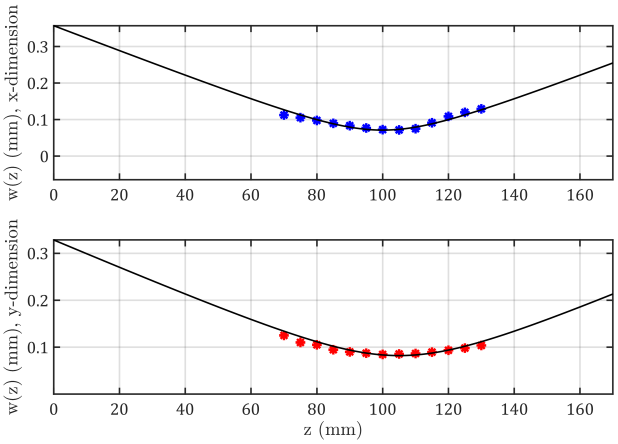

Figure 2.19: The measured laser beam radius with distance z, succeeding a f=100 mm lens, for the x dimension (top) and y dimension (bottom). A fit was applied to the data using Equation 2.23, where M^2 was fixed to equal 1.

2.4.2 Module Layout

The Flame consists of COTS components, packaged and aligned by Alter engineers. Figures 2.20a presents an image of a Flame laser, with Figure 2.20b showing an annotated version. A DBR laser diode and accompanying fast and slow axis collimators are aligned on a TEC bench. The TEC controls the laser diode temperature and therefore the tuning of the laser frequency, as discussed previously in this chapter. The first optical component following on from the FAC and SAC lenses is a polarising beamsplitter (PBS), where the majority of the laser light is transmitted to the output window of the module. This is typically more than 150 mW in output power and varies between laser diode chips. The reflected light at the PBS is directed to a second PBS where the light reflected here leads to the spectroscopy arm of the module.

The spectroscopy arm is a saturation absorption spectroscopy configuration. The light enters a QWP, then a 12 mm glass-blown atomic vapour cell before hitting a dielectric mirror and reflecting back towards PBS 2. The majority of the light is transmitted at the PBS and directed towards the integrated photodiode of the module. The double passing of the light at the vapour cell allows for the narrow hyperfine levels

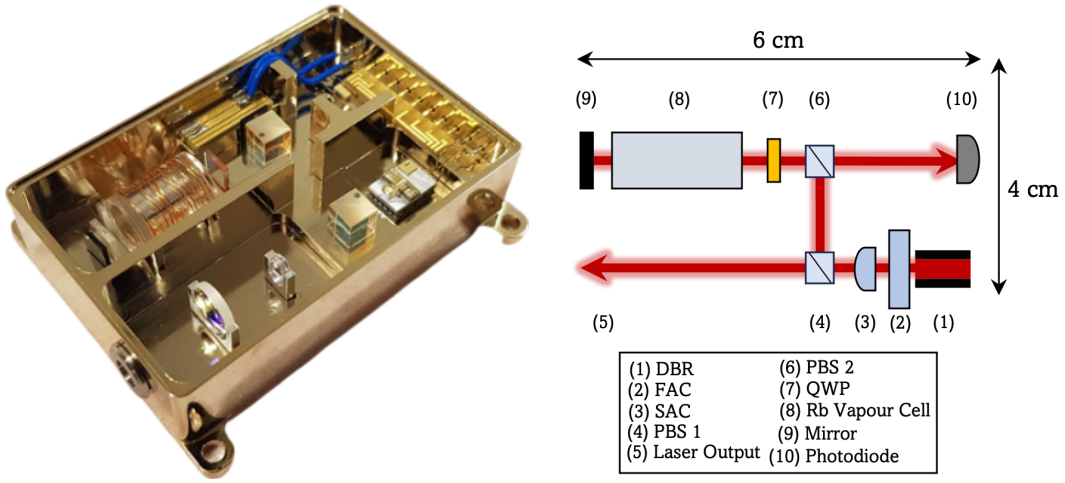

(a) (b)

Figure 2.20: (a) A photograph of a Flame module with the lid removed to show the various optics which allow for SAS and frequency stabilisation of the laser. This is a model photograph of the module, and the modules used in this thesis do not contain the additional telescope included in this image. (b) A labelled version of (a) with the beam path depicted. Starting at (1), a DBR laser is collimated with FAC and SAC. The majority of the light (typically more than 150 mW) is transmitted at the first PBS. The reflected light, reflects at a second PBS leading to the spectroscopy arm of the module. The beam doubles passes a quarter wave-plate (QWP) and a vapour cell to transmit at the second PBS for detection at a photodiode. (PBS: polarising beam-splitter, QWP: quarter wave-plate)

of the atomic species to be resolved through SAS.

The integrated spectroscopy scheme of the laser permits the frequency to be stabilised, eliminating the need for external optical components. The result is a compact module, frequency stabilised in-house and outputting over 150 mW of power. The Flame is therefore an appealing product in the field of laser spectroscopy, encompassing a selection of the key traits, discussed in Section 2.3.3.

2.4.3 Pin Configuration

The Flame's outer body consists of 12-pins to electrically drive the module. Table 2.1 overviews the function at each pin. The distance between the pins (2.54 mm) are such that commercially available 24-pin zero insertion force (ZIF) sockets can be inserted into the pins and locked into place with easy removal.

Pin	Function
1	TEC-
2	TEC+
3	Laser Anode
4	Laser Cathode
5	Thermistor
6	Thermistor
7	Photodiode Cathode
8	Photodiode Anode
9	Unused
10	Cell Heater
11	Cell Heater
12	Unused

Table 2.1: Pin Configuration for a standard Flame module.

The table shows that ten of the twelve pins are used. The first 6 pins are what drive the DBR laser, specifically through current and temperature control. Separately, the cathode and anode of the integrated photodiode are connected to pins 7 and 8 for outputting the spectroscopy signal electronically. This signal would then be amplified externally, and sent to the input of a lock-in amplifier for demodulation and deducing the derivative signal to lock the laser frequency to. It is useful to both drive and lock the laser from the same device. Commercially available laser drivers such as MOGLabs DLCs and Vescent drivers account for this, where laser diodes can be both driven and locked using these drivers. For all of the work presented in this thesis MOGLabs DLCs are used for driving and stabilising the modules.

The cell heater is the final component considered, heated by applying a DC current to pins 10 and 11. The heater is a copper wire wrapped around the vapour cell for early Flame models, and is discussed further below (Section 2.4.5).

2.4.4 Detection

After the spectroscopy signal is detected at the photodiode, amplification of the signal is necessary before it is sent to a lock-in amplifier. A 150 kOhm trans-impedance amplifier

(TIA) with a bandwidth of 530 kHz was designed by a colleague. This bandwidth was carefully chosen to ensure that the modulation frequency, which is 250 kHz standard from the MOGLabs DLC, was within the 1 dB passband of the amplifier. The TIA is powered by 12V, interfaced with the DLC via a FireWire cable.

2.4.5 Heating the Cell

The vapour cell used in the integrated spectroscopy of the Flame is 12 mm in length. This is a short cell, meaning at room temperature there are not enough atoms to provide a spectroscopy signal with a high signal to noise ratio (SNR). The cell must therefore be heated to increase the atomic vapour density. To heat the cell in preliminary modules, this was achieved by wrapping a copper wire around the cell and applying a DC-current to the wire. For later models and designs, printed circuit board (PCB) heaters were implemented. This provides more uniform heating, as well as ease of application as the wire-wrap proved finicky to implement during the fabrication process of a module. More significantly though, the wire wrap method is essentially a solenoid and the production of magnetic fields will have an influence on the atomic spectroscopy. This was not an observed issue between models, but nonetheless converting to PCB heaters was considered a design upgrade.

2.4.6 Flame PCB Board

A PCB was fabricated for increased user functionality and protection of the module pins. A 24-pin ZIF plug was used to grip the 12-pins of the module. The ZIF plug was subsequently soldered to the designed PCB. The PCB was specifically configured with integrated slits, strategically positioned to accommodate the passage of wires. These slits serve the dual purpose of facilitating wire insertion and providing strain relief for enhanced durability. Figure 2.21 shows design prototypes of the PCBs, designed on KiCad. The two slits for mitigating the pressure applied to the Flame pins can be seen at the bottom of the PCB.

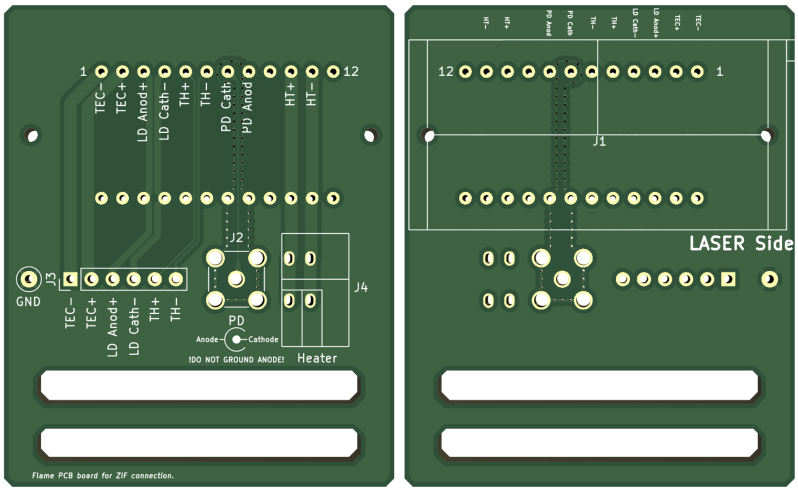

Figure 2.21: The fabricated printed circuit board for attachment to the module pins is shown here. The two slits on the bottom half of the boards are for feeding through the wires to alleviate stress on the pins.

2.4.7 Beam Expanding Optics

The beam intensity at the spectroscopy arm of the module is many orders of magnitude higher than the saturation intensity of rubidium ($I_{\text{sat}} = 1.6$ mW/cm^2). Such intensity completely saturates the atoms within the vapour cell, necessitating a reduction in the beam intensity.

To address this challenge, initial modules utilised neutral density (ND) filters positioned before the second PBS with an optical density (OD) of 0.3. This OD value effectively halves the transmitted power for each added filter. Typically, 3 to 4 filters were employed, reducing the intensity (I) by a factor ranging between 8 and 16. While the resultant intensity still surpasses I_{sat}, it proves suitable for performing adequate saturation absorption spectroscopy, where the condition $I \gg I_{\text{sat}}$ is typically maintained.

In later modules, beam expanding optics were utilised as an alternative solution to decreasing I. The main challenge encountered with the ND filters pertained to the deflection of the beam, necessitating their placement at an angle to mitigate reflections. Additionally, employing a larger laser beam includes interaction with a greater number of atoms within the cell as it extends to a larger area. A telescope of magnification 2 has

been included in recent modules, positioned between the two polarising beam splitters. This successfully reduces I by a factor of 4 and is a considerably better solution than the filters employed previously.

2.4.8 Optical Isolation

It has been realised that the module is extremely sensitive to optical back-reflections. Optical isolators providing around 60 dB isolation have been essential components for the various Flame modules used in this thesis. Figure 2.22 shows spectra examples using the internal vapour cell of the Flame, for 30 dB isolation (red) and 60 dB (blue). It should be noted that the distinct steps seen in the figure approximately every 350 MHz constitute to the free-spectral range of the cavity setup for the demonstration, i.e. the element which is providing the feedback. This is approximately 43 cm in distance from the laser diode.

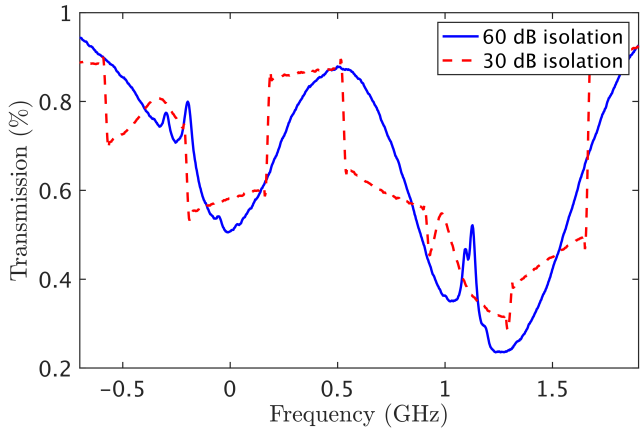

Figure 2.22: An example Flame module spectroscopy signal with 60 dB of optical isolation (blue), compared with only 30 dB of isolation (red). Based on this figure it is evident that a Flame module requires more than 30 dB of optical isolation for optimal operation.

The experiments detailed in this thesis all include external optical isolators delivering 60 dB of isolation to the laser. This is an obvious inconvenience when the goal is to keep the experiments small, and preferably the isolators would be located inside the Flame package. However, isolators on that scale are scarce with high optical loss.

Additionally, as isolators are highly magnetic, it should be proceeded with caution if one was to be placed in such close proximity to the spectroscopy arm of the module.

2.4.9 Example Signal

Figure 2.23 shows example signals for a 780 nm Flame module with an integrated rubidium reference cell. The top image shows the SAS signal for ^{87}Rb (left) and ^{85}Rb (right), with their resulting error signals in the bottom plot. A MOGLabs DLC was used which provides 250 kHz of frequency modulation to the laser, applied directly to the module current. The integrated LIA of the DLC produces the error signal which can be used for locking the laser.

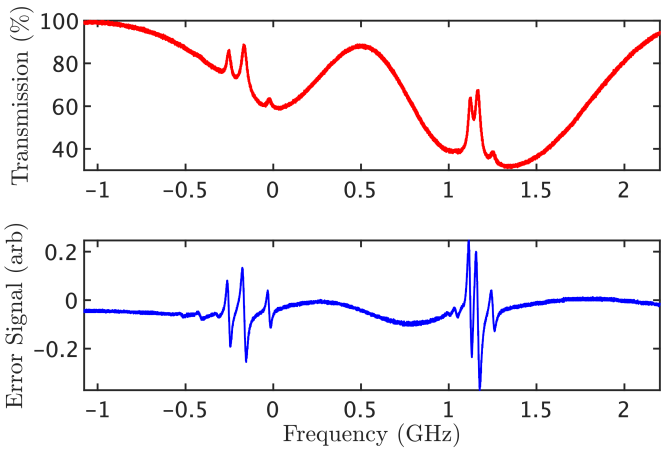

Figure 2.23: Example plots of a Flame's SAS signal and the resultant error signal for the ^{87}Rb F=2 to F' (left) and ^{85}Rb F=3 to F' (right) transitions.

2.4.10 Future Considerations and Similar Devices

The Flame modules used in this thesis output in free-space. In each of the experiments to be detailed the lasers were externally fibre coupled to be integrated into the relevant demonstrations. A future consideration is for the modules to be fabricated as fibre-coupled devices. This will increase user functionality and aligns with the objective of maintaining compact experimental setups. Possible obstacles in employing this approach, however, relate to the optical isolation required when fibre coupling.

Integrating the isolators to within the package, as discussed in Section 2.4.8, could consequently implicate the spectroscopy. An approach to tackling this could be magnetically shielding the vapour cell in future modules. This solution is used in [70], which details a compact laser spectroscopy module similar to the Flame.

Table 2.2 outlines similar compact laser packages which include integrated atomic vapour cells for laser frequency stabilisation. Each example accomplishes this through Doppler-free spectroscopy, employing frequency modulation achieved by modulating the current of the laser diode. The laser modules detailed in [70–73] additionally include the laser driving and locking electronics. This is a long term objective for Alter and the Flame module which is currently driven and locked using commercial DLCs, and would simplify user experience majorly. The Flame surpasses each in laser output power, making it more versatile for the applications discussed in Section 2.3.3.

Company or Research Group	**Laser Package Volume**	**Power Output**	**Additional Info.**
Alter UK	36 cm^3	>150 mW	DBR laser and COTS components
Humboldt Universität zu Berlin [74]	35 cm^3	6 mW	DFB laser and COTS components. Total volume of 400 cm^3 [71], which includes all driving and locking electronics
University of Neuchâtel [70, 72]	200 cm^3	3 mW	ECDL. Total volume of 500 cm^3 including driving and locking electronics
University of Neuchâtel [73]	220 cm^3	70 mW	DFB laser. Total volume of 630 cm^3 including driving and locking electronics

Table 2.2: Similar devices to the Flame in the literature, highlighting some of the key characteristics.

In [73], they additionally present a version of their laser head which includes an AOM (total laser-head volume 2400 cm^3). The AOM allows for laser frequency shifting from an atomic resonance, a necessary step in many cold atom and clock experiments. This implementation doubles their laser-head volume, however, and would not be viable in a Flame package which is fairly compact. Presented in [16] by Dyer et al., frequency control of their laser is achieved by sandwiching an atomic vapour cell between magnetic coils. This introduces a frequency shift via the Zeeman effect, and when integrated with SAS allows for controllable frequency tuning from a locked atomic transition. This could be much more easily executed in future Flame modules requiring limited changes to the current design.

Noteworthy commercial products include Vescent's D2-210 Saturated Absorption Spectroscopy Module [75]. This device is an already-aligned spectroscopy module which requires laser input from the user via free-space or fibre, 500 cm^3 in volume. Company TEM Messtechnik's 'CoSy' unit [76] works similarly to Vescent's, around 730 cm^3 and requiring fibre input for the laser light. The University of Nottingham presented an additively manufactured atomic spectroscopy module [77], 90 cm^3 in volume. The device requires three fibred laser inputs, which permits frequency stabilisation of the necessary laser frequencies to achieve laser cooling (see Chapter 4), as well as frequency tuning control as briefly mentioned above.

Chapter 3

Laser Frequency Stabilisation and Analysis

The Flame module and its ability to be frequency stabilised has been described in Chapter 2. It has been briefly discussed in Section 2.3.3 the typical laser requirements for suitability in laser cooling experiments. It is therefore imperative that the Flame modules are characterised in terms of their laser linewidth and frequency stability which are stringent parameters. Typically, ≤ 1 MHz linewidth is essential [23, 24], and a short-term (τ=1-10s) frequency stability in the range of 10^{-12} is desired for locked laser systems [70, 72, 78].

Frequency stability analysis is mostly achieved in the field by performing an Allan variance [79]. An Allan variance is a statistical tool which evaluates fractional frequency fluctuations of an oscillator. This is commonly achieved experimentally by beating two lasers of differing frequencies against one another at a photo-detector and recording the beat-frequency with a device such as a frequency counter. The recorded frequency data is then post-processed for stability analysis and an Allan variance is performed.

Let us firstly assume that the laser whose stability performance is pursued is beaten against a secondary laser whose frequency is not drifting with time. The stability of the beat note will then provide the frequency stability of the laser under test and will

have fractional frequency,

$$y(t) = \frac{f(t) - f_{av}}{f_0} = \frac{\Delta f}{f_0}, \tag{3.1}$$

where $f(t)$ is the measured beat frequency at a given time t, f_{av} is the average recorded beat frequency in the data-set and f_0 is the nominal laser frequency. The fluctuations in frequency during time t will then be equal to Δf.

This provides a fractional frequency array which the Allan variance is to be performed on. Let us first consider the non-overlapping version of an Allan variance, the original Allan variance proposed in [79],

$$\sigma_y^2(\tau) = \frac{1}{2(M-1)} \sum_{i=1}^{M-1} (y_{i+1} - y_i)^2 \tag{3.2}$$

where y_i are the i^{th} values of M $y(t)$ samples, averaged over an integration period τ.

The non-overlapping Allan variance has since been replaced with an overlapping version. This version considers all possible combinations of overlapping samples in the fractional frequency data-set for a given τ, increasing the confidence factor in the stability result. The overlapping Allan variance or deviation is the most frequently used method for frequency stability analysis [80].

$$\sigma_y^2(\tau) = \frac{1}{2m^2(M-2m+1)} \sum_{j=1}^{M-2m+1} \left\{ \sum_{i=j}^{j+m-1} (y_{i+m} - y_i) \right\}^2 \tag{3.3}$$

Here, $m = \tau/\tau_0$, where τ is the averaging time and τ_0 is the experiment measurement time.

Both Allan variance methods surpass standard variance methods, which are non-convergent for specific noise effects in the data-set. Figure 3.1 shows an example plot for the noise sources which are revealed after performing an Allan deviation to the fractional frequency data of an oscillator, where an Allan deviation is the square root of the variance, $\sigma_y(\tau)$. It is shown that the various noise effects are expressed by the slope of the Allan deviation.

Typical Allan deviation plots, similarly to Figure 3.1, start with initial improvements in the stability due to the averaging down of the noise at short τ. This slope

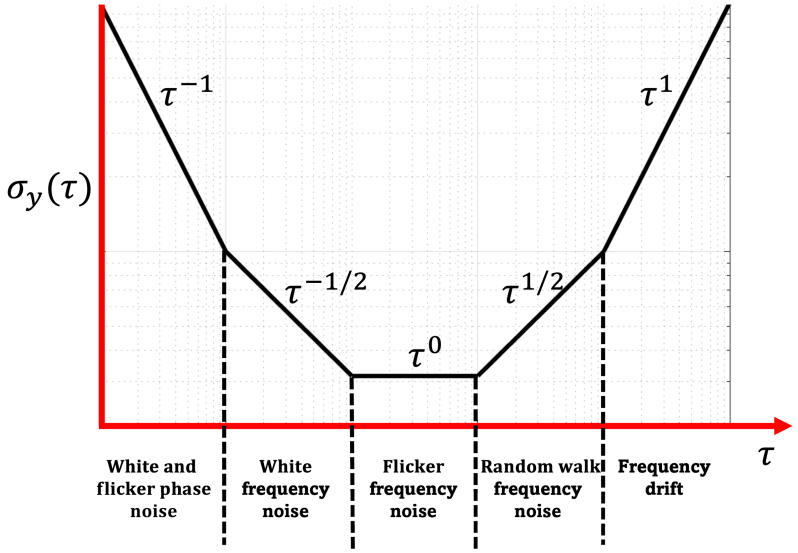

Figure 3.1: An example overlapping Allan deviation plot, depicting the various slopes that arise due to noise effects.

tends to flatten out when the noise floor of the experiment is reached, until inevitably rising and decreasing in stability due to averaging at longer τ. It is worth noting that the final points on a typical Allan deviation plot will show large error bars, as will be seen, due to averaging at long τ including a limited sample of $(y_{i+m} - y_i)$ values.

The overlapping Allan deviation is the tool of stability analysis used in this chapter to characterise the Flame module.

3.1 Experiment - The Three-Cornered Hat

In the introduction of this chapter, we discussed a method for assessing the frequency stability of a laser source. This method involved beating the laser against a secondary laser, recording the drift of the beat note, and then executing an overlapping Allan deviation analysis on the collected fractional frequency array. In this description, we made the assumption that the secondary laser is stable in frequency which in practice is not the case. In actual fact, a beat-note signal contains the relative frequency drift and noise from both laser sources. It is therefore the combined frequency stability of each laser that is observed in analysis, without means of determining which of the lasers are

contributing the most to the instabilities.

In this section, we implement a method which allows for the individual stability of a laser to be identified, allowing for the characterisation and development of the Flame module. This is achieved using a "three-cornered hat" experimental setup [81].

Described fully in [81], the three-cornered hat considers employing two or more reference oscillators to induce the stability of an oscillator under test. Consider three lasers A, B and C. Beating laser A with respect to B provides a combined frequency stability σ^2_{AB}. Similarly, beating laser A-C and B-C renders stabilities σ^2_{AC} and σ^2_{BC}, respectively. Assuming that these three lasers are independent of each other, their combined stabilities are therefore a product of the individual stabilities of each oscillator, and so we have,

$$\sigma^2_{AB} = \sigma^2_A + \sigma^2_B \tag{3.4}$$

$$\sigma^2_{AC} = \sigma^2_A + \sigma^2_C \tag{3.5}$$

$$\sigma^2_{BC} = \sigma^2_B + \sigma^2_C \tag{3.6}$$

It cannot be known with certainty the absolute stability of each oscillator following from these equations. Instead, the absolute stability of an individual component can be determined by employing simultaneous equations derived from equations 3.4 to 3.6.

$$\sigma^2_A = \frac{1}{2}(\sigma^2_{AB} + \sigma^2_{AC} - \sigma^2_{BC}) \tag{3.7}$$

Equation 3.7 conveys how a three-cornered hat can be executed for characterising the frequency stability of laser A, the laser under test. This technique is beneficial as it is an inexpensive and relatively simple evaluation for determining laser stability. Additionally, it is a seemingly obvious method for Alter to endorse in order to characterise future laser builds in-house, since multiple modules can be tested simultaneously.

It should be noted that although the three-cornered hat permits for the uncorrelated noise sources of each laser to be determined, any correlated sources will still be present in all three lasers. The three lasers and experimental setups to be detailed below will

be correlated in temperature, pressure and any acoustic noise as they were performed in the same laboratory simultaneously. They were however driven by independent laser drivers, locking electronics and spectroscopy setups. A secondary point to be highlighted is that the minus sign in Equation 3.7 signifies that the additional two lasers must be similar in stability to the laser under test, or the solved equation falls into a negative value due to noise.

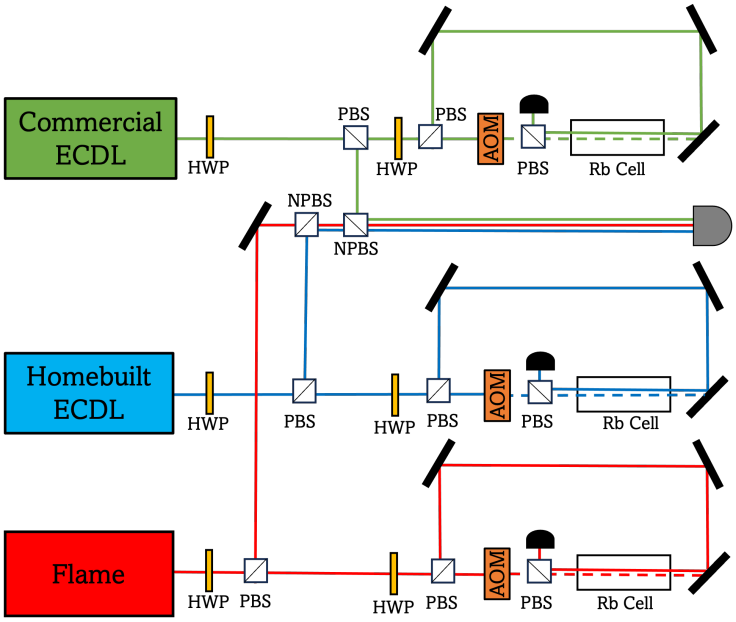

Figure 3.2: The experimental setup for the three-cornered hat. The three lasers to be tested are fibre launched to the experiment. Each laser is locked to a 7.5 cm Rb cell using SAS and frequency modulation of an AOM. This ensures only the pump beam is modulated (dashed lines). The clean probe signal from each laser is sent to a fast photodiode for beat-note measurements to be conducted. (HWP: half-waveplate, PBS: polarising beam splitter, NPBS: non-polarising beam-splitter)

Figure 3.2 displays the three-cornered hat experimental setup. There are three optical setups of SAS to allow for the locking of each individual laser. Two variations were made to how saturation absorption spectroscopy was achieved, specifically to how the pump beam was frequency modulated. In the first iterations of the experiment, for Figures 3.3 and 3.4, frequency modulation was specifically not applied to the laser itself, but instead to the pump beam only via an AOM. This was to initially establish a fair comparison of all three lasers, as frequency modulation couples into laser linewidth

broadening which is directly related to the modulation depth applied. A voltage controlled oscillator (VCO) (ZX95-200+) generated the RF for each AOM. The frequency modulation was supplied by a waveform generator, mixed with the VCO output using a bias-tee. The mixed signal was supplied to each AOM, with the modulation frequency and depth controlled by the frequency and amplitude at the waveform generator. These parameters were kept identical for all three AOMs. Each frequency modulation signal was additionally sent to the reference input of a LIA for appropriate demodulation of the SAS signal. The experimental setup from Figure 3.6 onwards is a result of direct current modulation applied to the lasers and will be explained within. Since the pump and probe beams have different frequencies, the resonance condition changes. The lasers no longer equally address the zero velocity class and instead their resonant velocity class is Doppler shifted from ω_0 by $\frac{2\pi\nu_{AOM}}{2}$.

The three lasers were fibre coupled and launched to the three-cornered hat breadboard. This was to ensure that each laser produced the same beam diameters and were collimated, for fair comparison and ease of beam-overlapping at the fast photodiode. The pump beam of each laser is frequency modulated at an AOM and directed to a 75 mm rubidium glass vapour cell. The probe light overlaps with the pump at the vapour cell and is reflected at the PBS to a photo-detector. Each laser is subsequently locked after demodulation at three separate lock-in amplifiers. A fragment of the light in each set-up is picked off for the probe to be directed to a fast-photodiode which detects the beat-note signals of each two-laser combination. The beat-notes are optimised using an RF spectral analyser, with one of the three beams blocked for the beginning of the experiment. The beat-note signal is conveyed to a frequency counter, wherein the central frequencies are recorded. This is repeated until we have three beat recordings, A-B, B-C and A-C. An overlapping Allan deviation is performed on each beat note using software Stable32 [82]. After the Allan deviation for each laser pair is determined, the three-cornered hat can be executed. For each of the Allan deviation plots to come, the data-sets were recorded over a period of 5 minutes. It should also be noted that the systems were in a steady-state before starting the experiment.

Figure 3.3 shows the overlapping Allan deviations for each two-laser combination

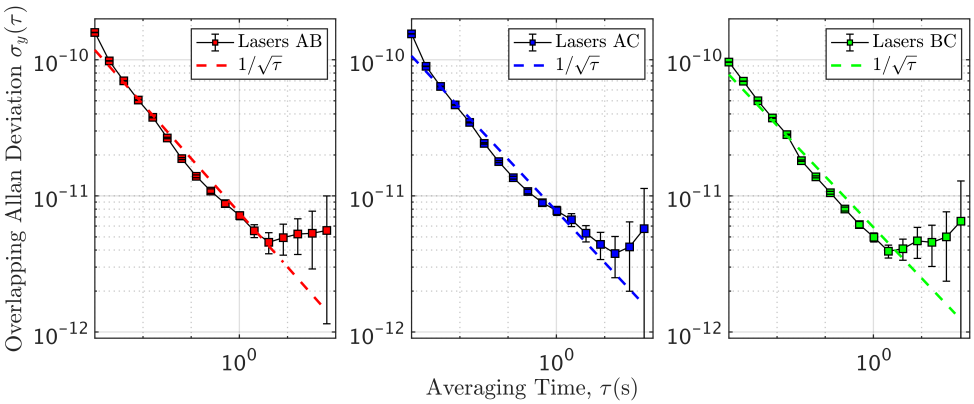

Figure 3.3: The overlapping Allan deviations for each of the two laser combinations. Laser A is a commercial ECDL, B a home-built ECDL and C is the Flame. A $1/\sqrt{\tau}$ fit has been added to each, corresponding to the dashed line in each plot.

where Laser A, B and C is a commercial ECDL, a home-built ECDL and the Flame (a DBR configuration), respectively. A $1/\sqrt{\tau}$ fit was applied to the data to show that the limiting noise in the experiment is white frequency modulation (FM) noise at about $\tau = 2s$. Each laser combination hits around 4×10^{-12} before another type of noise begins to dominate. Initial observation of the three presented plots in Figure 3.3 show similar Allan deviation plots for each of the paired lasers, however, a conclusive answer to the frequency stability portrayed by each individual laser is possible by a three-cornered hat execution.

Figure 3.4 shows the overlapping Allan deviation from the three-cornered hat analysis of the three lasers under test. The presented data leads to the conclusion that the three tested lasers exhibit comparable frequency stabilities when locked to similar spectroscopy setups. This finding was considered a positive result, specifically for the Flame as it demonstrated that there were no inherent issues with the laser and its accompanying electronics to cause unlocking or laser frequency drifts. This development was a beneficial step towards establishing the Flame as a competitive laser in the market, achieving parity with other commercially available products.

The laser diode configuration of the Flame is a DBR, which are presumed to be wider in laser linewidth than ECDL's due to their shorter cavities (see Section 2.1). Interestingly, the seemingly larger linewidth has not contributed to frequency insta-

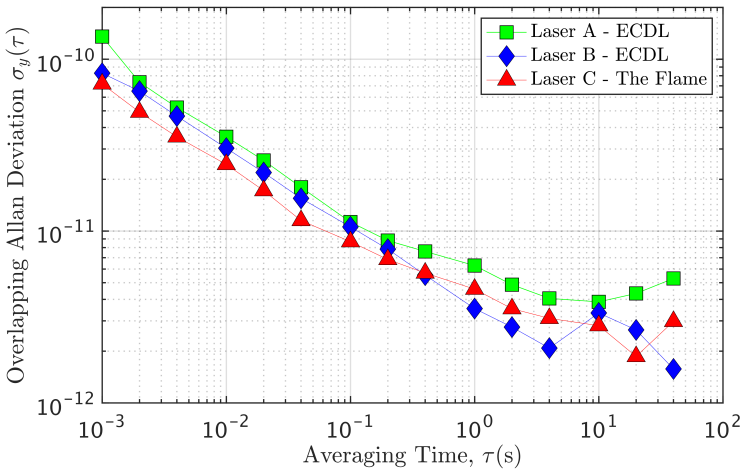

Figure 3.4: The result of the three-cornered hat, outlining the individual frequency stability of the three lasers under test. The three lasers are considered equal in terms of their stability following this analysis.

bilities when compared to ECDLs. To prove this, the beat-note signal for each laser pairing was recorded, each at approximately 2 seconds measurement time. Figure 3.5 shows the three beat-note signals with Lorentzian fits and their FWHM shown.

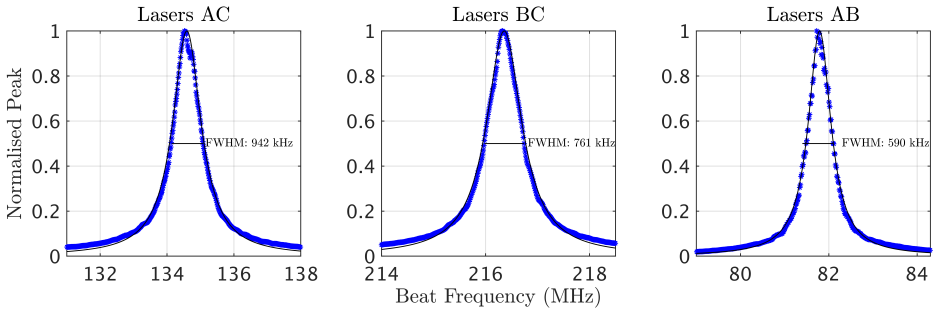

Figure 3.5: Beat-note measurements at a 2 second measurement time for each of the two-laser combinations. Their full-width half-maximum linewidths have been labelled in each for comparison of laser linewidth.

Similarly to the three-cornered hat analysis, simultaneous equations can be used to estimate the laser linewidth at a 2 second measurement time for each laser. This gives laser linewidth's of approximately 386 kHz, 204 kHz and 556 kHz for lasers A, B and C, respectively. The linewidth of the laser therefore does not have an effect on the frequency stability in this experiment. Additionally, Figures 3.4 and 3.5 validate that

the Flame's linewidth and stability are satisfactory values for laser cooling applications.

3.2 Experiment - The Flame's Internal Lock vs External

Demonstrating that identical spectroscopy and locking methods gave alike Allan deviations allowed for future demonstrations to use only two lasers in analysis and the three-cornered hat was no longer implemented. A valuable analogy could then be established by comparing the Flame's laser frequency stability when locked to a standard 75 mm rubidium vapour cell against its internal cell, which measures 12 mm in length. This would be a key insight into demonstrating the main asset and benefit of the laser module, which is the internal locking of its spectroscopy. For this demonstration, both lasers used were switched to current modulation and the AOM's were removed from the setups. This was to allow for an impartial comparison of techniques as to stabilise the Flame to the internal cell of the module, the module must be current modulated as described in Section 2.4.3. The Flame's cell heater was heated to achieve optimal absorption, around 45 °C.

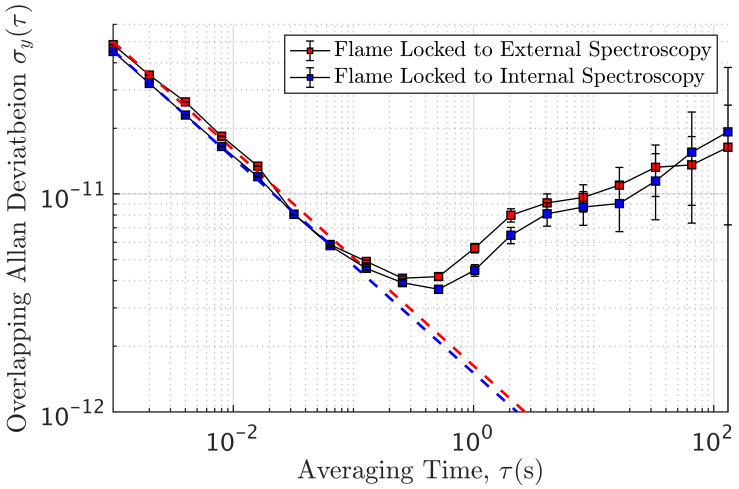

Figure 3.6: Comparison of the Flame laser locked to an external SAS setup to the internal spectroscopy arm of the module. The Flame is beaten against an ECDL for both configurations and the setup has been switched to current modulation with the AOM removed.

Figure 3.6 shows the overlapping Allan deviations for the Flame when locked to

an external SAS setup, to the internal SAS of the module. These Allan deviations were the result of the Flame and one of the two ECDLs from the previous plots beaten against one another, where it is deemed not important which of the ECDLs were used considering the result of Figure 3.4 and the three-cornered hat.

It is clearly observed that regardless of the spectroscopy setup that the laser is stabilised to, the stability of the laser frequency is the same. This is an extremely favourable outcome for the Flame. It can be concluded that the module can achieve frequency stabilities with deviations in the kHz range, competent for cold-atom applications, and that this can be executed within its 60 x 40 mm module footprint. Figure 3.6 is showing that bulky laboratory based setups can confidently be reduced in the form of Alter's Flame module.

Comparing Figure 3.6 to any of the three plots in Figure 3.3 shows a slightly lower stability but at a much quicker degradation of stability for the current modulation technique. It is believed the lower stability is due to a slightly tighter laser lock being achieved with the current modulation method for this particular measurement. The stability of this lock then degrades much faster, likely due to the inherent instability introduced by modulating the laser current directly to achieve frequency modulation of the pump beam.

3.3 Conclusion

The results presented in this chapter show a focus on short-term frequency stabilities, with early rises in the Allan deviation plots observed at around 1 second. Various factors are believed to be the cause of this. For example, the intensity of the lasers, as well as the cell temperatures were not stabilised. For the locking of the lasers via current modulation, the error signals were Doppler background limited, meaning any change to the absorption signal due to laser intensity or temperature drifts would have a direct impact on the error lock point. These parameters would need to be stabilised and investigated further if long-term stability measurements were desired. Additionally, a non-Doppler limited background of the error signal can be achieved using a third-

derivative approach [83].

In this chapter, we explored using a three-cornered hat experimental setup in order to investigate the individual frequency stability of the Flame. From this, we were able to draw the conclusion that it was equally effective to use only two lasers for our laser stability analysis. This simplified future evaluations, and the Flame was then analysed by beating it against just one other laser source.

It is noteworthy that this represents the first instance of frequency stability measurements conducted with a Flame device. The stability reached using the Flame's internal spectroscopy for stabilisation was around $5\text{x}10^{-12}$ at 1 second, demonstrating kHz deviations from the lock point. This proves the Flame's feasibility in laser cooling applications from within its 36 cm^3 package, matching well with integrated laser systems published in the literature at similar integration times [70–72, 78].

Chapter 4

Magneto-Optical Traps

In the late 20^{th} century, great interest emerged in using laser radiation to manipulate and cool particles. After the initial proposal in 1975 by Hänsch and Schawlow [3], the concept of laser light potentially decelerating atomic motion spurred extensive experimental research and investigation [4–7].

In this chapter, the Flame is demonstrated in a portable magneto-optical trap experimental setup. Laser cooled atoms are the first step in various precision applications, such as atom interferometry and atomic clocks. Additionally, there has been a push in recent times towards utilising laser cooled atoms for field-deployable quantum sensors. This has involved the development of the various components which make the experiment, with SWaP reduction being pivotal for progress in the field.

Testing the laser in a quantum technology experiment was the next step in validating the Flame's functionality, following from the frequency stability evaluation shown in Chapter 3.

4.1 Laser Cooling

Introduced in this section are the basic principles to describe the method of laser cooling atoms. Photon momentum, $\hbar k$, is transferred to an atom amid atom-light interactions.

An excited atom is recoiled parallel to the direction of the light with momentum,

$$p = mv = \hbar k \tag{4.1}$$

where m is the atom mass and v the atom velocity. The velocity is therefore modified by $v = \frac{\hbar k}{m}$. The atom emits a photon of frequency ω_0 in a random direction upon decay, enduring another velocity change v in a direction opposite the emitted photon. This presents no net change in atom momentum over multiple absorption cycles. The atom therefore experiences a change in velocity dependent exclusively on the incoming laser light. An exerted force, F_{scatt}, accelerates or decelerates the atom as the photon absorption and emission cycle continues. F_{scatt} can be described as,

$$F_{scatt} = \frac{\Delta p}{\Delta t} = \frac{\Delta p}{1/R_{scatt}} \tag{4.2}$$

where R_{scatt} is the scattering rate of the photons, related to the natural linewidth (Γ) of an atomic transition and the fraction of the population of atoms in the excited state (ρ_{22}). This becomes,

$$R_{scatt} = \frac{\Gamma}{2} \frac{I/I_{sat}}{(1 + I/I_{sat} + 4\delta^2/\Gamma^2)} \tag{4.3}$$

Here, δ=($\omega_L - \omega_0$) is the laser detuning from resonance, I is the intensity of the light and I_{sat} is the saturation intensity of the atoms. The scattering force then becomes,

$$F_{scatt} = \hbar k \frac{\Gamma}{2} \frac{I/I_{sat}}{(1 + I/I_{sat} + 4\delta^2/\Gamma^2)} \tag{4.4}$$

The scattering force, however, exerts its influence solely in one direction and does not consider the Doppler shift experienced by the moving atoms.

Consider instead two counter-propagating lasers whose frequencies are red-shifted, $\omega_L < \omega_0$. The light appears as blue-shifted for atoms which travel toward a laser attributable to the Doppler effect, therefore absorbing more photons from that laser. Equation 4.3 can be slightly modified to account for the laser detuning from resonance,

$$R_{scatt} = \frac{\Gamma}{2} \frac{I/I_{sat}}{(1 + I/I_{sat} + 4(\delta \pm kv)^2/\Gamma^2)} \tag{4.5}$$

The total force influencing the atoms is now a consideration of each laser's respective scattering rates,

$$F_{tot} = \frac{\hbar k \Gamma}{2} \left(\frac{I/I_{sat}}{1 + I/I_{sat} + 4(\delta - kv)^2/\Gamma^2} - \frac{I/I_{sat}}{1 + I/I_{sat} + 4(\delta + kv)^2/\Gamma^2} \right) \tag{4.6}$$

Equation 4.6 reveals that the force exerted on an atom is dependent on the atom velocity. This relation is shown analytically in Figure 4.1, where the black solid line shows the total force acting upon an atom as a function of its velocity and the dashed lines the applied force from each laser. The force applied is positive (negative) for an atom travelling with negative (positive) velocity, ensuring deceleration of the atom.

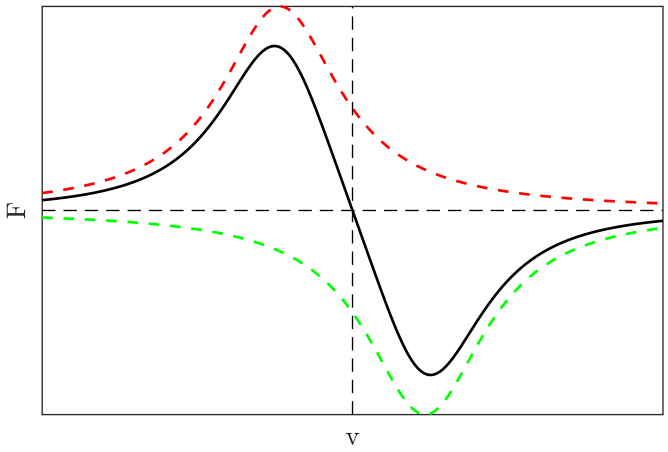

Figure 4.1: The velocity dependent force which acts on an atom in an optical molasses. The black line depicts the combined force due to the counter-propagating lasers. In this example, I=I_{sat}.

For efficient atom cooling in three dimensions, three pairs of counter-propagating lasers can be utilised. This technique is coined optical molasses, based on the Doppler cooling mechanism. Although the optical molasses technique has the ability to cool atoms, it is not effective in trapping them.

4.2 Trapping

Integrating the damping force described above with the Zeeman effect gives a position dependent force which confines the atoms as well as cooling them, known as a magneto-optical trap (MOT). The position dependent force is created by the introduction of a magnetic field. This breaks the degeneracy of the hyperfine (F) levels of an atom, introducing $2F+1$ magnetic sublevels (m_F) to the atomic structure which was discussed in Section 2.2.1. The energy shift of the sublevels with respect to a low magnetic field $\overrightarrow{B}$ is,

$$\Delta E = \mu_B g_F m_F \overrightarrow{B} \tag{4.7}$$

where μ_B is the Bohr magneton $\frac{e\hbar}{2m_e}$ of an atom with electron charge e and mass m_e, and g_F is the Landé g-factor, equal to -1/2 and +1/2 for F=1 and F=2 respectively for ^{87}Rb. This gives a linear split in energy at low magnetic fields, and is known as the Zeeman effect.

The Zeeman sublevels therefore increase with respect to the applied $\overrightarrow{B}$-field. To understand how this mechanism is applied for trapping atoms, we refer to Figure 4.2 below. This is a hypothetical example for basic understanding of the working principle.

In this example, we consider a F=0 to F'=1 transition. The F'=1 state will have m_F levels -1, 0 and +1 attributable to the applied magnetic field $\overrightarrow{B}$. Transitions which change m_F sublevels by -1, 0 and +1 are described as σ^-, π and σ^+ transitions, respectively, driven by the specific polarisation of the induced light. Selections rules dictate that light that is right (left) circularly polarised will induce σ^+ (σ^-) transitions, when the applied $\overrightarrow{B}$-field is (anti-)parallel to the light propagation. The figure shows two circularly polarised lasers of opposite-handedness red-detuned from ω_0. An atom travelling in the positive x-direction will interact and absorb more photons from the σ^- beam, forcing the atom into the centre of the trap through the damping force described in section 4.1. An opposing force is applied to atoms moving in the opposite direction upon interaction with σ^+ light. Thus, a position dependent force is realised as the atom is brought closer to resonance whichever direction it travels, pushing the atom towards the trap centre.

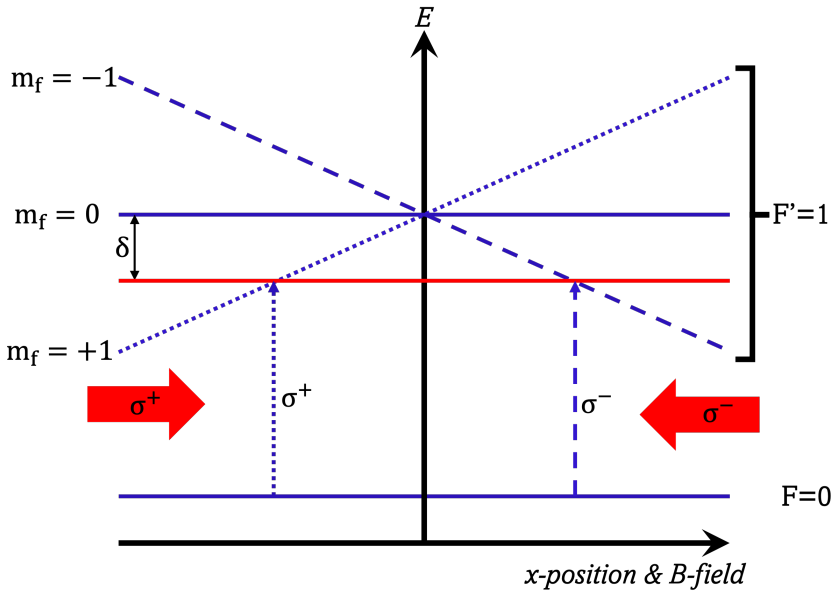

Figure 4.2: A simplified version of a one-dimensional magneto-optical trap. A $\overrightarrow{B}$-field is applied increasing with magnitude in the positive x-direction. This introduces m_F sublevels on the F'=1 transition from -1 to 1. Two counter-propagating lasers are red-detuned from ω_0, circularly polarised with opposite handedness.

The example above oversimplifies the concept of a MOT. In practice, a pair of anti-Helmholtz coils is employed, ensuring that the magnetic field at the trap centre is zero. The magnetic field then increases proportionally with distance in both the positive and negative x-directions. The method is easily applied in three dimensions by using three pairs of counter-propagating beams in each direction for most effective cooling and trapping.

4.3 Grating MOTs

The two laser beams essential for each dimension of cooling in MOTs require a considerable amount of optics. Reducing the number of laser beams is therefore a key step in reducing the size of the experimental apparatus. The development of the pyramid MOT, as detailed in [13], introduced the application of applying a single incident beam on a pyramidal hollow mirror to effectively generate the three pairs of counter-propagating beams, mirroring the configuration found in a conventional MOT. This idea extended

to tetrahedral-MOTs [84] which permitted for improved optical access using angled-mirrors, realising a four-beam MOT. The most significant development, however, came from the tetrahedral configuration being formed from the first-order diffraction of a single incident beam using microfabricated gratings [14]. These diffracted beams achieve the balance of radiation pressure from the incident beam to permit for laser cooling in three-dimensions. A schematic of a gMOT configuration is shown in Figure 4.3. The introduction of the grating magneto-optical trap (gMOT) enabled the significant reduction in both the space and components necessary for cooling and trapping atoms. Furthermore, gMOTs offer the advantage of simplified optical alignment and integration into the apparatus, facilitated by the planar nature of the optic.

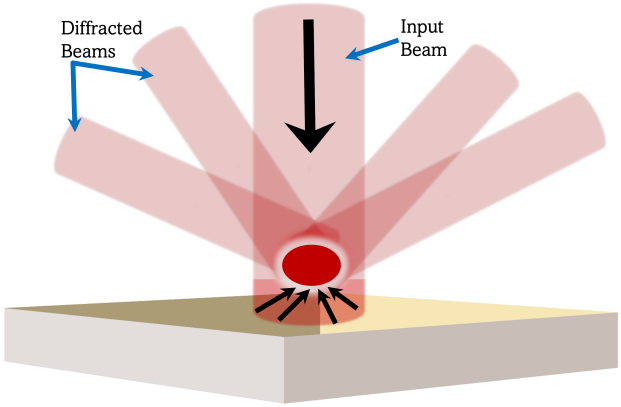

Figure 4.3: Schematic of a grating MOT chip. A single input beam is diffracted at the grating surface to form the beams necessary for laser cooling. Not included in the schematic are the anti-Helmholtz coils.

The description of the optics and mechanisms which describe MOTs have so far neglected another essential component for effective laser cooling. Ultra-high vacuum (UHV) chambers are implemented to mitigate thermal collisions of the rubidium atoms with background gases, actively pumped in the range of 10^{-7} mbar [85] by an ion pump. The alkali is then released into the chamber typically by dispensers. For the configuration used in this chapter, a gMOT chip has been integrated into a vacuum cell with attached dispensers and ion pump. We refer to this as a gMOT cell, which requires the input of a single beam and anti-Helmholtz coils for the creation of laser

cooled atoms. In this chapter, we test a commercial, compact gMOT package fabricated by CPI-TMD [86] along with a Flame laser module to demonstrate a portable magneto-optical trap.

4.4 Experiment - Portable Magneto-Optical Trap

The experiment introduced in this chapter aimed to determine the capabilities of a compact and portable cold-atom system on a mobile platform. The motivation for this reverts back to the ideas presented already in this thesis. It has been highlighted that there has been significant funding in the past decade directed towards reducing the SWaP consumption of the components integral to quantum technologies. Demonstrating a MOT in a portable manner therefore aligns with this objective.

The total system presented in this chapter incorporates two main compact quantum technologies. The Flame to provide the frequency stabilised laser light, from Alter UK, and a gMOT vacuum chamber package by CPI-TMD. This experiment thus explores the integration of commercial quantum technology products for demonstration of a transportable magneto-optical trap.

An overview of the cold-atom platform is described, with the various structural elements split into individual sub-sections. The fabricated sensor is a first-version attempt. The challenges entailed in transforming a portable system from what is typically an extremely bulky and lab-based experiment are discussed.

4.4.1 Experimental Setup

The experimental setup was split into multiple subsystems as depicted in Figure 4.4. The individual components are colour coded to outline the individual 19" rack cases, combined to give the overall system. The sub-systems are explained in further detail below.

• Laser Driver - This is the electronics used to stabilise the laser frequency. A commercial DLC is used to drive and lock the laser. A trans-impedence amplifier is essential for amplifying the photodiode signal before it reaches the DLC's lock-in

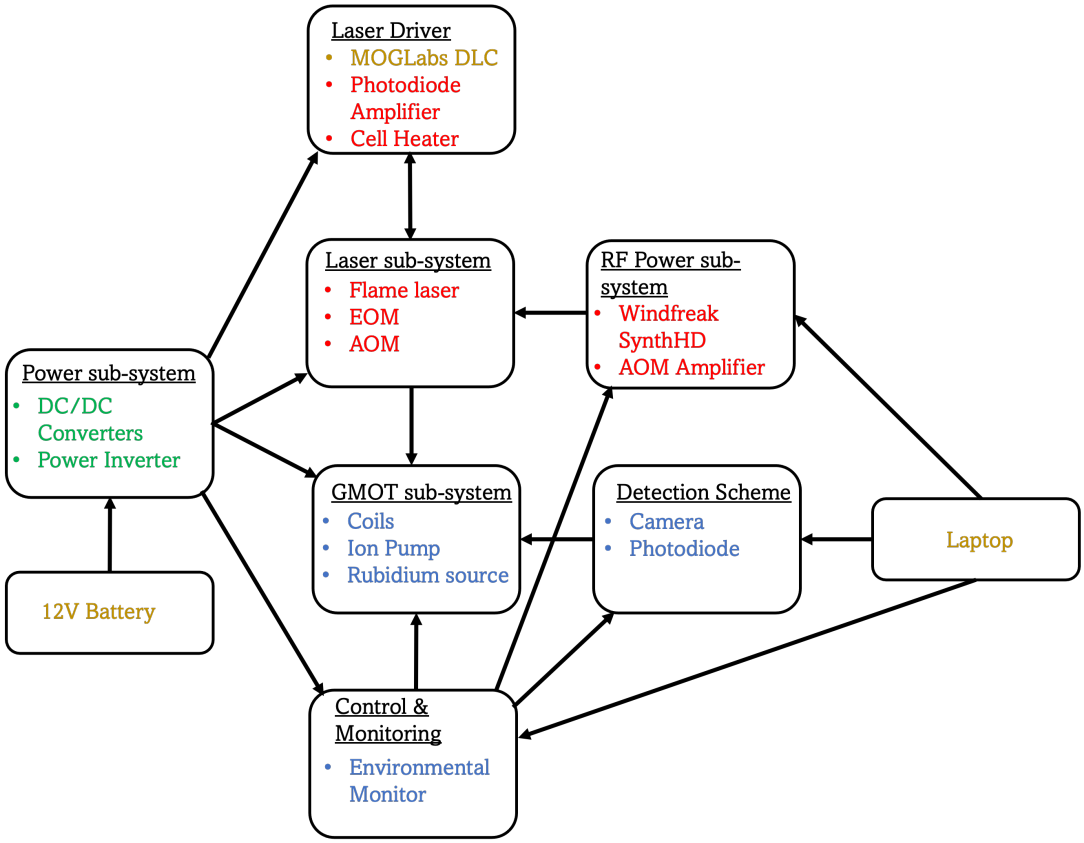

Figure 4.4: The various sub-systems which the cold-atom system is comprised of. The colours of each component are representative of the rack case they were constructed in.

amplifier. This is a custom PCB and is described in Chapter 2. Also discussed in Chapter 2 is the requirement to heat the integrated vapour cell of the Flame to increase the density of the rubidium atoms. This is done by applying current to a wire wrapped around the cell.

• Laser sub-system - This sub-system provides the light for laser cooling the atoms. The laser module used is a 780 nm Flame, frequency stabilised to the integrated rubidium cell. An EOM is used for the required repump light in the laser cooling process. An AOM in a double-pass configuration allows for the control of the laser frequency and intensity. The laser light is then fibre coupled, to be delivered to the fibre input of the gMOT subsystem.

• RF Power sub-system - Windfreak Synth HD devices are used to generate the RF frequencies required for the AOM and EOM devices. The AOM requires around

30 dBm of RF power provided by an RF amplifier.

• gMOT system - This is the cold atom sub-system, CPI-TMD's compact grating magneto-optical trap. This device contains a vacuum cell with an integrated grating chip to allow for the generation of cold atoms, with accompanying optical beam delivery coming from an optical fibre input. Additionally incorporated in this package are the required electronics to drive the MOT coils, the ion-pump and the rubidium dispensers.

• Detection Scheme - This is the sub-system for detecting the atoms. A camera takes triggered images of the atoms, with a photodiode in place for detection of the MOT fluorescence.

• Control and Monitoring - A custom electronic board was created to monitor the environment during deployment, as well as to implement control sequences on the system. The environmental monitor records the temperature, humidity, magnetic fields, accelerations and location and is controlled by a RasberryPi Pico board.

• Laptop - A laptop is used to control the RF power, the control and monitoring sub-system and to process the MOT images from the detection scheme.

• Power sub-system - This system converts the power from a car battery to the required voltages to drive the majority of the system. Multiple DC/DC power supplies are used for conversion of the 12V DC battery to the +5V, +24V and -24V DC needed for various components. Additionally, a power inverter was chosen to generate the 230V AC necessary for components such as the DLC, laptop chargers and multi-socket extension cords.

• Battery - An 110Ah 12V car battery is used to power the entire system.

These various sub-systems were then packaged into five 19" rack cases (laptop not included), where the colours illustrated in Figure 4.4 indicate the components which make up each rack. The number of rack units per case is shown in Table 4.1 below, in addition to the total estimated power budget for each rack.

Figure 4.5 shows an image of the overall portable system built in this project. The total volume of the rack cabinet chosen was 18U. This gave an extra 3U of space, of which could be utilised for a shim-rack in future builds. A stretch goal of the project was to incorporate magnetic shim coils in order to cancel background magnetic fields. This

	Rack Units	Estimated Power Budget
MOGLabs DLC	2U	70W
gMOT Rack	3U	22W
Laser Rack	3U	19W
Power Rack	2U	Not Applicable
Car Battery	5U	Not Applicable
Total:	**15U**	**111W**

Table 4.1: Estimated power budget and total size in rack units for the system. For the laser rack, the components considered are the Flame's cell heater (1W), the AOM amplifier (12W) and the WindFreak device which drives the AOM and EOM. For the gMOT rack, the individual components are the gMOT package (15W) and the environmental detection and control board (7W).

was eventually not implemented due to time constraints but is hoped to be considered in future iterations. The sub-sections which follow display images of each of the racks with a detailed analysis of the components.

Power Rack -

Figure 4.6 shows images of the power rack. The power to the rack is facilitated via a 12V DC car battery. Figure 4.6a shows the custom designed, panel mounted rack wall for the power rack. This was designed with safety, robustness and practicality in mind. Starting from left to right, these include a plug socket for the AC-powered components, an international electrotechnical commission (IEC) lead-input delivering the 12V from the battery, and a power-switch connected to the IEC lead for safety. Finally, presented are RS PRO heavy-duty power connectors (part number 171-5732), designed to endure currents of up to 16A. These connectors are interfaced to the output of the DC/DC converters, enabling the power transfer to the other racks.

The interior of the rack is depicted in Figure 4.6b. Starting from the bottom left is the power inverter used to convert the 12V DC to the 230V AC necessary for powering AC devices, such as the DLC. The exact model shown in the image is RS Pro model 816-0034, however, this was not the device used in deployment and will be discussed in

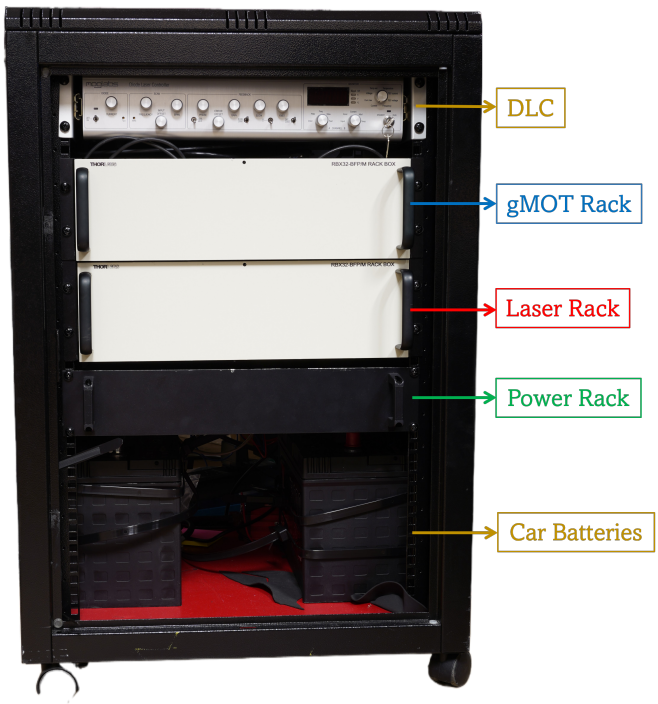

Figure 4.5: The portable cold atom system fabricated in this chapter, with each rack and individual component labelled. The sensor is 60 cm L x 60 cm D x 90 cm H in volume.

Section 4.4.2. The device was screwed to the rack wall for convenient connection to the plug socket output. Following from the inverter are the the DC/DC converters. From left to right these are 5V, +24V and -24V devices. The 5V DC was required to power the Flame's integrated vapour cell and environmental monitoring device. The AOM RF amplifier required +24V, and the -24V was included to power the shim-rack. The shim-rack was not implemented due to time constraints, though is expected to be included in future iterations of the system. The power from each of the DC/DC converters is connected to the socket version of the RS PRO heavy-duty power connectors (part number 171-5733). The sockets are screwed securely to the rack wall.

Laser Rack -

Figure 4.7 shows an image and labelled drawing of the laser rack. This rack consists of the optical breadboard and fibre launch, the RF components and the necessary

(a) (b)

Figure 4.6: Photograph of the power rack displayed at different angles. (a) The custom designed rack wall. From left to right: a plug socket to the power inverter, an IEC lead supplying the power from the battery, a power switch and three connectors which interface with the DC/DC converters for the transfer of power to the gMOT and laser racks. (b) The interior of the power rack. Left to right: the power inverter, a 5V DC/DC converter, a +24V DC/DC and a -24V DC/DC.

electronics to drive them. The top section of the figure shows the custom designed rack wall of the laser rack. Additionally, a pound coin is shown on the left-hand side of the rack to gauge the compact size of the optical components.

The 780 nm Flame module used is driven and frequency stabilised by a MOGLabs DLC. The electronic breakout board for the DLC is panel mounted to the rack, 'DLC Board' in the labelled figure of Figure 4.7. The DLC Board is connected to the appropriate pins of the custom PCB Flame driver. Described in Section 2.4.6, the Flame PCB driver interfaces the Flame laser with the electrical components to drive and lock the module. A SubMiniature version A (SMA) cable connects the photodiode output signal of the Flame to the rack wall via 'SMA Connector', interfaced with the input of the trans-impedance amplifier on the other side of the wall. Additionally wired to the Flame PCB is the vapour cell heater. This gets powered by 5V DC, obtained from the power rack, wired via 'Power Connector' on the labelled image. A resistor was connected in series to reduce the current induced.

Additionally labelled are the devices which drive the AOM and EOM, a WindFreak

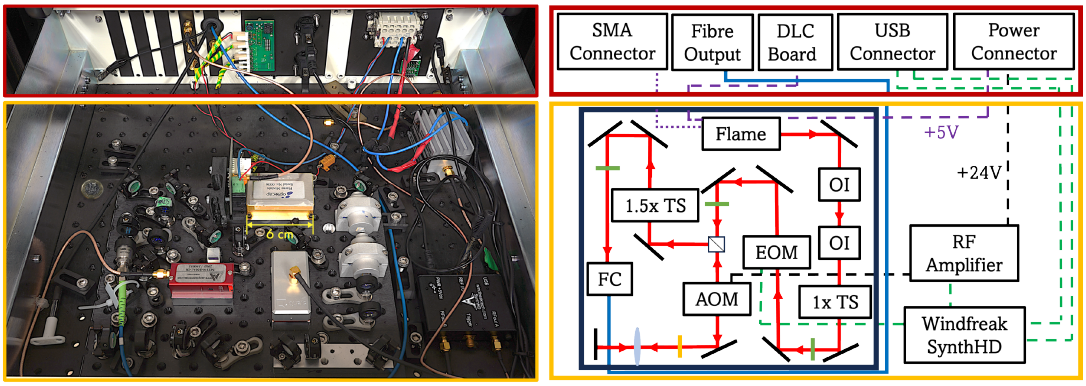

Figure 4.7: Photograph of the laser rack aligned with a labelled schematic. The top red boxes show the rack-wall of the laser rack. The panel mounted components needed were an SMA connector, grommet hole for the fibre transfer, the MOGLabs electronic driver board, universal serial bus (USB) connectors and power connectors which transfer the DC voltages from the power rack. The yellow boxes show the laser bread-board, an RF amplifier and a WindFreak SynthHD device. This device supplies the RF powers and frequencies for the AOM and EOM devices. The beam path is depicted, where green and orange rectangles represent half-waveplates and quarter-waveplates, respectively. (OI: optical isolator, TS: telescope, FC: fibre-collimator)

SynthHD and an RF amplifier for the AOM. The WindFreak outputs the RF powers and frequencies for the EOM and AOM devices. The device is both powered and controlled via USB connection to the laptop, interfaced using the 'USB Connector' on the rack wall. The RF amplifier amplifies the WindFreak signal intended for the AOM by 30 dB and is powered by +24V DC from the power rack.

Finally, there are incorporated grommet holes mounted on the rack for the optical fibre and temperature probes from the environmental monitor to be inserted through for travel to the other racks. This is labelled as 'Fibre Output' on Figure 4.7.

The optical breadboard is highlighted (black) with the beam path depicted. For the optical components, Thorlabs miniseries range was chosen [87]. These components are more compact, lighter and less vibrationally sensitive than standard components used in labs. This permitted the size of the optical breadboard to be reduced significantly. Pedestal posts 12.5 mm in height (MSP05/M) were chosen, which include pre-mounted set screws for the mounting of the optical components. These posts are then secured onto the breadboard with clamping forks and therefore the heights of these components

are not adjustable. Custom mounts of aluminium were machined to account for the set height of the optical components. This was for securing the Flame, optical isolators, EOM, AOM, as well as a few of the optics to the breadboard.

The Flame laser used generates 150 mW of 780 nm light. The beam is directed towards two optical isolators. To accommodate the restricted breadboard size, it was necessary to source optical isolators in smaller form factors with large beam apertures. EOT Tornos optical isolators (OIs) provide around 33 dB of optical isolation, a 4 mm aperture and are 40 mm long. Optical isolators, especially to such a high degree of isolation, have proven to be crucial for Flame modules designed for fibre-coupling. This is discussed and demonstrated in Section 2.4.8. The beam is then recollimated by a 1:1 telescope (TS) before being directed to an EOM. The EOM procured is from QUBIG (PM-RB-6.6), used to produce the optical side-bands necessary for the repump light in the laser cooling stage (∼3%). This device is powered by 20 dBm of 6.574 GHz of RF power via the WindFreak, which is the maximum power output available using a WindFreak device.

Following from the EOM, the beam travels to a PBS where the majority of the light is transmitted. The polarisation of the light is controlled and optimised by a half wave-plate (HWP), depicted as green rectangles in Figure 4.7. The transmitted light enters a double-pass AOM configuration with a cat-eye lens setup. This is to ensure the beam is not misaligned as the frequency of the AOM is altered in the optical molasses stage of the experiment. A 110 MHz AA Opto-Electronic AOM (MT110-A1-IR) was chosen and in steady-state MOT operation was employed at 101.45 MHz with -4 dBm of RF power delivered via the WindFreak. This was amplified by a 31 dBm AA Opto-Electronic RF amplifier (AMPB-34-10.500). This enabled the laser to be around 10 MHz detuned from the F'=3 cooling transition of ^{87}Rb, with the Flame locked to the F=2→F'=1 & 3 crossover transition of its integrated cell. The polarisation of the light was optimised to ensure that the majority of the light is reflected at the PBS after the double pass of the AOM using a quarter-wave plate, orange rectangle in the labelled figure. A second telescope was included in the beam path to increase the beam by 1.5x to optimise the fibre coupling (FC). The light is then fibre launched via a polarising

maintaining fibre, which travels to the 'Fibre Output' grommet hole for insertion to the gMOT rack.

Finally, a 3D printed mount was fabricated in order to secure in place the Flame PCB driver and ZIF plug connector which is attached to the 12-pins of the module. This was to mitigate concerns that whilst the system was in motion, the ZIF connector would respond to the vibrations, causing strain on the module pins, loose connections or permanent damage. The back of the PCB was secured to the wall of the mount via nylon screws and can be seen seen on the picture image of Figure 4.7.

The laser sub-system provides 23 mW of laser cooling light from the output of the polarisation maintaining fibre, a sufficient value for generating cold atoms in a gMOT configuration [15,88,89]. The majority of the optical loss is from the double pass AOM configuration, where around 54% of light is lost (83% diffraction efficiency in the first pass and 65% in the second). The fibre coupling efficiency is around 50% which is also a major factor of optical power loss. The footprint of the laser breadboard is 20 x 25 cm with the highest point around 7 cm, leaving ample space in the 3U 19" rack chosen for the laser rack of the system.

The next stage of miniaturisation for the laser rack could include fibred optical components. This would undoubtedly reduce the volume of the breadboard, whilst mitigating the risk of optical misalignments. Fibred Flame devices are in development at Alter and could be used in future iterations of this system with fibred EOM and AOM devices.

gMOT, Control and Detection Rack -

The rack which integrates the gMOT package as well as the control, monitoring and detection sub-system is shown in Figure 4.8. The rack-wall was once again custom designed to interface with the laser and power racks.

CPI-TMD's gMOT sub-system consists of an ultra-high vacuum cell with an integrated grating, allowing for the conditions to create and trap cold atoms with beam-delivering optics and coils. This is all contained within a 33 x 8.8 x 10.4 cm package, including an electronic board which drives the MOT coils, ion-pump and rubidium

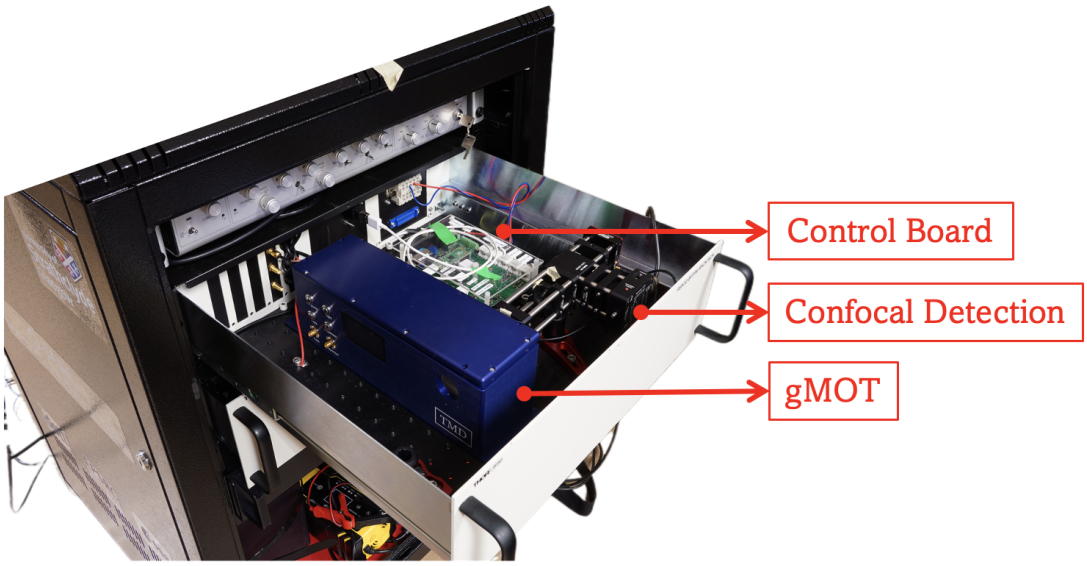

Figure 4.8: Labelled image of the gMOT rack. This rack is comprised of the gMOT vacuum package, the detection scheme and the electronic control board.

dispensers. All that is needed from the user is 5V DC, and the laser light delivered via the optical fibre input, which comes from the laser rack as described above.

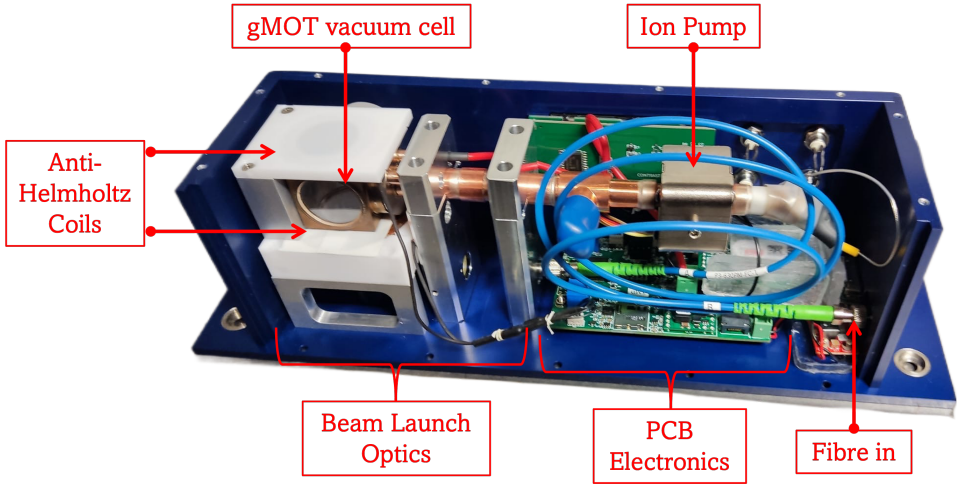

Figure 4.9: The interior of CPI-TMD's gMOT package. The cooling and re-pump light enter at fibre in and are beam-launched to the grating MOT vacuum cell. A pair of anti-Helmholtz coils sit directly above and below the cell to ensure that the applied magnetic field is zero at the MOT location. The PCB which powers the coils, ion pump and dispensers is shown.

Figure 4.9 shows a labelled image of the gMOT package with its lid removed revealing the internal components. The fibre from the laser rack is input at 'Fibre In'. A separate, internal fibre of the gMOT then launches the light towards a quarter waveplate to achieve the required circularly polarised light, as described in Section 4.2. The circular light hits a mirror and is directed towards a quad grating chip where four diffracted orders are generated. Magnetic coils in an anti-Helmholtz configuration sit directly above and below the gMOT cell, as labelled. Some alterations to the coil resistance was necessary to successfully produce the magnetic field gradient (∼15 G/cm) needed for atom trapping when powering the coils from the PCB. The 5V DC to power the device can be provided from either USB power from a laptop or from the 5V supplied from the power rack.

The detection and control schemes were tasks assigned to a colleague and electronic engineer, respectively. The PCB for in-house control and environmental monitoring is managed by a Raspberry Pi Pico through serial commands. Table 4.2 outlines the control hardware and their output channel objectives. The implementation of the control board communication to the physical components was an assigned responsibility of a colleague. This was executed as a guided user interface (GUI), written on PYQt5. Due to time constraints, some of the implementations were not executed. Control of the gMOT coils and dispensers was not executed due to issues with the gMOT PCB. It was found that the push switches for the magnetic coils did not offload the current to the coils fully when switched off, and so this control was not implemented. Switching off of the MOT was instead controlled by powering down the RF power to the AOM via the WindFreak device.

For environmental monitoring, the board is outfitted with both on-board and off-board 3-axis magnetometers (GY-271 modules). Onboard humidity and temperature sensors (DHT22), which measure temperatures in the range of -40°C to +125°C and 0 to 100% humidity readings. Three off-board temperature sensors (DS18B20), measuring within -55°C to +125°C. These sensors could be transported easily through the back panel grommet holes of the racks, where one was placed in the laser rack (can be seen bottom left of Figure 4.7). The Global Positioning System (GPS) was recorded

Channel Information	Physical Control
• 2x channels • 16-bit analog to digital converter • 0 to 10V	• 1x channel used for photodiode input for measurement of atom loading curves.
• 2x channels • 16-bit analog to digital converter • 0 to 10V	• 2x channels to be used for control of analog AOM driver (not implemented).
• 3x channels • 16-bit digital to analog converter • -10 to 10V	• These channels were for future magnetic field cancellation control.
• 4x channels • General purpose input output time-to-live (TTL) • 0/5V	• 2x channels to be used for controlling gMOT coils and dispensers (not implemented).
• 5x channels • General purpose input output TTL • 0/3.3V	• 1x channel used for camera trigger.

Table 4.2: Table overviewing the control hardware for the experiment

using a U-blox 7 module and the acceleration via an on-board accelerometer, GY-521 (MPU-6050).

A confocal optical system was employed to address the considerable scattering present in gMOT systems. The detected light was divided between a triggerable camera (CS165MU1/M) and a biased photodiode (PDA36A2) for imaging and monitoring of the cold atoms at the 2.5 cm diameter window of the gMOT. Consolidating the camera and photodiode signals into a single imaging system was adopted to minimise the sub-system's footprint.

Laser Driver and Car Battery -

These final two items occupied the remainder of the space on the rack. The MOGLabs DLC is 2U in volume and was chosen due to familiarity and ease of operation. The device drives the laser, frequency modulates the light via modulation of the current applied and has an in built lock-in amplifier for demodulating the signal and locking to the error signal. As will be discussed, more compact devices should be considered for

future iterations. Additionally, devices that do not require operation on AC voltages should be considered, allowing for the exclusion of the power inverter. Figure 4.5 showed there was still 3U of space available in the overall cold-atom system, therefore the laser driver did not necessarily pose as a hinder to the size of the system from the rack cabinet chosen in this project.

The battery used was a 12V, 110Ah car battery, 39.2D x 24W x 17.1H cm. Table 4.1 showed that the estimated power budget of the overall system was 115W, allowing for almost 10 hours of usage from the battery. An extra battery was purchased and placed in the system as a precaution but was not anticipated to be needed.

4.4.2 Results and Realisations

This chapter highlights the systems engineering required to transform a typically large and laboratory-based system into a portable one. Such a transformation involved identifying and addressing numerous challenges, leading to several key insights and realisations.

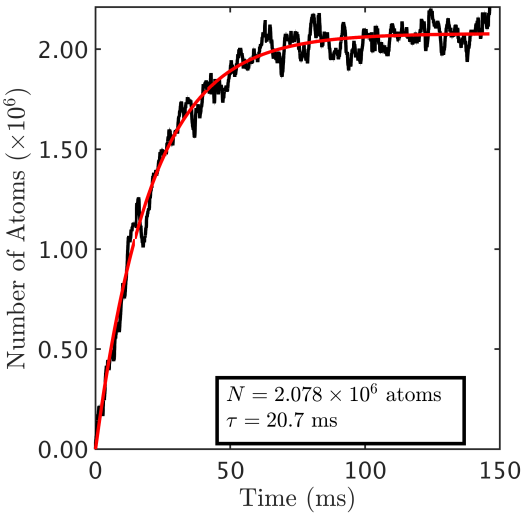

Figure 4.10: An example atom loading curve produced by the portable system in the lab before the field trials.

Figure 4.10 shows an example of a MOT loading curve, measured in the lab before the field trials. The MOT was turned off and on by configuring the AOM RF power.

The resulting atom loading curve is fitted using the following equation [90],

$$N(t) = N_{eq}(1 - exp(-t/\tau)) \tag{4.8}$$

where N equals the number of atoms in the MOT at time t, τ is the MOT loading time and N_{eq} is the equilibrium number of atoms in the MOT.

Figure 4.11: An image of the system in the back of a van on the day of the field trails. The system is powered by the car battery. The laser was found to on the day unlock consistently, resulting in only brief periods of cold atoms being achieved during the trials..

The number of atoms trapped and the MOT loading rates measured in the lab were consistent and the system was considered reliable. Figure 4.11 shows an example picture of the cold atom system in the back of a van on the day of the field trials. The system successfully powered up and cold atoms were achieved. However, the laser was

found to unlock consistently, staying locked for no more than about 30 seconds at a time. Described in this section are some of the realisations made both before and after deployment. Based on these findings, decisions have been made for the future iterations of this system in the hope for a more robust cold-atom system in version two.

Electronic Issues -

As a seemingly obvious route for powering AC devices in a portable manner, power inverters were chosen. Having trialled multiple different models and types of inverters in this project, however, it was concluded that these devices would not be elected as an effective solution again. Table 4.3 below summarises the devices tested, with the complications found with each highlighted. A total of four inverters were bought over the course of the project, of which, three of them were found to induce noise on the photo-amplified spectroscopy signal of the Flame. The noise was so apparent that it hindered the laser locking process with the error signal being drowned out by the noise. The inverters used varied in terms of wattage, price and both modified and pure sine wave devices were explored.

Table 4.3 shows the main issues found with the different inverters throughout the course of the project, with induced electronic noise being the biggest culprit and the hardest issue to mitigate. Inverter "1" was identified as the sole power inverter to not impede the laser locking process as it did not produce additional electronic noise. However, it was the only inverter of the four to cause a drop in the maximum current limit of the laser diode controller, meaning the laser frequency could not be tuned to resonance with the ^{87}Rb F=2 transition. This specifically happened when an extension lead was used and multiple devices were plugged in. Two pure-sine wave power inverters were purchased as it was theorised that modified sine inverters were not efficient or reliable enough for powering the AC devices. However, this change did not result in any improvement to the induced noise.

Inverter "1" was the only device to not induce noise to the system. It is assumed that the electronic noise issues are an effect of a grounding matter, of which "1" does not submit to. It was found that if only the DLC was powered by inverter number "1",

	Part Number	Power (W)	Pure Sine Wave vs Modified	Issue
1	Ultimate Speed USSW 300 A1	300	Modified	No noise induced. However, power of laser driver current dropped.
2	RS Pro 816-0034	500	Modified	Noise induced unless pressure to chassis - mechanical issue. No laser current drop.
3	Yinleader 500W Voltage Transformer	500	Pure Sine	Noise issues. No laser current drop.
4	RS Pro 179-3325	300	Pure Sine	Noise issues. No laser current drop, no mitigation of noise by pressure to chassis.

Table 4.3: The various power inverters purchased for the experiment and the challenges faced with each.

the current limit of the DLC minimising was resolved. Therefore, for demonstrations of the system powering outside of the laboratory, inverter "1" was used. This was the most acceptable solution due to time constraints, although it meant that additional components which require AC power (laptop chargers for example) had to be avoided as to not overload the inverter.

In improvements made to the current system or future builds, it is unlikely that power inverters will be utilised, an insight gained as a result of this work. Instead, portable DLCs which run off of DC voltages should be explored, with the additional advantage of reducing the real-estate of the overall system. An investigated solution which required basic resources and minimised alterations to the initial setup was explored by operating the MOGLabs DLC on DC power. This was achieved by supplying approximately 15V DC directly to the device, bypassing the transformer. This method was determined to effectively drive the laser with the exclusion of the power inverter

and is a route which will be considered in the next iteration of this project if minor modifications are desired.

Noise from the power inverters were not the only source of electronic difficulties. In general there were grounding issues relating to many of the components which form the portable system, with all of the racks needing to be grounded to the power-rack to mitigate some of the noise induced. Subsequently, it was discovered that as more electronic components were added to the system, for example the detection camera or a laptop, the problem persisted. The above issues were a consequence of the system being powered from the battery, which was a requisite for the system being portable. These various noise concerns were fairly unanticipated and a considerable amount of time was spent investigating in order to mitigate them. Unfortunately, on the deployment day this was the root cause of the system creating cold atoms for only short periods of time, as the locking electronics were disrupted with random bursts of noise.

Environmental Dependence -

Figure 4.12 shows trials of the cold-atom system in motion within the university building and outside of the laboratory. A steady-state MOT was realised, with the atom fluorescence recorded, as measured by the photodiode in the con-focal detection scheme. Simultaneously, the acceleration and magnetic fields were recorded by the environmental monitor to determine any correlation in the parameters to the MOT number. This experimental run lasted for 235 seconds before the laser became unlocked resulting in the MOT being lost.

Figure 4.12a displays that accelerations exceeding 0.6 g were recorded on the trial run, with a standard deviation of 0.1 g. Figure 4.12b presents the magnetic field measured during the same corridor run. The maximum field was 3.8 G, with a standard deviation 0.7 G. The atom number throughout the duration of the MOT steady-state varied with a standard deviation of 11% of the normalised value. The laser unlocking does not appear to correlate with either of the environmental factors, where the most significant changes in acceleration and magnetic field occur closer to the beginning or middle periods of the measurement. It is believed that the laser became unlocked due

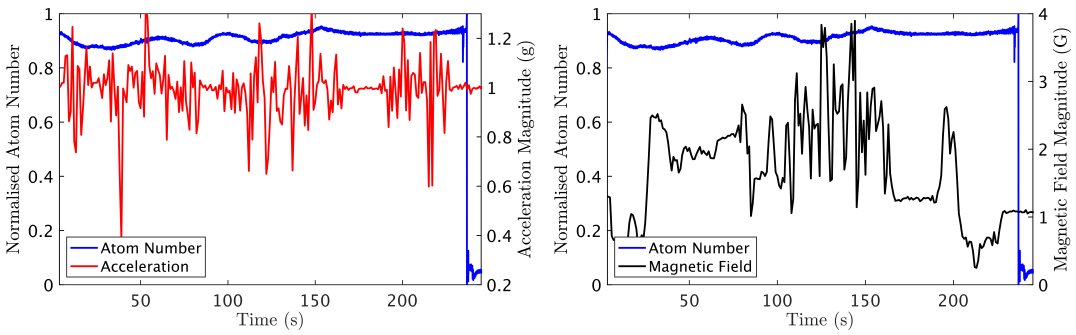

(a) (b)

Figure 4.12: A trial run of the portable system outside of the laboratory. A steady-state MOT was created and the system was transported in a corridor. The normalised atom number compared with the recorded: (a) accelerations (b) magnetic fields, are presented.

to the grounding issues mentioned before.

Overloading of Rb -

In an attempt to power the gMOT dispensers using the integrated device PCB, the dispensers were inadvertently overrun and the vacuum cell was overfilled with rubidium. We believe this caused the Rb partial pressure to saturate. Rubidium vapour pressure is fairly high, with a strong dependence on temperature (around an order of magnitude every 20°C). This occurred in the run up to the system being deployed and remained for several weeks.

The outside temperature had dropped to about zero degrees Celsius, which saw an advantageous opportunity for investigating this matter. The entire setup was transported outdoors for several hours to allow the vapour cell temperature to decrease. This was a profitable experiment, where there are limitations in lowering the temperature of a vapour cell from within a lab environment. Using cooling methods such as dry ice around the cell, for example, could result in the atomic vapour condensing. Being able to transfer the system with ease to a cold environment allowed us to safely attain a reduced rubidium pressure and increase the MOT loading time.

Trapped atoms are lost from the MOT due to collisions with hot, un-trapped rubid-

ium atoms and collisions with background gases. This permits for the pressure within the cell to be determined [17,91] by characterising the MOT loading curve, specifically by considering the loading time τ. This is particularly useful in cold atom experiments which do not contain pressure gauges, especially in compact sensors such as TMD's gMOT.

The loading time τ can be considered as the MOT lifetime, described in [17] as,

$$\tau = \frac{1}{\gamma P_{bk} + \beta P_{Rb}} \tag{4.9}$$

Here, P_{Rb} is the rubidium pressure and P_{bk} the background vapour pressure within the cell in mbar, explicitly everything else that is not Rb. The corresponding loss coefficients due to collisions with hot rubidium atoms and the background gases are described by β (3.3×10^7 mbar^{-1}s^{-1}) and γ (3.73×10^7 mbar^{-1}s^{-1}) [91], respectively. The pressure of the rubidium in the vacuum cell will increase drastically with temperature, using the following equation retrieved from [53],

$$log_{10}P_{Rb} = -94.04826 - \frac{1961.258}{T} - 0.03771687T + 42.57526log_{10}T \tag{4.10}$$

The pressure of the background gases can then be found by rearrangement of Equation 4.9.

The entire cold-atom system was sat stationary outside for several hours until a steady temperature was reached. The temperature of the cell was measured by placing a thermo-couple on the copper pipe of the ion pump. The system was then transported back inside and loading curves were recorded as the temperature of the system started to rise with room temperature.

Figure 4.13 shows a comparison of the loading curves for the apparatus at two different temperatures. Detailed also on each sub-figure is the equilibrium number of atoms in the trap and the calculated background pressure, by rearrangement of Equation 4.9.

The MOT loading time increased roughly by a factor of 7 after the system was cooled down. An unexpected outcome of this experiment was the factor of 10 increase

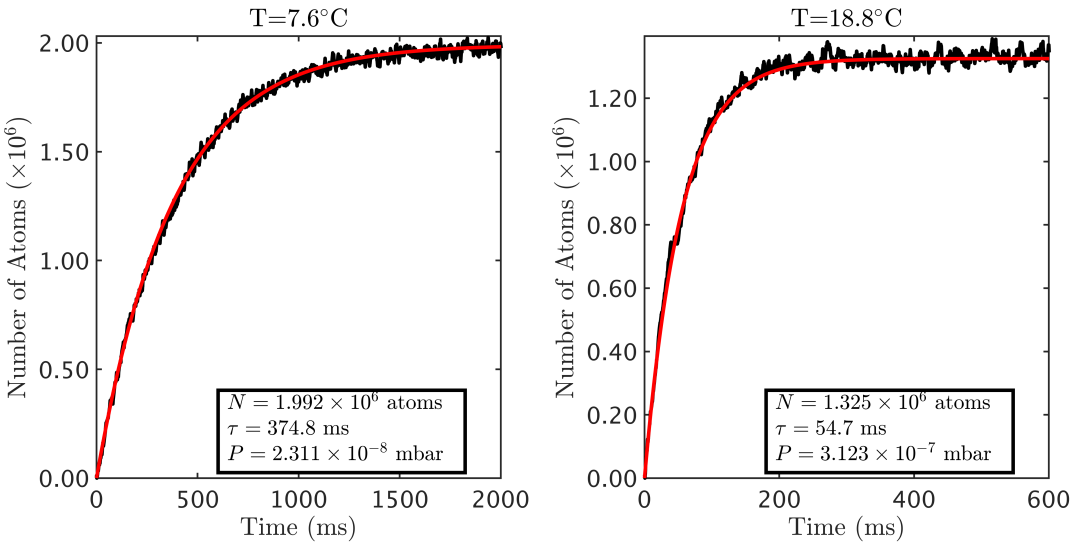

(a) (b)

Figure 4.13: Comparison of the loading curves with an ∼11°C difference in measured temperature. The loading curve has been fitted using equation 4.8. The atom number, loading times and calculated background pressures are labelled as N, τ and P, respectively.

in the background pressure as the temperature of the cell increased. This suggests that either the model used is incomplete, or there is a gas present in the vacuum which has a more significant temperature dependence with pressure than anticipated. The measured τ values were then compared to the theoretical values using Equation 4.9. A sensible value of 10^{-8} mbar was chosen for P_{bk}, with an adjustment in place to account for the ideal gas law. Figure 4.14 shows the experimental τ values as a function of the temperature of the cell, compared with the theoretical values.

An important aspect to consider is that although we successfully reduced the pressure within the vapour cell, uncontrolled parameters were prevalent. This was a best-effort attempt, with limited alternative solutions. Throughout this trial, the laser was kept on the entire time and was repeatedly locked. Similarly to the deployment in the van, the electronic issues caused by the portable-powering of the system resulted in continuous and random unlocking of the laser. The variability in the goodness of the lock during each re-lock may have contributed to the discrepancy between the experimental data and the theory. Additionally, the thermocouple was placed on the copper

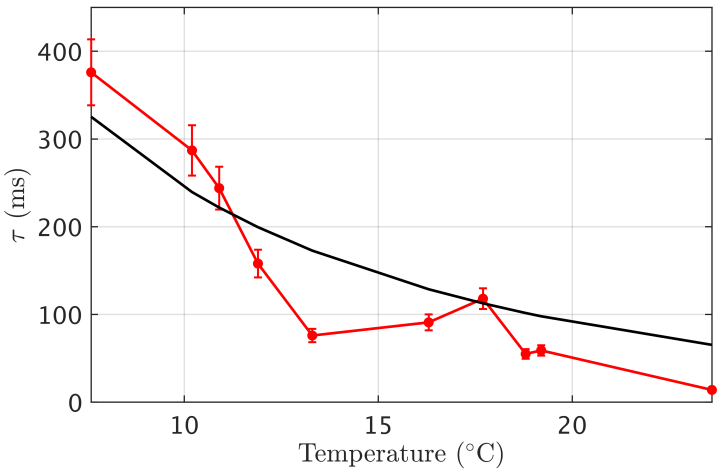

Figure 4.14: The experimental τ values against cell temperature plotted with the theoretical values of τ, using Equation 4.9. The included error bars are representative of the error calculated in loading curve measurements of a different setup.

pipe of the ion pump, where theoretical values are derived from the coldest point of the cell. For this reason, the temperature values have been offset by 5 degrees for Figures 4.13 and 4.14. The measurement ideally would be repeated and averaged to deduce the error in the results. This was challenging to do as the temperature was uncontrolled and rose quickly once the system was moved back indoors. The errors bars included in the plot are representative of the calculated standard deviation for loading curve measurements in a different experiment.

4.4.3 Conclusion

It is possible for the footprint of the system engineered in this chapter to be reduced massively. Alternative diode laser controllers could considerably decrease the system volume, with the added gain of improved functionality. Commercial DC-powered laser controllers such as Koheron drivers [92] could be integrated with a microcontroller to create a digital laser controller, for example. Strangfeld et al. [71] utilise a RedPitaya StemLab with a tailored extension board to both drive and frequency stabilise a DFB laser. Additionally, they have devised an accessible field-programmable gate array (FPGA) tool [93] which facilitates the automatic locking and re-locking of a user-

selected atomic transition. This would have undoubtedly improved the user friendliness and overall volume of the portable cold-atom source described here.

Additional downsizing of the system include minimising the laser sub-system through eliminating the EOM and AOM components. It is possible for the repump light, for example, to instead be generated from direct modulation of the laser diode [94]. Additionally, the double-pass AOM configuration resulted in about 50% of optical power being lost in alignment. There are alternative frequency stabilisation schemes which can allow for the frequency control needed whilst neglecting these devices. Schemes such as DAVLL (see Section 2.3.2) could be utilised, giving a large tuning range at the expense of a less stable lock. Methods which rely on the Zeeman effect for frequency shifting the atoms with a controlled magnetic field [16, 60] could also be employed. Portable atom interferometers in the literature achieve the frequency stabilisation and control needed in a variety of forms. Frequency offset locking is elected by many [9, 28, 67, 95], permitting for the exclusion of EOM and AOM devices, though requiring more than one laser source. This solution likely would have increased the optical power output of the trap beam if adopted in the system, though procuring additional lasers would be expensive with no real save on form-factor.

Table 4.4 overviews the system built in this project against other portable MOTs in the literature, as well as to two quantum sensors. Specifically, the size, weight and power of each is over-viewed. The system real-estate could have been substantially reduced by use of fibre coupled devices. It was discussed in Section 2.4 that Alter plan to fibre-couple future Flame modules. A frequency stabilised Flame device with a fibred output could be used in conjunction with fibred AOM and EOM devices for simplistic integration with the gMOT device. Portable atom interferometers and MOT devices are widely comprised of all-fibred components [9, 28, 67, 96–99], which are inherently less sensitive to vibrations and mechanical perturbations.

Portable magneto-optical traps are on the greater part comprised of the essential components which could eventually transform them into sensing devices. The limiting factor in doing so in the setup discussed in this chapter is largely due to the optical output power. Atom interferometry, as discussed in Section 2.3.3, requires 100s of

Citation	System Type	Size	Weight	Power	Additional Information
This work	MOT	60 cm x 60 cm x 90 cm	80 kg	111 W	Free-space optical components.
[98]	MOT	20 cm x 20 cm x 50 cm	10 kg	80 mW	Frequency-doubled telecoms system. All fibre components.
[97]	MOT	37 cm x 35 cm x 10 cm	6.5 kg	80 W	Frequency-doubled telecoms system. All fibre components. System was flown on a drone.
[95]	MOT	Laser system - (25 cm x 30 cm x 8 cm) Science Package - (7.2 cm x 42 cm)	5 kg	-	Powered by mains. Weight includes laser system only.
[100]	Bose-Einstein Condensate (BEC)	65 cm x 95 cm	246 kg	364 W	Weight includes two layer mu-metal shield. System is designed for achieving BECs - consists of two separate vacuum systems.
[101]	Lattice Clock	121 L	75 kg	320 W	System is designed to load strontium atoms into an optical lattice.

Table 4.4: A comparison of the cold-atom system described in this chapter compared to similar systems in the literature. This specifically focuses on the SWaP characteristics of each.

mW of light, specifically for experiments which rely on Raman laser pulses. Similar portable MOTs utilise fibred components with optical amplifiers [97, 98], which would enable the future adaption of their system for atom interferometry applications. Such a transformation is beyond the scope of this project, where the primary aim was to deploy a cold atom system in a vehicle.

This experiment predominantly served as a showcase for commercial quantum technology products, Alter's Flame laser module and CPI-TMD's compact vacuum system. As a first version, the developed cold-atom system is considered a success. Major electronic grounding issues when powering from the car battery impeded the van de-

ployment test. Time must be spent on identifying the fundamental cause, however, it is believed that reducing the number of components could tackle this. Additional work is also required to address the control hardware for improved user capabilities and organisation. With these refinements and future considerations of laser controllers used, a more reliable, robust and compact system is believed to be achieved with future builds.

As a closing statement, the Flame successfully endured the deployment test within the vehicle and additionally demonstrated resilience during prolonged exposure to almost freezing temperatures when operated outdoors for several hours. During both outdoor trials, it was observed that the frequency of the laser maintained resonance with the atoms, and there appeared to be no issue with the abrupt changes in temperature or environment.

Chapter 5

Magnetometry

Described in this chapter are two magnetometry experiments based on a free-induction decay configuration, employing alternate Flame devices as the laser source. Free induction decay (FID) magnetometry exploits the spin-polarisation of atoms as they are optically pumped by laser light. In the presence of a magnetic field, the atomic spins precess at the Larmor frequency as the pump is turned off, detected by monitoring the rotation of a weaker probe beam.

For these experiments, we rely on the atoms being polarised for as long as possible and therefore mechanisms such as collisions between the atoms with each other and the cell walls should be minimised. To prolong the spin-coherence lifetime of the atoms, therefore, a buffer gas can be added to the atomic vapour cell. The presence of the buffer gas in the cell effectively mitigates the decoherence of the atomic species by reducing cell wall collisions, prolonging the atomic coherence. However, a consequence of this inclusion is the occurrence of alkali atom collisions with the buffer gas molecules. Excessively high buffer gas pressures can lead to this being the primary depolarising contribution. Ideally, the alkali-wall collision rate and alkali-buffer gas collision rate are approximately equal. This minimises the intrinsic relaxation properties of the cell, as discussed in [102]. Additionally, the buffer gas leads to a broadening and frequency shifting of the optical resonances. The collisional broadening is directly proportional to the pressure of the added buffer gas, ∼20 MHz of broadening for each Torr with a -8 MHz/Torr frequency shift using nitrogen (N_2) buffer gas [103]. A suitable buffer

gas pressure should therefore be selected for magnetometry cells which incorporate buffer gas, accounting for the broadening whilst ensuring that the spin-coherence of the atoms is maximised. The magnetometers introduced in this chapter utilise micro-electro mechanical systems (MEMS) atomic vapour cells with added buffer gas. The main advantages of using MEMS cells are that they are mass-producible, inexpensive and compact enough for chip-scale devices.

The integrated vapour cell of the Flame is therefore redundant in magnetometry sensors which utilise MEMS cells with added N_2 buffer gas. The broadening and shifts caused by the buffer gas results in the incorporated vapour cell within the module being GHz detuned from resonance with the broadened MEMS cell atoms, for typical pressures of around 200 Torr or more. This broadening effect relaxes the stringent requirements on the lasers used in these experiments compared with the cold atom applications discussed previously, especially in terms of linewidth. For example, OPMs operating with buffer-gas cells could suffice with a laser linewidth less than 100 MHz [26]. Therefore, typically the lasers in this application do not require to be frequency stabilised, highlighting once more that the Flame's integrated vapour cell can be dispensable in magnetometry applications.

Laser diodes are the most commonly used laser devices in OPM experiments, especially for portable and compact sensors. Vertical-cavity surface-emitting lasers (VCSELs), for example, are extremely favourable due to their reduced dimensions and low-power consumption. The main advantages for using a Flame laser for such an experiment is twofold. The compact size of the module assists in the need for portable OPMs, aiding applications such as geophysical surveying, fundamental physics areas and medical applications [104–106]. The second is the Flame's high-optical power. The more intense the optical pumping light, the more atoms that are interacted with creating a higher spin polarisation and SNR. This is an advantage that lasers commonly used in portable experiments, such as VCSELs, cannot contend with. The high output power of the Flame may also be utilised to provide two or more independent beams paths, resulting in magnetic gradiometric measurements which are often desired in unshielded real-world magnetometry applications.

This chapter introduces two free-induction decay magnetometry sensors which use Flame modules, one based on rubidium atoms and the other using caesium. Both species are commonly used, each offering distinct benefits. Caesium for example has a higher vapour density at equivalent temperatures compared to rubidium. This is advantageous in terms of power consumption in a system where SWaP is a concern. Rubidium offers benefits such as a lower spin-destruction cross-section compared to caesium [103], leading to a lower rate of spin-destructive collisions and therefore a longer coherence time.

5.1 Free-Induction Decay Magnetometry

OPMs boast a wide array of benefits over other magnetic sensors such as flux-gates or Hall probes, with increased sensitivity performance and accuracy being the key qualities which surpass conventional devices. The choice of OPM configuration depends on the specific use case or intended application, with each configuration offering distinct traits and advantages. For example, the spin-exchange relaxation-free (SERF) configuration [107, 108] operates at low magnetic fields strengths of around 100 nT which sets a limit on the dynamic range. It does however achieve extremely high sensitivities, making it suitable for biomagnetism applications. Radio-frequency (RF) magnetometers have also displayed high sensitivities [109, 110]. This scheme also enables a tuneable detection frequency far from sources of technical noise, however, again the dynamic range of the sensor is limited providing a challenge for implementation in conditions where the magnetic field amplitude may vary (i.e. onboard moving vessels). A FID sensor is a straightforward technique to implement. Furthermore, it has the dynamic range required for operation in unshielded environments such as the Earth's geomagnetic field, paving the way for its use in portable sensing systems. An additional advantage is the device accuracy, as the high-intensity pump light is extinguished during the probing measurement stage, preventing excessive light shifts.

In general, OPMs operate by measuring the Larmor frequency, ω_L, of spin-polarised groundstate atoms as they precess around an external magnetic field, $|\overrightarrow{B}|$. The strength

of the magnetic field is calculated through the relation,

$$\omega_L = \gamma_g |\overrightarrow{B}| \tag{5.1}$$

where γ_g is the gyro-magnetic ratio of the atom, a fixed value given in Hz/T describing the ratio of an atom's magnetic moment to its angular momentum.

Measurements of ω_L in an FID sensor are performed by pulsed optical-pumping of an atomic sample with circularly polarised light which creates an atomic orientation. By separately probing the atoms with a weaker, linearly polarised beam, the precession of the atoms around $|\overrightarrow{B}|$ is detected by the resulting optical rotation of the probe light. The optical rotation is detected using a balanced polarimeter device connected to a data acquisition (DAQ) device. This signal takes the form of a decaying sinusoid,

$$S(t) = Asin(\omega_L t + \phi)e^{-\gamma t} \tag{5.2}$$

where A is the amplitude of the signal, ω_L is the Larmor frequency, ϕ is the phase and γ is the decay rate.

The more atoms included in the spin-polarisation build up, the higher A and therefore the higher the SNR. This is achieved experimentally by interacting with as many atoms as possible, augmented by increased atomic vapour densities, longer cell path lengths, and a more intense pump beam. The decay rate γ of the signal is inversely related to the coherence lifetime of the atoms. Prolonging the spin-coherence of the atoms will therefore increase the measurement time and the overall sensitivity of the sensor. The atomic cells in this chapter therefore include nitrogen buffer gas in order to minimise decoherence processes such as atomic wall collisions.

A key metric for an OPM sensor is the sensitivity. A magnetometer's sensitivity describes the smallest magnetic field change that is able to be resolved by the sensor. The sensitivity of an OPM is estimated by performing a discrete Fourier transform (DFT) on the time domain data for recorded magnetic fields. This conveys the data in the frequency domain and the noise floor of the sensor is found. FID sensors have demonstrated sensitivities in the 10s of $fT/\sqrt{Hz}$ levels in unshielded environments [106]

and 100s of fT level using novel spin-polarising techniques [111].

5.2 Experiment - FID With Natural Rubidium

The most commonly used atomic magnetometers consist of caesium atoms or an isotope of rubidium. In this section, we introduce an FID experimental setup consisting of a cell of natural rubidium atoms.

Having two isotopes present results in two distinctive precession frequencies. Therefore, the model equation (Equation 5.2) to describe this process for a cell containing natural rubidium atoms becomes,

$$S(t) = Asin(\omega_{L1}t + \phi_1)e^{-\gamma_1 t} + Bsin(\omega_{L2}t + \phi_2)e^{-\gamma_2 t} \tag{5.3}$$

where the parameter definitions are the same as previously discussed, except now describing the precession for each isotope. The gyro-magnetic ratios for ^{85}Rb and ^{87}Rb atoms are 4.67 Hz/nT [54] and 7 Hz/nT [53], respectively. In the presence of an external magnetic field, the ^{87}Rb atoms will precess around the field with a Larmor frequency 1.4989 times faster than the ^{85}Rb atoms. The objective of this experiment was to demonstrate this variation in the Larmor precession frequency. For the experimental results to follow, we define the first half of the equation as ^{85}Rb's contribution and the second half as ^{87}Rb's.

Figure 5.1 depicts an example of the individual FID signals for each isotope when influenced by the same magnetic field (top), compared with the sum of their contributions (bottom) in accordance with Equation 5.3. It has been assumed that ^{85}Rb's precession signal is larger in amplitude than ^{87}Rb's due to its higher natural abundance. The resultant signal does not represent a single exponentially decaying sinusoid, unlike single atomic species or isotopes.

Figure 5.2 shows the spectrum for the MEMS cell used in this experiment against a 75 mm glass-blown vapour cell. The MEMS cell here is 3 mm thick and contains around 200 Torr of N_2 buffer gas. The 200 Torr of buffer gas results in 4 GHz of broadening of the optical transitions due to collisional broadening and the hyperfine

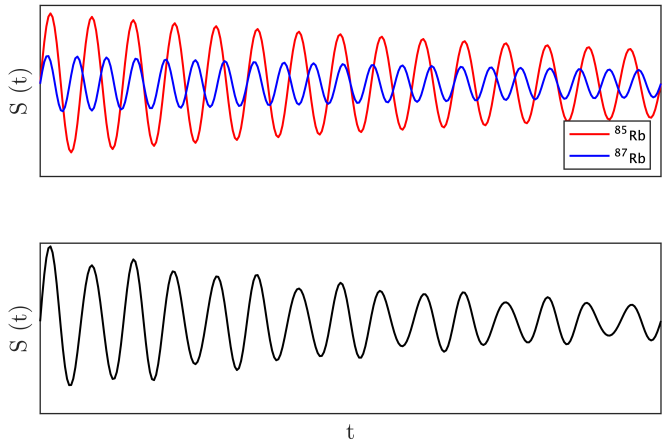

Figure 5.1: Simulated data displaying the individual FID signals for each isotope in the presence of the same external magnetic field (top), compared with the resulting, combined FID signal which will be detected (bottom). The ^{87}Rb atoms precess approximately 1.5 times faster than ^{85}Rb. The lower natural abundance of ^{87}Rb results in a lower number of atoms which are interacted with. This lower signal amplitude has been accounted for in this simulated data.

levels of ^{85}Rb and ^{87}Rb are therefore unresolvable. This means that the pump laser will be simultaneously polarising both isotopes of rubidium as it is scanned across the cell.

5.2.1 Experimental Setup

The experimental setup was as shown in Figure 5.3. A single 780 nm (Rb D2) Flame laser was used, which performs both the optical pumping and probing. Optical pumping in OPM systems is more commonly employed on the D1 transition line, due to the higher achieveable total spin polarisation [103]. However, recent results utilising D2 line optical pumping for Rb and Cs have also demonstrated excellent sensitivity performance [111, 112].

An AOM is used to modulate the laser's amplitude. This offers a simpler solution compared to the direct modulation of the Flame, while also allowing precise control over the signal's high and low levels. A square wave is applied to the AOM via a function generator, raised to a high level during the pump stage before being lowered to a much

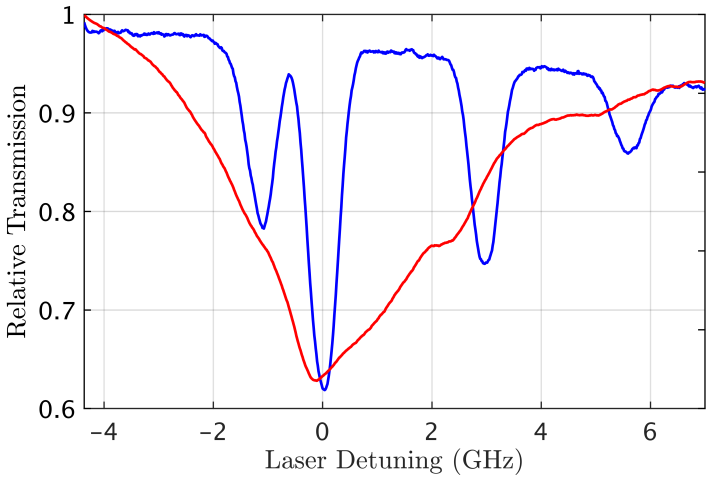

Figure 5.2: Example spectra of the MEMS cell (red) used in this experiment compared with a 75 mm reference cell (blue) of natural rubidium. The transitions of the reference cell from left to right show ^{87}Rb F=2→F', ^{85}Rb F=3→F', ^{85}Rb F=2→F' and ^{87}Rb F=1→F'. The MEMS cell is displayed as a single peak with the hyperfine levels unresolved due to the 200 Torr of buffer gas.

lower intensity for the probing stage. To achieve FID in the single laser scheme, the light should be elliptically polarised. Elliptically polarised light is used to compensate for the ideal case of having circularly polarised pump light for optically pumping the atoms and linearly polarised probe light for detection. A QWP is placed before the cell to achieve this ellipticity, with a HWP after the cell to ensure equal light is directed to each detection arm of the polarimeter when separated at a PBS. Separating the probe light into two separate channels enables differential polarimetry to be used. The two individual light ports are π out of phase with each other, enabling the differential to be taken which enhances the SNR.

The atomic sample is a 3 mm thick MEMS cell of natural rubidium, heated to 75°C to increase the atomic density. An external magnetic field of about 25 μT was produced by a pair of Helmholtz coils, applied in the transverse direction to the beam-propagation cancelling the Earth's magnetic field. Ideally, the external field applied in a lab setting would emulate the the Earth's field ($\sim$50 μT) if characterising a portable sensor for geomagnetic sensing. For this experiment, the coils available produced a maximum field of around 25 μT which was sufficient for this demonstration.

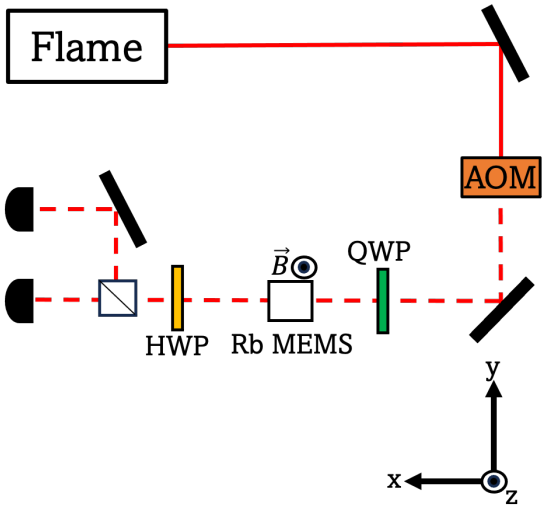

Figure 5.3: Schematic of the setup for achieving FID. The Flame laser light is amplitude modulated at the AOM via a square wave. The modulated signal, depicted here as a dashed line, acts as the pump laser on high-level and the probe on low. Elliptically polarised light is realised at the QWP. A magnetic field is applied at the Rb MEMS cell transverse (z-direction) to the beam propagation axis (x-direction). A HWP is used to balance the power in each detection arm where the detected signals are subtracted from one another for the optical rotation of the probe light to be measured

5.2.2 Experimental Results

Figure 5.4 shows an example signal of the FID sensor based on natural rubidium, with an experimental fit applied using Equation 5.3. By fitting to the experimental data, the various parameters of the FID signal can be extracted. Table 5.1 shows the parameter results for Figure 5.4.

Table 5.1 shows that the values of ω_{L1} and ω_{L2} can be extracted with high accuracy using the fit to values which match that of the theory. These parameters will however depend on the laser frequency, and it was of interest to examine the variation at different laser detunings. An FID trace was captured at various laser frequencies, as recorded by a wave-meter, to observe the effect on these parameters.

Figure 5.5 shows four example FID traces as the laser frequency is scanned across the resonance profile of the MEMS cell. The laser frequency detuning is relative to ^{85}Rb F=3→F', as shown in Figure 5.2. The laser detuning was varied by approximately 10 GHz in total. Equation 5.3 was applied to each trace to extract the experimental

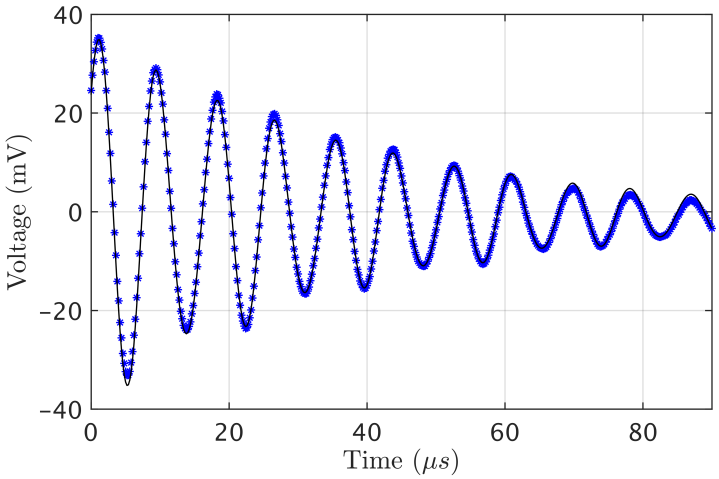

Figure 5.4: An example FID trace of the sensor, with a fit applied. The various parameters obtained from the model are revealed in Table 5.1.

parameters. It is observed that as the laser frequency is increased, the FID signals begin to resemble less of a decaying sinusoid, and more of the superimposed signal. In Figure 5.6, we compare the extracted Larmor ratios of ^{87}Rb to ^{85}Rb ($\omega_{L2} : \omega_{L1}$) as the laser frequency is altered.

Figure 5.6a shows the extracted Larmor frequency ratios as a function of laser frequency detuning. The green dashed line indicates the theoretical Larmor ratio value of the two isotopes (1.4989). The black dashed lines show plus and minus 0.5% of the theoretical value. Also plotted is the absorption profile of the MEMS cell as the laser frequency is scanned.

It is evident that the first 3 data points give inaccurate values of this ratio, this is specifically due to the extraction of ω_{L2}. It is assumed at this stage that the laser is predominately interacting with the ^{85}Rb atoms alone, or with a very limited number of ^{87}Rb atoms. The standard decaying sinusoidal fit is most appropriate at this stage with Equation 5.3 ineffective. Once the laser is scanned to the other side of the MEMS absorption profile towards ^{87}Rb F=1→F', more of the ^{87}Rb atoms are involved in the optical pumping process. The fit then gives accurate values of the precession ratios of the two isotopes to within 0.5% of the theoretical value, as observed in Figure 5.6b. The natural abundance of the isotopes will contribute to the optimal laser pumping

	^{85}Rb	^{87}Rb	Ratio of ^{87}Rb to ^{85}Rb
Amplitudes Extracted	66.1 mV	4.9 mV	0.07
Larmor Frequencies	$2\pi\times$116.5 kHz	$2\pi\times$174.6 kHz	1.498
Phase	130°	236°	$\phi_2 - \phi_1$=106°
Decay Rate	24.7 kHz	24.3 kHz	0.98
Calculated Magnetic Fields	24.95 μT	24.94 μT	0.9995

Table 5.1: The experimental results of Figure 5.4. The ratio of the Larmor frequencies ($\omega_{L2} : \omega_{L1}$) match that of the theory for this particular FID trace.

frequencies for extracting accurate ratios, with ^{85}Rb 72% in abundance compared to ^{87}Rb at 28%. As the laser frequency is increased closer to resonance with ^{87}Rb F=1→F', there remains a considerable interaction with ^{85}Rb atoms due to their higher natural abundance.

To expand on this further, the decay rates and amplitudes for each isotope as a function of laser frequency were explored. The decay rates and amplitudes of the ^{87}Rb atoms are only displayed from about +1 GHz of detuning onwards due to the poor fit for this isotope for the preceding frequencies. By applying a single sinusoidal fit (Equation 5.2) to the files where ω_{L2} was unsuccessfully extracted, it was observed that the extracted parameters for ^{85}Rb gave the same values as those using Equation 5.3. The values for ^{85}Rb have therefore been plotted for all measured laser frequencies.

Figure 5.7a shows a decrease in the relaxation rate for each isotope as the laser is tuned further from the trough of the MEMS cells optical resonance. Employing the laser at this frequency therefore extends the atomic spin coherence time. The probe beam reaches maximum absorption at around 0 detuning, power broadening the isotopes during detection. This perturbs the atoms and induces them to decay much faster, a consequence of using one laser source for both pumping and probing.

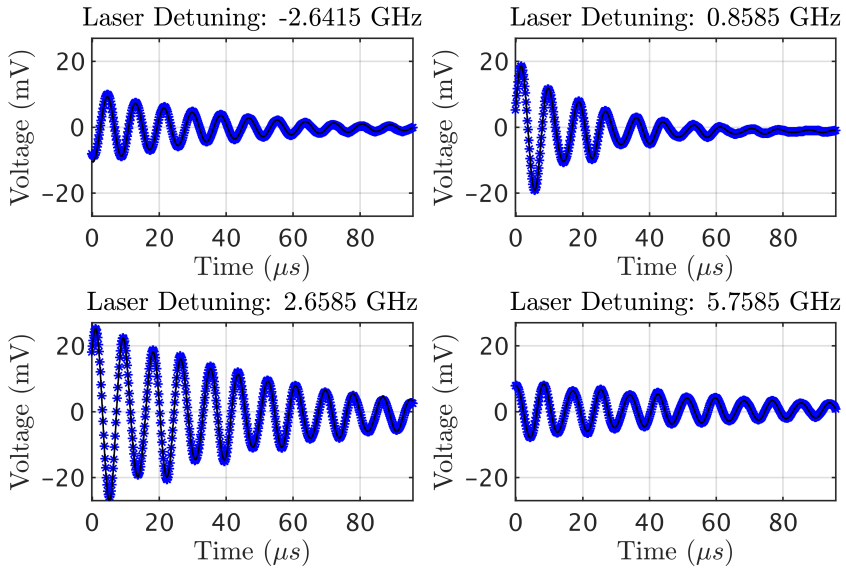

Figure 5.5: Four example FID traces as the laser frequency is scanned. Each trace includes a fit using Equation 5.3. The FID trace develops into a signal which resembles less of a decaying sinusoid as the laser frequency is blue detuned from ^{85}Rb F=3→F'

Typical FID sensors which employ separate pumping and probing purposefully detune the probe far from resonance so as to avoid this detrimental residual optical pumping effect (occurring at ∼1 GHz on this scale).

The sensor's optimal laser frequency is one which maximises the signal amplitude and minimises the decay rate. Figure 5.7b shows the extracted amplitudes for each isotope. The highest number of atoms were spin-polarised for each isotope at maximum absorption. It was initially expected that the ratio between the extracted amplitudes would reveal the abundance ratio of the isotopes at this laser frequency, with amplitude A being roughly 2.5 times B. This was never realised, and the amplitude of A is at minimum around 6 times greater than B. This allows us to conclude that there are far more ^{85}Rb atoms involved in the optical pumping process at any given laser frequency in this demonstration.

Figure 5.8 shows the extracted phase from the model for each isotope and the phase difference. Referring to 5.8a, we see an approximate π phase shift in ϕ_1 indicating a change in the optical rotation direction of the isotope. This occurs as we begin to

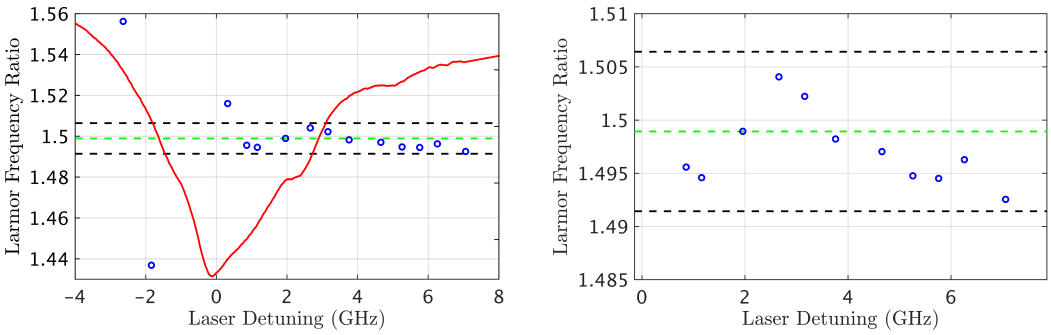

(a) (b)

Figure 5.6: The laser detuning as a function of Larmor frequency ratios ($\omega_{L2} : \omega_{L1}$). Both plots display the theoretical ratio (green dashed) and plus and minus 0.5% of this value (black dashed). (a) Shows the detuning with the MEMS cell absorption profile (red), included for clarity on where the optical pumping is occurring. (b) Zoomed in image of the high-accuracy values which fall within 0.5% of the theory.

pump the atoms from ^{85}Rb F=3→F' to F=2→F', as the laser frequency is increased. These two transitions have opposing Landé g_F factors, causing a change in the atomic precession direction as the F=2 level is introduced to optical pumping. Furthermore, this process contributes to the missing data from detunings around -1.9 GHz to 0.3 GHz. At this stage, no FID signal was observed as the two ground levels of ^{85}Rb are simultaneously pumped, causing decoherence through spin-exchange collisions due to the opposite directions of precession.

Figure 5.8b shows the phase difference between the two isotopes with varying laser frequency. This difference is not random with laser detuning, however, the trend is not completely understood. The optical pumping dynamics in this demonstration are complex due to the single beam configuration combined with two-isotopes, consisting of a total of four ground states. Fully understanding the results of the sensor would require further investigation, with decoupling the pump and probe beams considered a key start. This would enable the separate beams to be polarised circularly and linearly for the respective pump and probe, rather than the elliptical light used in this demonstration. Additionally, it would permit the probe to be detuned further from resonance for both isotopes ensuring the probe does not majorly influence the atoms through power broadening and light shift mechanisms.

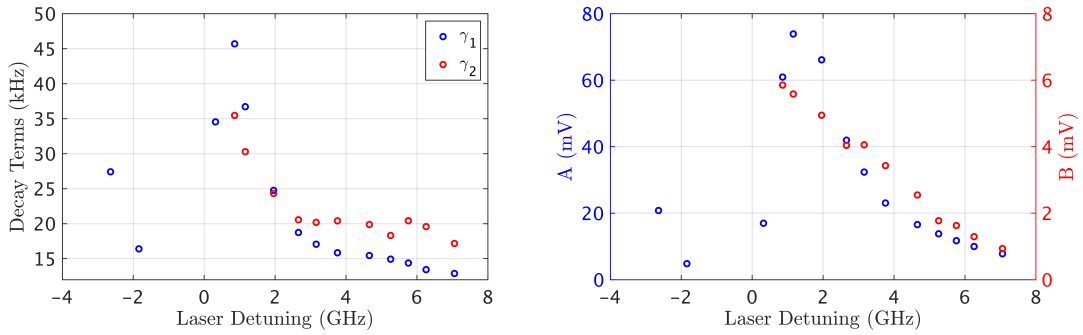

(a) (b)

Figure 5.7: (a) The decay rates for each isotope as a function of laser frequency and (b) the extracted amplitude for each isotope.

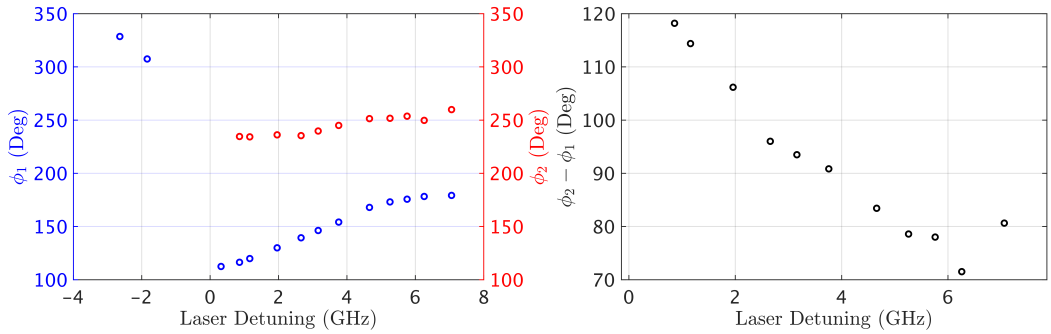

(a) (b)

Figure 5.8: Laser frequency detuning and the influence on (a) ϕ_1 and ϕ_2 values and (b) the difference in ϕ_1 and ϕ_2.

5.2.3 Conclusion

The work shown here is a compelling start to what is known as a co-magnetometer. A co-magnetometer is a sensor capable of simultaneously measuring the spin-precessions of multiple atomic species from within the same cell volume. The motivation towards such a sensor pertains to its feasibility for inertial rotation sensing. Co-magnetometers are commonly executed using alkali noble-gas cell mixtures [11, 113], dual alkali combinations [114] or atomic samples comprised of a single species [115–118]. Typically, co-magnetometers operating in environments with magnetic field gradients suffer from errors due to the difference in thermal diffusion between species. This can cause the measured magnetic fields to be marginally different due to the gradient affecting their

average position in the cell volume. Single species co-magnetometers are therefore advantageous in reducing the systematic errors that are associated with using two or more species [118].

No effort was put into this demonstration to reduce the size of the experimental setup, nor was the experiment tested in a magnetically shielded environment. The magnetically unshielded laboratory resulted in high-relaxation rates due to large magnetic gradients. A shielded system would greatly improve this, as magnetic gradients would be greatly reduced, resulting on improved coherence times and therefore measurement times. Continuation of this experiment could include miniaturisation for portable use, as well as separating the pump and probe lasers as discussed. There is ongoing research within the EQOP group at Strathclyde towards the active tuning of buffer gas pressures in MEMS cells [119]. This technique could be beneficial in this demonstration to reduce the cell pressure which would permit the transitions to be distinguished, providing clarity on which transitions and isotopes are being optically pumped at a given laser detuning. Subsequently, the laser scan tests performed in this section could be repeated at varying buffer gas pressures to identify the optimal cell pressure for the co-magnetometer sensor. Finally, the advantage of the abundant optical power deliverable from the Flame device would be well suitable for multiple OPM sensing channels. This could be achieved, for example, by introducing fibre-splitters redistributing the optical power to various MEMS cells and detection schemes.

Although this experiment has demonstrated its potential relevance in co-magnetometry applications, far more straightforward FID systems can be developed. Considering more than one isotope complicated the analysis of the magnetometer signal due to the atoms precessing at different frequencies. Additionally, using only one laser source is not optimal for ensuring that the probe light does not interfere or disturb the polarised spins in the detection stage. In the following section, we introduce a caesium based FID sensor with separate pump and probe laser sources, improving on these drawbacks.

5.3 Experiment - FID With Caesium

Aligned with previously discussed points, such as the need for portability and bringing quantum technologies out of the lab, an 852 nm Flame was used to demonstrate a compact and accurate free-induction decay magnetometer. The general idea was to integrate a Flame laser into existing University of Strathclyde (UoS) quantum technology [120] and compare the performance to other magnetometers which operate in different configurations. Additionally, the system was to be compact enough to be packed up with ease for outdoor and unshielded measurements of the Earth's field.

This section therefore links in suitably with Chapter 4, with the overall goal to demonstrate a quantum sensor for portable and outdoor use, albeit an alternative application. Both chapters therefore demonstrate the Flame module's adaptability within the realm of quantum technologies. In addition, this section presents an improved FID setup from that presented in Section 5.2, where certain issues were highlighted. Caesium is frequently used as the atomic ensemble in magnetometry experiments, particularly in magnetometers that utilise MEMS vapour cells containing N_2. As seen in the previous section, the inclusion of the buffer gas can cause the two isotopes and the total of four ground state transitions of natural Rb's D2 line to overlap, complicating the signal analysis. This section by contrast considers only one isotope, allowing for alternative data extraction methods not permitted in Section 5.2. Separate pump and probe lasers are also employed to prolong the spin-coherence of the atoms, with measurements being performed in a magnetically shielded environment.

5.3.1 Experimental Setup

The experimental setup is illustrated in Figure 5.9. The laser sources used are an 852 nm Flame and an 895 nm VCSEL for the pump and probe beams, respectively. The Flame laser light is amplitude modulated by the AOM and fibre launched ready for integration to the overall magnetometer sensor head. The sensor head consists of a fibre input for the Flame light and a VCSEL for the probing laser. Both beams are directed to and overlapped at a 200 Torr caesium MEMS cell, glued to a dielectric mirror, which

is sandwiched between the vapour cell and a PCB heater. Perfect overlapping of the beams at the cell is essential for achieving an optimal FID signal. The probe laser strikes the centre of the mirror before being reflected and directed towards a PBS for balanced photo-detection. Whilst it is not intended that the pump beam also reflects towards the detection scheme, it is not a significant concern if it does as it is turned off during the probing stage. The design of the sensor consists of only a few components to provide scope for scalability and portability. This is in contrast to a typical laboratory based sensor which tend to employ a plethora of components for optimal performance.

Figure 5.9 shows the optical breadboard layout for the Flame, which is fibre launched to the overall sensor head. The breadboard is 24 cm by 19 cm. Thorlabs miniseries range is used (see Chapter 4) for the optical components to keep the overall size of the setup to a minimum. Additionally, two optical isolators at 30 dB isolation were included, essential components to reduce optical feedback issues (see Chapter 2). Contrary to Chapter 4, Thorlabs IO-3D-780-VLP optical isolators were chosen. These are more easily accessible and cost-effective. The aperture size is smaller than the EOT optical isolators used previously, though this was not found to be an issue here. The 852 nm Flame module produces 185 mW of light at its output. The light follows the path depicted in Figure 5.9, before being amplitude modulated at the AOM and re-collimated with a 1.5x magnification telescope. The beam is then directed to a fibre collimator for launch to the sensor head. The diffraction efficiency achieved was 83% and the fibre coupling efficiency was 62% allowing for a maximum optical power of 65 mW at the end of the fibre to the sensor head input.

The sensor head is a 3D-printed design, made of high-temperature resin. This design was based on a previous version used in a double-resonance configuration, designed by Strathclyde's Stuart Ingleby. Previous versions of the sensor-head utilised two separate VCSELs for the pumping and probing beams. These components are compact and are easily glued into the sensor-head package, using a push-fit insert. Using the Flame as the pump laser offers a significant advantage over the VCSEL by substantially increasing optical power and therefore optical pumping. Since the Flame's free-space light is instead fibre launched to the magnetometer sensor head, the main alterations made

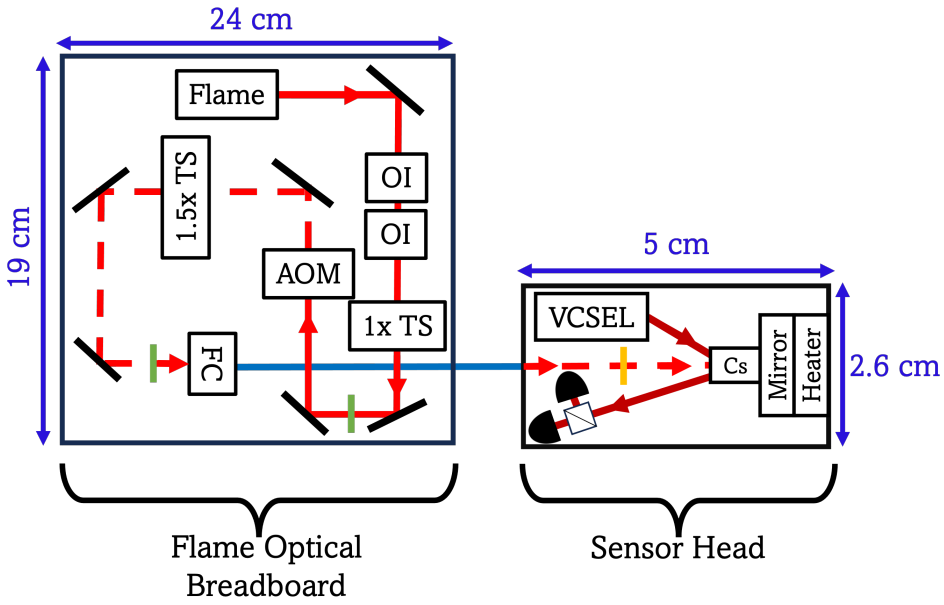

Figure 5.9: An 852 nm Flame laser is amplitude modulated at an AOM and fibre launched to the overall magnetometer sensor-head. Green blocks are HWPs. (OI: optical isolator, TS: telescope, FC: fibre-coupler). The sensor is comprised of the Flame fibre input, a VCSEL to probe, a QWP (yellow block), a 200 Torr Cs MEMS cell and a detection scheme. Image not to scale.

to the design were therefore the optical fibre's insert. The yellow block on the image demonstrates a quarter wave-plate. This component is 5 mm in diameter, with the fast-axis indicated by a flat edge as provided by the supplier. This permits the QWP to be glued into the sensor-head with the fast-axis aligned orthogonally to the direction of propagation of the pump beam. Orientation of the fibre-insert by 45° with respect to the fast-axis of the QWP then attains circular polarisation of the pump light.

The caesium cell is 3 mm thick containing around 200 Torr of nitrogen buffer gas. The cell is heated to around 70 °C through resistive heating of a PCB coil. The cell heater is periodically driven by a square wave with an 'on' state when pumping and 'off' when probing. This prevents any additional magnetic fields being present during detection.

5.3.2 In-house Fibre Collimators

A requisite for the fibre connector is that it must be non-magnetic considering the proximity of the fibre input to the atomic vapour. This aspect made this a partially challenging demand for this version of the sensor, and a custom adaption was necessary. Non-magnetic fibre connectors do exist commercially, such as used those used in [121]. However, this component proved to be both too expensive and bulky for this demonstration. Custom and compact fibre collimators were instead fabricated in-house using readily available Thorlabs components.

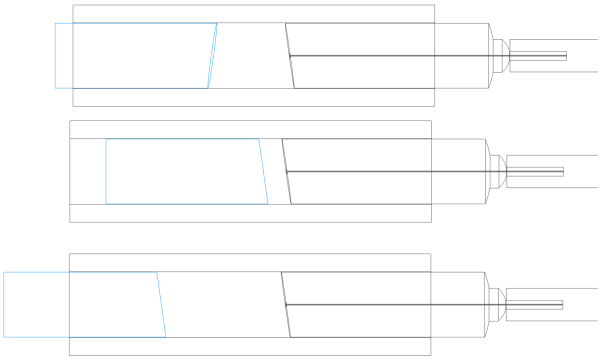

Figure 5.10: Inventor screenshots of the in-house fibre collimator. From left to right, it displays the GRIN lens (blue) and the pig-tailed fibre end, both placed inside of the glass mating sleeve. The GRIN lens in each example is varied in distance from the fibre and in angle with respect to the 8° fibre end-face.

Thorlabs provide all glass components for fabricating custom fibre-collimators internally. The collimators are composed of pigtailed glass ferrules (with a standard connector located at the opposite fibre-end), aligned with a gradient-index (GRIN) lens both glued within a glass mating sleeve. The components used for the portable FID sensor were part numbers PMPFX5, GRIN2308A and 51-2800-1800 for the fibre, GRIN lens and ferrule sleeve, respectively. The fibre itself is a polarisation maintaining, angled physical contact pigtailed ferrule. The glass ferrule of the fibre is therefore angled at 8° to minimise back reflections, the GRIN lens end-face is also angled for the same purpose. This makes the alignment of the components slightly more challenging to implement, as both the distance between the fibre-end and the lens must

be controlled as well as the rotation to allow the angles to match when fabricating the collimator.

Figure 5.10 shows an example of the components on Inventor with the GRIN lens at differing distances and angles. The glass sleeve is 10 mm long with the fibre and the lens 5.6 mm and 4.4 mm long, respectively. The optimal distance between the fibre ferrule and the GRIN lens for a collimated beam is 0.27 mm. However, to ensure a definite overlap of the pump beam with the probe, this version of the fibre-collimator prioritised a large beam (∼3 mm diameter) at the distance matching where the fibre sits to where the cell is situated in the sensor. This was to guarantee that as many atoms as possible were optically pumped without assurance at this stage that the pump and probe beams were aligned to the same location at the cell. Future versions should focus on collimating the fibre output, increasing the beam intensity and involving more atoms in the spin build up. This would demand perfect overlapping with the probe laser which may require multiple sensor-head prints, and driving the VCSEL before gluing to each print. The project time limitations at this stage did not permit for these trials.

After the preferred beam-diameter was chosen and the rotation of the GRIN lens angled end-face was aligned with the fibre ferrule, the components were UV cured using optical adhesive. The subsequent stage involved securing the fibre collimator to the OPM sensor head. This was initially intended to be screwed-in at the fibre aperture for easy insertion and removal, but more crucially for control of the polarisation alignment. The fast-axis of the QWP is fixed in place in the sensor as discussed. The polarisation of the light at the vapour cell is thereby controlled by the orientation of the fibre-insert, preferably 45° to the QWP fast-axis for perfectly circular light. However, securing the fibre-insert using nylon screws led to slight misalignments of the pump through the MEMS cell. Ultimately, for this version of the sensor the fibre-collimator was aligned manually and glued in place using 5-minute epoxy adhesive. The position was optimised by observing an FID signal whilst rotating the collimator, with the highest signal amplitude indicating that the pump laser was mostly circular at that orientation. This solution poses a high risk, particularly if the fibre is damaged. Future versions of the

sensor should consider more careful design of the fibre aperture position. Additionally, a design for a rotating mount for the QWP could be a more elegant approach for control of the pump light polarisation.

5.3.3 Synchronous Modulation

The optical pumping efficiency can be greatly boosted by driving the atoms at the Larmor frequency during the pumping stage [122]. This method becomes more effective at higher fields, such as the Earth's at 50 μT. Since the magnetic field is transverse to the beam propagation direction, atoms become deflected from the beam propagation axis to a greater extent for increasing field strength. This limits the achievable spin-polarisation and expedites the decoherence at higher fields due to the exerted torque. Actively pumping the atoms at the Larmor frequency therefore increases their spin-coherence. This method, known as synchronous modulation, was employed in this experiment. This approach however does require prior knowledge of the field being measured. In a laboratory based setup, this poses no issues, as the sensor can easily be employed to initially measure a known applied field.

To employ synchronous modulation, programming of the function generator driving the pump is necessary. This is to execute the arbitrary waveform needed, which is frequency mixed with an RF input (WindFreak SynthHD) to drive the AOM.

It should be noted that this approach could not be used in Section 5.2 due to the two rubidium isotopes precessing at different Larmor frequencies. This underscores the improved design of this sensor in terms of implementation, and as will be seen, in detection and analysis.

5.3.4 Data Extraction Methods

Section 5.2 demonstrated the signal analysis required to extract the experimental parameters of the FID signal. This was achieved by fitting a damped sinusoid to the signal, using either Equation 5.3 for the co-magnetometer, or Equation 5.2 where only one isotope is considered. This is constructive for analysis within a laboratory environment as it gives an accurate and thorough extraction of the key information concealed

in the signal. In a portable environment however, performing this post process is not ideal. Instead, an instant and continuous method for determining the magnetic fields is sought. In this demonstration, we elected to use a frequency counter for the recording of the Larmor frequencies to provide a direct reading in an unshielded environment. This method does not capture the full parameters of the signal, and only provides the oscillation frequency information, as the active tracking of the magnetic field was prioritised.

The setup for recording the Larmor frequencies for the portable FID-sensor is shown in Figure 5.11. A digital delay instrument is included (DG535). A square-wave from the function generator (Keysight TGF4042) is used to heat the cell using a pulsed approach, active only in the pumping stage as mentioned in Section 5.3.1. This is the trigger input to the delay generator, with a time delay with respect to the trigger being manually altered by the user. This gives an appropriate output signal, sent to the external gating input of the frequency counter (Keysight 53220A). The gating period of the frequency counter can then be set to trigger during the probing stage only. Note that triggering the gating period to the falling edge of the square wave resulted in the frequency counter beginning the measurement whilst the pump was briefly still on. Implementation of the delay generator was therefore essential to delay the trigger by a few μs before the measurement begins.

Figure 5.11 shows the simulated signals essential for driving the sensor and recording the measured magnetic fields. The atoms are pumped synchronously during the pumping period and then probed (blue). The cell heater is driven by a square wave (red) with a repetition rate matching that of the synchronous signal, 1 kHz in this example. The black signal is the gating period for the frequency counter, where the delay and width of this signal are controlled by the delay generator. Fine tuning the width of the delay pulse is necessary to ensure that no pump light leaks into the frequency counter measurement. By implementing this method, the recorded Larmor frequencies can be used to assess the performance of the magnetometer synonymous to the fitting regime.

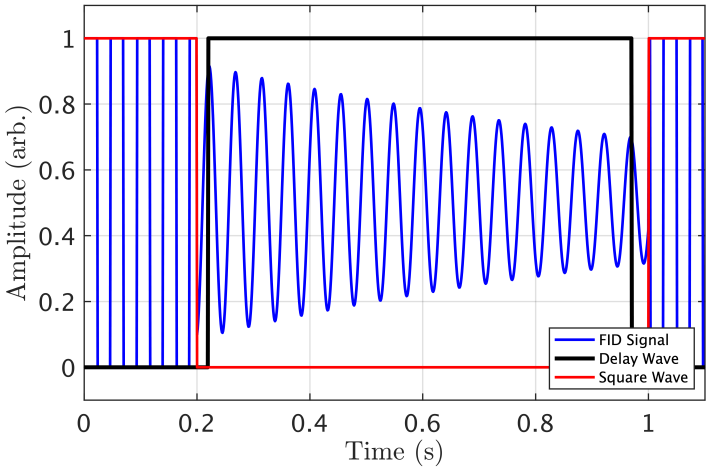

Figure 5.11: Simulated plot displaying the various signals which drive the experiment. The square wave (red) drives the cell heater. Synchronous modulation is applied during the pumping period, detecting an FID signal during the probe (blue). The black signal is a delayed wave with respect to the square signal. This is the gating period for the frequency counter measurement and is controlled by a DG535.

5.3.5 Results - FID Signal for Portable Sensor

The remainder of this section will demonstrate the performance of the compact FID sensor. The sensor was placed in a 3-layer μ-metal shield for its shielded sensitivity to be determined for each of the results to follow. Figure 5.12 shows an example absorption reference signal for the Cs D2 line (blue), compared with a similar MEMS cell to the one used in this experiment (red). The transitions shown are F=4 $\rightarrow$ F' and F=3 $\rightarrow$ F' from left to right.

Pumping on the F=3 groundstate transition is most effective as it permits more atoms to accumulate into a stretched Zeeman state. These are states where the m_F level is at its largest attainable value (m_F=F), with a higher atomic population in the stretched state realising more atoms precessing together in phase. Atoms which are excited to F' are redistributed to each groundstate transition upon decay. Pumping on F=3 results in atoms which spontaneously decay to F=3 being reintroduced to the optical pumping, eventually resulting in most atoms being distributed into F=4. Pumping on F=4, however, results in atoms which decay to F=3 being lost in the

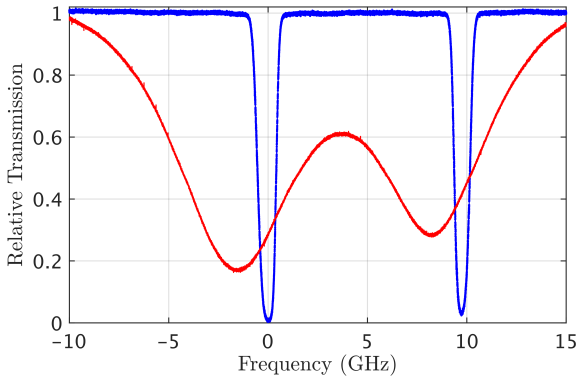

Figure 5.12: Example spectra of caesium's D2 line using a 75 mm reference cell (blue), compared with a MEMS cell similar to the one used in this experiment (red). The MEMS cell is 3 mm thick with an estimated 200 Torr of nitrogen included. Displayed from left to right is the F=4→F' and F=3→F' transitions.

optical pumping process. This is an effect widely known and implemented, with works including [123] publishing and discussing this. The pump laser is therefore tuned to F=3 for most optimal pumping in this experiment.

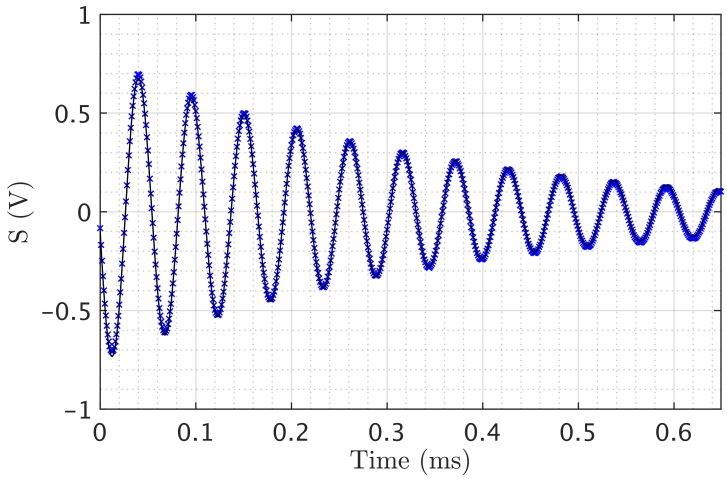

Figure 5.13: Example FID trace using the compact FID sensor with a decaying sinusoidal fit applied. The decay rate of the signal is 2.9 kHz.

An example FID signal for the portable sensor is shown in Figure 5.13. The external magnetic field was set to about 5 μT, resulting in a Larmor frequency of $2\pi\times18$ kHz (γ_g=3.5 kHz/μT [55]). Ideally, the Earth's field of 50 μT would be emulated in the

shield. A lower field was chosen due to magnetic gradients from imperfect coils within the shield. The gradient increased with higher field strengths and had an effect on the measurement parameters, where lower field operation mitigated more significant gradients. The pump light was synchronously modulated to correspond with the measured Larmor precession.

5.3.6 Results - Comparison of Data Extraction Methods

Comparison of the fitting regime and the frequency counter method was performed. Figure 5.14 displays example root-spectral density (RSD) performances of the magnetometer using post-process fitting against the frequency counter analysis. The total measurement time in each example was 1 ms, with a pumping period of 400 μs. One second of data was taken for each method, giving ~1000 frequencies in an array for the 1 kHz repetition rate of the experiment. One second of data gives a sensitivity estimation with a large error. Therefore, taking more independent one second measurements gives a more accurate measurement of the field with a lower associated error. A RSD was performed on the data to reveal the calculated sensitivity of the sensor. Comparison of the two methods with their resulting sensitivities is shown in Figure 5.14 below.

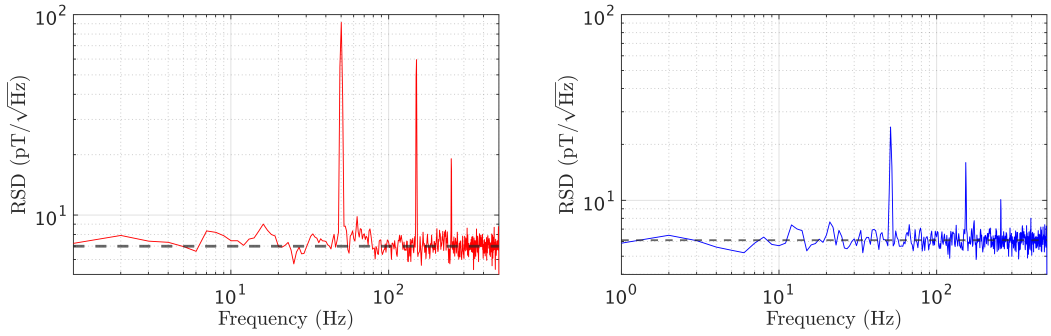

Figure 5.14: Comparing the calculated sensitivity of the sensor using the standard fitting regime and the frequency counter method. (a) The estimated sensitivity using the fitting method is 6.9 ± 0.60 pT/$\sqrt{Hz}$. (b) A value of 6.1 ± 0.70 pT/$\sqrt{Hz}$ is realised when employing the frequency counter. Both measurements were 1 second long and repeated 40 times for averaging.

Figure 5.14a, using the fitting method, calculated the magnetometer sensitivity to

be 6.9 ± 0.60 pT/$\sqrt{Hz}$. This matches extremely well with Figure 5.14b, which used the frequency counter for the measurement of ω_L, attaining an average sensitivity of 6.1 ± 0.70 pT/$\sqrt{Hz}$. This provides evidence that a frequency counter can replace the modelling method and in a much faster and simplistic way. For Figure 5.14a, the one second measurements were repeated 40 times for averaging. This is a computationally heavy task as the software uses iterative fitting to each FID signal to extract the Larmor frequency for each measurement. The frequency counter however records continuously for a set duration and can be averaged appropriately post measurement.

5.3.7 Results - Magnetometer Stability

The magnetometer described in this section has an eventual goal for portable demonstrations. The temporal characteristics of the sensor's sensitivity over long periods would therefore be useful for determining its capabilities in the field. A helpful tool for analysis to perceive this is an overlapping Allan deviation.

Allan deviations have been described and shown experimentally in Chapter 3. Here, instead of looking at the stability of an oscillator in terms of its frequency stability, an Allan deviation can be used to depict the stability of the magnetic field recordings of the sensor. This can help identify the noise sources inherent in the sensor as well as external factors which add to the measured magnetic noise. Additionally the σ_τ values calculated by the Allan deviation give a direct reading of the sensor's magnetic sensitivity at varying time scales.

Figure 5.15 displays an example overlapping Allan deviation of the recorded magnetic fields over a measurement period of around 15 minutes. A $1/\sqrt{\tau}$ fit shows the limiting noise in the experiment is white FM noise at around 1 second integration time. The measurement shows that the noise floor of the sensor is 9 pT at 2 seconds, before the magnetic stability begins to degrade and drift for the remainder of the measurement. The σ_τ value of 10 pT at 1 second integration matches reasonably well with the sensitivities calculated at this measurement time as shown in Section 5.3.6.

The early rise in the Allan deviation plot could be due to a number of factors. Although the sensor was in a magnetic shield, the caps of the shield could not be

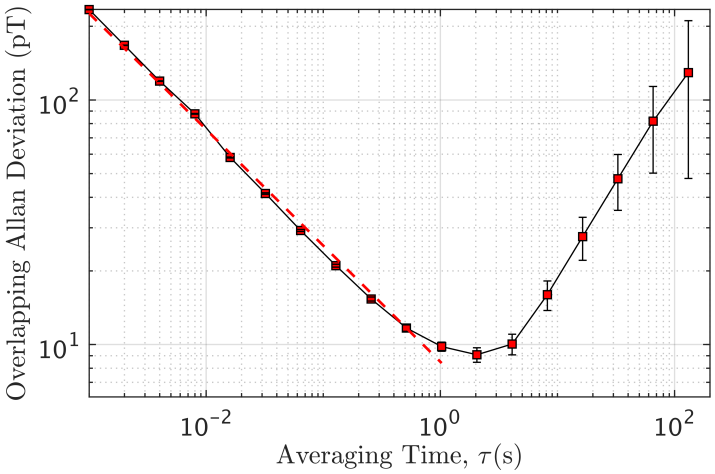

Figure 5.15: An overlapping Allan deviation to determine the magnetic stability. A $1/\sqrt{\tau}$ fit has been applied (dashed lines). The noise-floor of the magnetometer is 9 pT at two second integration time.

secured and the laboratory the sensor was measured in is extremely magnetically noisy. This would have manifested as real signal drift during the measurement, adversely affecting the stability of the magnetic field measurements. To mitigate this concern the sensor should be tested, unshielded, in a magnetically quiet environment such as in rural areas far from sources of magnetic noise. This requires the sensor and the various components which drive it to be portable, and is the next step in fully characterising the sensor. An important point to highlight is that the Flame is not frequency stabilised in these demonstrations as it is not required to be. The VCSEL was found to be much less versatile in the controlled temperature environment, the laser TEC needing tuned consistently over relatively short periods of time (every 30 minutes or so). Fluctuations of the probe frequency would have adverse effects on the measurement, such as light shift mechanisms and excess optical pumping during detection [111]. This could have contributed to the early drift in the Allan deviation plot. The VCSEL therefore needs to be stabilised to ensure that any degradation in the magnetic stability is not from laser frequency drifts of the probe laser. This can be done using far more simple methods than those mentioned in this thesis, as the stability of the lock can afford to drift by 100s of MHz due to the high presence of buffer gas. This is hoped to be achieved in

this project by stabilising the VCSEL TEC voltage to a PID control loop. Polarisation drift is another concern, where simply touching the optical fibre can cause changes to the FID signals. This is expected to be mitigated by extra fibre protection such as plastic cladding and housing.

For measurements at longer integration times, programming of the frequency counter is necessary. The frequency counter is capable of recording a maximum of 1M readings before ending a measurement on its internal memory. For the 1 kHz repetition rate of the experiment, the frequency counter reaches the maximum capacity of readings at 16.6 minutes. Interfacing with the frequency counter via Python through serial communication will permit the frequencies to be stored within the software and not the memory of the device, allowing for longer measurements.

5.3.8 Results - Field Switching

Synchronously modulating the atoms in the pump stage is a beneficial method for augmenting the spin-coherence. It is, however, a less valuable approach when the magnetic field to be measured is unknown or is varying in time. This makes the method ill-suited for portable and unshielded magnetic measurements. Instead, a field-switching approach [111] was implemented to replace the synchronous method. This technique actively improves the state preparation process by introducing a magnetic field along the optical-pumping axis. This significantly avoids the deflection of the atoms from the optical pumping axis caused by the transverse bias field, thereby ensuring more atoms are maintained and spin-polarised. Advantageously, this method could be applied to this specific sensor with minimal changes. A high magnetic field (100s of μT) was applied parallel to the beam propagation axis by implementing a pair of Helmholtz coils around the sensor-head. Synchronously modulating via the arbitrary waveform was then not necessary for this setup. Similarly to before, the field-switching coils were only active during pumping.

Figures 5.16a and 5.16b display an example FID signal and sensitivity measurement after employing field-switching coils. The sensitivity measurement was realised using the fitting method, and the frequency counter was not implemented in this example.

The amplitude of the signal increased by a factor of two compared to Figure 5.13 where synchronous modulation was implemented. The decay rate of the atoms also improved, decreasing from 2.9 kHz to 1.8 kHz using this refined spin-polarisation technique. Additionally, the sensitivity of the magnetometer was enhanced roughly by a factor of two, demonstrating 3 ± 0.3 $pT/\sqrt{Hz}$. The implementation of the field switching method has developed the sensor closer to sub-pT performance.

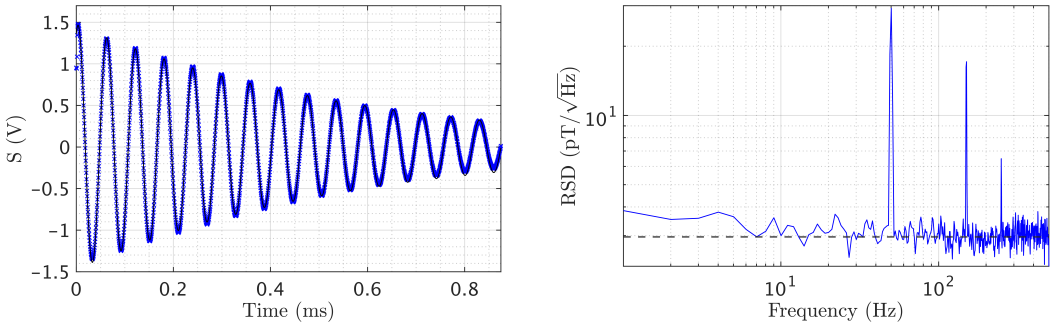

(a) (b)

Figure 5.16: An FID trace and sensitivity measurement to show the improvement of the sensor when switching from synchronously modulating the atoms to using a field switching approach [111]. (a) The amplitude of the FID trace has increased by a factor of two with decreased atomic decay rate when compared with Figure 5.13. (b) The sensitivity was calculated to be 3 ± 0.3 $pT/\sqrt{Hz}$, displaying a factor of two improvement.

5.3.9 Conclusion

In this section, we exhibited an accurate and compact FID sensor. We applied novel spin-polarising techniques to improve the initial sensitivity by a factor of two and explored improved data extraction methods using a frequency counter. Using a frequency counter, we were able to determine the magnetic stability of the magnetometer using overlapping Allan deviations. This analysis tool could eventually be implemented to compare the compact FID sensor to magnetometers operating in different configurations using the three-cornered hat method described in Chapter 3.

As a first-version, reaching a few $pT/\sqrt{Hz}$ sensitivity is considered a promising start, with the capabilities at this level making it suitable for measurements of Earth's

magnetic field. The next steps using this version of the sensor consist mostly of hardware organisation to condense the driving electronics for eventual portable use. Other improvements such as stabilising the probe laser and minimising polarisation drifts, as mentioned, are to be implemented.

It is believed that future iterations of the sensor will achieve even better performance by improving the engineering of the sensor head design, such as the alignment of the pump fibre input and its collimation. Rotation mounts for the QWP are additionally hoped to be designed to improve the process for achieving circular-light.

Chapter 6

Conclusion and Outlook

This thesis has aimed to characterise Alter's Flame module experimentally in applications pertaining to quantum technologies. The Flame's ability to be stabilised to within its own module finds the product most relevant in application areas which employ laser cooled atoms. It has been well covered in this thesis that such experiments require the laser to be extremely stable in frequency. To prove the efficacy of the Flame in this field area, it logically followed that the initial step was to test the frequency stability of the module. This provided the finding that the frequency stability of the module when locked to the internal spectroscopy was 5×10^{-12} at a 1 second integration time. This corresponds to kHz deviations in stability and demonstrated the viability of the Flame for a significant number of laser cooling applications.

Following from this, the laser was integrated into a deployable cold-atom system. This required condensing a conventionally large setup and rendering it portable. The additional advantage of this experiment lay in the opportunity to showcase the Flame alongside another commercial, quantum technology product in CPI-TMD's compact vacuum package. The overall system build was 60 cm L x 60 cm D x 90 cm H in size, occupying an 18U rack case. The system successfully powered and operated cold atoms in a portable manner in addition to demonstrating durability when exposed to low temperatures. Unforeseen electronic issues disrupted the deployment test, which caused the laser to unlock consistently.

Finally, Flame modules were tested as the laser source used in two optically pumped

magnetometer experiments. This was advantageous as it permitted for the laser to be tested in an alternative quantum sensing device. The first magnetometer discussed incorporated a 780 nm Flame laser and a MEMS cell of natural rubidium atoms as the sensing element. This sensor found pertinence in co-magnetometry applications, relevant in rotation sensing. It was however a complex setup with respect to understanding the optical pumping dynamics at play. Only one laser source was employed to function as both the pump and probe which is not optimal in mitigating power broadening and light shift mechanisms. The second sensor introduced an 852 nm Flame device and a caesium MEMS cell. Two laser sources were utilised to serve as the pump and probe beams, permitting for more optimal pumping and probing detuning frequencies. This developed sensor-head is extremely compact, 5 x 2.6 cm in size. The sensor was tested in shielded environments, exhibiting 3.0 $\pm$ 0.3 $pT/\sqrt{Hz}$ sensitivity performance. Since the conclusion of this thesis, this sensor has been tested in field measurements in Eskdalemuir Magnetic Observatory by a colleague. The results of this trial showed extremely promising results when compared to British Geological Survey's own magnetic measurement data and is expected to be published in the near future.

Quantum sensors in the literature frequently use fibred devices which inherently exhibit lower sensitivities to vibrations and mechanical disturbances. At present, Alter are in the process of fabricating fibre coupled Flame modules. In particular, future work includes trialling a fibre coupled Flame device in the portable MOT system built in this project. This will permit the modules in general to be integrated with existing quantum technology more effortlessly than the free-space modules used in this thesis, which were externally fibre-coupled for integration to each setup discussed.

Bibliography

[1] T. H. Maiman, "Stimulated Optical Radiation in Ruby," *Nature* **187**, 493–494 (1960).

[2] J. C. Camparo, "The Diode Laser in Atomic Physics," *Contemporary Physics* **26**, 443–477 (1985).

[3] T. W. Hänsch and A. L. Schawlow, "Cooling of gases by laser radiation," *Optics Communications* **13**, 68–69 (1975).

[4] W. D. Phillips and H. Metcalf, "Laser Deceleration of an Atomic Beam," *Physical Review Letters* **48**, 596 (1982).

[5] S. Chu, L. Hollberg, J. E. Bjorkholm, A. Cable and A. Ashkin, "Three-dimensional Viscous Confinement and Cooling of Atoms by Resonance Radiation Pressure," *Physical Review Letters* **55**, 48 (1985).

[6] A. L. Migdall, J. V. Prodan, W. D. Phillips, T. H. Bergeman and H. J. Metcalf, "First observation of magnetically trapped neutral atoms," *Physical Review Letters* **54**, 2596 (1985).

[7] E. L. Raab, M. Prentiss, A. Cable, S. Chu and D. E. Pritchard, "Trapping of Neutral Sodium Atoms with Radiation Pressure," *Physical Review Letters* **59**, 2631 (1987).

[8] G. Bevilacqua, V. Biancalana, P. Chessa and Y. Dancheva, "Multichannel optical atomic magnetometer operating in unshielded environment," *Applied Physics B* **122**, 1–9 (2016).

[9] Y. Bidel, O. Carraz, R. Charrière, M. Cadoret, N. Zahzam and A. Bresson, "Compact cold atom gravimeter for field applications," *Applied Physics Letters* **102**, 144107 (2013).

[10] C. L. Garrido Alzar, "Compact chip-scale guided cold atom gyrometers for inertial navigation: Enabling technologies and design study," *AVS Quantum Science* **1**, 014702 (2019).

[11] T. Kornack, R. Ghosh and M. V. Romalis, "Nuclear spin gyroscope based on an atomic comagnetometer," *Physical Review Letters* **95**, 230801 (2005).

[12] A. D. Ludlow, M. M. Boyd, J. Ye, E. Peik and P. O. Schmidt, "Optical atomic clocks," *Reviews of Modern Physics* **87**, 637 (2015).

[13] K. Lee, J. Kim, H. Noh and W. Jhe, "Single-beam atom trap in a pyramidal and conical hollow mirror," *Optics Letters* **21**, 1177–1179 (1996).

[14] C. Nshii, M. Vangeleyn, J. P. Cotter, P. F. Griffin, E. Hinds, C. N. Ironside, P. See, A. Sinclair, E. Riis and A. S. Arnold, "A surface-patterned chip as a strong source of ultracold atoms for quantum technologies," *Nature Nanotechnology* **8**, 321–324 (2013).

[15] J. P. Mcgilligan, K. Moore, A. Dellis, G. Martinez, E. de Clercq, P. Griffin, A. Arnold, E. Riis, R. Boudot and J. Kitching, "Laser cooling in a chip-scale platform," *Applied Physics Letters* **117**, 054001 (2020).

[16] S. Dyer, K. Gallacher, U. Hawley, A. Bregazzi, P. F. Griffin, A. S. Arnold, D. J. Paul, E. Riis and J. P. Mcgilligan, "Chip-Scale Packages for a Tunable Wavelength Reference and Laser Cooling Platform," *Physical Review Applied* **19**, 044015 (2023).

[17] O. S. Burrow, P. F. Osborn, E. Boughton, F. Mirando, D. P. Burt, P. F. Griffin, A. S. Arnold and E. Riis, "Stand-alone vacuum cell for compact ultracold quantum technologies," *Applied Physics Letters* **119**, 124002 (2021).

[18] N. Cooper, L. Coles, S. Everton, I. Maskery, R. Campion, S. Madkhaly, C. Morley, J. O'Shea, W. Evans, R. Saint, P. Krüger, F. Oručević, C. Tuck, R. Wildman, T. Fromhold and L. Hackermüller, "Additively manufactured ultra-high vacuum chamber for portable quantum technologies," *Additive Manufacturing* **40**, 101898 (2021).

[19] R. N. Hall, G. E. Fenner, J. Kingsley, T. Soltys and R. Carlson, "Coherent light emission from GaAs junctions," *Physical Review Letters* **9**, 366 (1962).

[20] M. I. Nathan, W. P. Dumke, G. Burns, F. H. Dill Jr and G. Lasher, "Stimulated emission of radiation from GaAs p-n junctions," *Applied Physics Letters* **1**, 62–64 (1962).

[21] C. E. Wieman and L. Hollberg, "Using diode lasers for atomic physics," *Review of Scientific Instruments* **62**, 1 (1991).

[22] H. Nasim and Y. Jamil, "Diode lasers: From laboratory to industry," *Optics & Laser Technology* **56**, 211–222 (2014).

[23] J. McGilligan, K. Gallacher, P. Griffin, D. Paul, A. Arnold and E. Riis, "Micro-fabricated components for cold atom sensors," *Review of Scientific Instruments* **93**, 091101 (2022).

[24] S. D. Saliba and R. E. Scholten, "Linewidths below 100 kHz with external cavity diode lasers," *Applied Optics* **48**, 6961–6966 (2009).

[25] C. Wieman, G. Flowers and S. Gilbert, "Inexpensive laser cooling and trapping experiment for undergraduate laboratories," *American Journal of Physics* **63**, 317–330 (1995).

[26] J. Kitching, "Chip-scale atomic devices," *Applied Physics Reviews* **5**, 3 (2018).

[27] N. Heine, J. Matthias, M. Sahelgozin, W. Herr, S. Abend, L. Timmen, J. Müller and E. M. Rasel, "A transportable quantum gravimeter employing delta-kick collimated Bose–Einstein condensates," *The European Physical Journal D* **74**, 1–8 (2020).

[28] V. Ménoret, P. Vermeulen, N. L. Moigne, S. Bonvalot, P. Bouyer, A. Landragin and B. Desruelle, "Gravity measurements below 109 g with a transportable absolute quantum gravimeter," *Scientific Reports* **8**, 12300 (2018).

[29] F. Theron, Y. Bidel, E. Dieu, N. Zahzam, M. Cadoret and A. Bresson, "Frequency-doubled telecom fiber laser for a cold atom interferometer using optical lattices," *Optics Communications* **393**, 152–155 (2017).

[30] F. Lienhart, S. Boussen, O. Carraz, N. Zahzam, Y. Bidel and A. Bresson, "Compact and robust laser system for rubidium laser cooling based on the frequency doubling of a fiber bench at 1560 nm," *Applied Physics B* **89**, 177–180 (2007).

[31] N. Almat, M. Pellaton, W. Moreno, F. Gruet, C. Affolderbach and G. Mileti, "Rb vapor-cell clock demonstration with a frequency-doubled telecom laser," *Applied Optics* **57**, 4707–4713 (2018).

[32] P. Ripley, "The physics of diode lasers," *Lasers in Medical Science* **11**, 71–78 (1996).

[33] A. Yariv, P. Yeh and A. Yariv, *Photonics: optical electronics in modern communications*, vol. 6, Oxford university press New York (2007).

[34] A. Arnold, J. Wilson and M. Boshier, "A simple extended-cavity diode laser," *Review of Scientific Instruments* **69**, 1236–1239 (1998).

[35] A. L. Schawlow and C. H. Townes, "Infrared and optical masers," *Physical Review* **112**, 1940 (1958).

[36] A. E. Siegman, *Lasers*, University Science Books, Mill Valley, California (1986).

[37] C. Henry, "Theory of the linewidth of semiconductor lasers," *IEEE Journal of Quantum Electronics* **18**, 259–264 (1982).

[38] Y. Yu, G. Giuliani and S. Donati, "Measurement of the linewidth enhancement factor of semiconductor lasers based on the optical feedback self-mixing effect," *IEEE Photonics Technology Letters* **16**, 990–992 (2004).

[39] G. Liu, X. Jin and S.-L. Chuang, "Measurement of linewidth enhancement factor of semiconductor lasers using an injection-locking technique," *IEEE photonics Technology letters* **13**, 430–432 (2001).

[40] S.-L. Lee, D. A. Tauber, V. Jayaraman, M. Heimbuch, L. Coldren and J. E. Bowers, "Dynamic responses of widely tunable sampled grating DBR lasers," *IEEE Photonics Technology Letters* **8**, 1597–1599 (1996).

[41] M. Fleming and A. Mooradian, "Spectral characteristics of external-cavity controlled semiconductor lasers," *IEEE Journal of Quantum Electronics* **17**, 44–59 (1981).

[42] Y. Li, T. Ido, T. Eichler and H. Katori, "Narrow-line diode laser system for laser cooling of strontium atoms on the intercombination transition," *Applied Physics B: Lasers and Optics* **78**, 315–320 (2004).

[43] A. Daffurn, R. F. Offer and A. S. Arnold, "A simple, powerful diode laser system for atomic physics," *Applied Optics* **60**, 5832–5836 (2021).

[44] S. Kraft, A. Deninger, C. Trück, J. Fortágh, F. Lison and C. Zimmermann, "Rubidium spectroscopy at 778–780 nm with a distributed feedback laser diode," *Laser Physics Letters* **2**, 71 (2004).

[45] E. Di Gaetano, S. Watson, E. McBrearty, M. Sorel and D. Paul, "Sub-megahertz linewidth 780.24 nm distributed feedback laser for 87 Rb applications," *Optics Letters* **45**, 3529–3532 (2020).

[46] V. Jayaraman, A. Mathur, L. Coldren and P. Dapkus, "Extended tuning range in sampled grating DBR lasers," *IEEE Photonics Technology Letters* **5**, 489–491 (1993).

[47] S. Lee, M.-S. Heo, T. Y. Kwon, H.-G. Hong, S.-B. Lee, A. P. Hilton, A. N. Luiten, J. G. Hartnett and S. E. Park, "Operating atomic fountain clock using robust DBR laser: short-term stability analysis," *IEEE Transactions on Instrumentation and Measurement* **66**, 1349–1354 (2017).

[48] Z. L. Newman, V. Maurice, T. Drake, J. R. Stone, T. C. Briles, D. T. Spencer, C. Fredrick, Q. Li, D. Westly, B. R. Ilic, B. Shen, M.-G. Suh, K. Y. Yang, C. Johnson, D. M. S. Johnson, L. Hollberg, K. J. Vahala, K. Srinivasan, S. A. Diddams, J. Kitching, S. B. Papp and M. T. Hummon, "Architecture for the photonic integration of an optical atomic clock," *Optica* **6**, 680–685 (2019).

[49] U. Feiste, "Optimization of modulation bandwidth in DBR lasers with detuned Bragg reflectors," *IEEE Journal of Quantum Electronics* **34**, 2371–2379 (1998).

[50] O. Arnon and P. Baumeister, "Electric field distribution and the reduction of laser damage in multilayers," *Applied Optics* **19**, 1853–1855 (1980).

[51] TFCalc, "TFCalc Demo and Manual," `https://www.sspectra.com/demo.html` (2016). Accessed: January 2024.

[52] P. Siddons, C. S. Adams, C. Ge and I. G. Hughes, "Absolute absorption on rubidium D lines: comparison between theory and experiment," *Journal of Physics B: Atomic, Molecular and Optical Physics* **41**, 155004 (2008).

[53] D. A. Steck, "Rubidium 87 D Line Data," `https://steck.us/alkalidata` (2001). Version 2.3.3.

[54] D. A. Steck, "Rubidium 85 D Line Data," `https://steck.us/alkalidata` (2008). Version 2.3.3.

[55] D. A. Steck, "Cesium D Line Data," `https://steck.us/alkalidata` (2003). Version 2.3.3.

[56] U. Volz and H. Schmoranzer, "Precision lifetime measurements on alkali atoms and on helium by beam–gas–laser spectroscopy," *Physica Scripta* **1996**, 48 (1996).

[57] D. W. Preston, "Doppler-free saturated absorption: Laser spectroscopy ," *Journal of Physics* **64**, 1432–1436 (1996).

[58] K. L. Corwin, Z.-T. Lu, C. F. Hand, R. J. Epstein and C. E. Wieman, "Frequency-stabilized diode laser with the Zeeman shift in an atomic vapor," *Applied Optics* **37**, 3295–3298 (1998).

[59] D. McCarron, S. King and S. Cornish, "Modulation transfer spectroscopy in atomic rubidium," *Measurement science and technology* **19**, 105601 (2008).

[60] C. Wieman and T. W. Hänsch, "Doppler-free laser polarization spectroscopy," *Physical Review Letters* **36**, 1170 (1976).

[61] J. H. Shirley, "Modulation transfer processes in optical heterodyne saturation spectroscopy," *Optics Letters* **7**, 537–539 (1982).

[62] C. Pearman, C. Adams, S. Cox, P. Griffin, D. Smith and I. Hughes, "Polarization spectroscopy of a closed atomic transition: applications to laser frequency locking," *Journal of Physics B: Atomic, Molecular and Optical Physics* **35**, 5141 (2002).

[63] J. D. Elgin, T. P. Heavner, J. Kitching, E. A. Donley, J. Denney and E. A. Salim, "A cold-atom beam clock based on coherent population trapping," *Applied Physics Letters* **115**, 3 (2019).

[64] B. Xu, X. Chen, J. Wang and M. Zhan, "Realization of a single-beam mini magneto-optical trap: A candidate for compact CPT cold atom-clocks," *Optics Communications* **281**, 5819–5823 (2008).

[65] E. Blanshan, S. Rochester, E. Donley and J. Kitching, "Light shifts in a pulsed cold-atom coherent-population-trapping clock," *Physical Review A* **91**, 041401 (2015).

[66] S. Rosi, A. Burchianti, S. Conclave, D. S. Naik, G. Roati, C. Fort and F. Minardi, "λ-enhanced grey molasses on the D2 transition of Rubidium-87 atoms," *Scientific Reports* **8**, 1301 (2018).

[67] V. Schkolnik, O. Hellmig, A. Wenzlawski, J. Grosse, A. Kohfeldt, K. Döringshoff, A. Wicht, P. Windpassinger, K. Sengstock, C. Braxmaier, M. Krutzik and A. Peters, "A compact and robust diode laser system for atom interferometry on a sounding rocket," *Applied Physics B: Lasers and Optics* **122**, 1–8 (2016).

[68] T. Müller, T. Wendrich, M. Gilowski, C. Jentsch, E. Rasel and W. Ertmer, "Versatile compact atomic source for high-resolution dual atom interferometry," *Physical Review A* **76**, 063611 (2007).

[69] A. E. Siegman, "Defining, measuring, and optimizing laser beam quality," *Laser Resonators and Coherent Optics: Modeling, Technology, and Applications* **1868**, 2–12 (1993).

[70] C. Affolderbach and G. Mileti, "A compact laser head with high-frequency stability for Rb atomic clocks and optical instrumentation," *Review of Scientific Instruments* **76**, 7 (2005).

[71] A. Strangfeld, B. Wiegand, J. Kluge, M. Schoch and M. Krutzik, "Compact plug and play optical frequency reference device based on Doppler-free spectroscopy of rubidium vapor," *Optics Express* **30**, 12039–12047 (2022).

[72] C. Affolderbach and G. Mileti, "Tuneable, stabilised diode lasers for compact atomic frequency standards and precision wavelength references," *Optics and Lasers in Engineering* **43**, 291–302 (2005).

[73] F. Gruet, M. Pellaton, C. Affolderbach, T. Bandi, R. Matthey and G. Mileti, "Compact and frequency stabilized laser heads for rubidium atomic clocks," in *International Conference on Space Optics—ICSO 2012*, **10564**, 756–761, SPIE (2017).

[74] A. Strangfeld, S. Kanthak, M. Schiemangk, B. Wiegand, A. Wicht, A. Ling and M. Krutzik, "Prototype of a compact rubidium-based optical frequency reference for operation on nanosatellites," *Journal of the Optical Society of America B* **38**, 1885–1891 (2021).

[75] Vescent Photonics, "Saturated Absorption Spectroscopy Module," `https://vescent.com/gb/d2-210-saturated-absorption-spectroscopy-module.html` (2023). Accessed: December 2023.

[76] TEM Messtechnik, "CoSy – Doppler-free Absorption Saturation Spectroscopy," `https://tem-messtechnik.de/en/products/` (2023). Accessed: December 2023.

[77] S. H. Madkhaly, N. Cooper, L. Coles and L. Hackermüller, "High-performance, additively-manufactured atomic spectroscopy apparatus for portable quantum technologies," *Optics Express* **30**, 25753 (2022).

[78] W. Liang, V. S. Ilchenko, D. Eliyahu, E. Dale, A. A. Savchenkov, D. Seidel, A. B. Matsko and L. Maleki, "Compact stabilized semiconductor laser for frequency metrology," *Applied Optics* **54**, 3353 (2015).

[79] D. W. Allan, "Statistics of atomic frequency standards," *Proceedings of the IEEE* **54**, 221–230 (1966).

[80] W. Riley and D. Howe, "Handbook of Frequency Stability Analysis," Special Publication (NIST SP), National Institute of Standards and Technology, Gaithersburg, MD. [online] `https://tsapps.nist.gov/publication/get_pdf.cfm?pub_id=50505` (2008). Accessed: January 2024.

[81] J. E. Gray and D. W. Allan, "A method for estimating the frequency stability of an individual oscillator," in *28th Annual Symposium on Frequency Control*, 243–246, IEEE (1974).

[82] IEEE-UFFC-S, "Welcome to the Stable32 Web Site," `http://www.stable32.com` (2020). Accessed: December 2023.

[83] G. Barwood, P. Gill and W. Rowley, "An optically narrowed diode laser for Rb saturation spectroscopy," *Journal of Modern Optics* **37**, 749–758 (1990).

[84] M. Vangeleyn, P. F. Griffin, E. Riis and A. S. Arnold, "Single-laser, one beam, tetrahedral magneto-optical trap," *Optics Express* **17**, 13601–13608 (2009).

[85] J. Rushton, M. Aldous and M. Himsworth, "Contributed review: The feasibility of a fully miniaturized magneto-optical trap for portable ultracold quantum technology," *Review of Scientific Instruments* **85**, 12 (2014).

[86] CPI, "Products - Quantum Technology," `https://www.cpii.com/product.cfm/16/169` (2023). Accessed: December 2023.

[87] Thorlabs, "Mini-Series Optical Post Assemblies," `https://www.thorlabs.com/navigation.cfm?guide_id=2249` (2023). Accessed: December 2023.

[88] W. R. McGehee, W. Zhu, D. S. Barker, D. Westly, A. Yulaev, N. Klimov, A. Agrawal, S. Eckel, V. Aksyuk and J. J. McClelland, "Magneto-optical trapping using planar optics," *New Journal of Physics* **23**, 013021 (2021).

[89] J. Duan, X. Liu, Y. Zhou, X.-B. Xu, L. Chen, C.-L. Zou, Z. Zhu, Z. Yu, N. Ru and J. Qu, "High diffraction efficiency grating atom chip for magneto-optical trap," *Optics Communications* **513**, 128087 (2022).

[90] R. W. Moore, L. A. Lee, E. A. Findlay, L. Torralbo-Campo, G. D. Bruce and D. Cassettari, "Measurement of vacuum pressure with a magneto-optical trap: A pressure-rise method," *Review of Scientific Instruments* **86**, 9 (2015).

[91] T. Arpornthip, C. A. Sackett and K. J. Hughes, "Vacuum-pressure measurement using a magneto-optical trap," *Physical Review A - Atomic, Molecular, and Optical Physics* **85**, 3 (2012).

[92] Koheron, "Laser Drivers," `https://www.koheron.com/laser-drivers/` (2024). Accessed: January 2024.

[93] B. Wiegand, B. Leykauf, R. Jördens and M. Krutzik, "Linien: A versatile, user-friendly, open-source FPGA-based tool for frequency stabilization and spectroscopy parameter optimization," *Review of Scientific Instruments* **93**, 6 (2022).

[94] C. Myatt, N. Newbury and C. Wieman, "Simplified atom trap by using direct microwave modulation of a diode laser," *Optics letters* **18**, 649–651 (1993).

[95] J. Vovrosh, K. Wilkinson, S. Hedges, K. McGovern, F. Hayati, C. Carson, A. Selyem, J. Winch, B. Stray, L. Earl, H. Maxwell, G. Wilson, S. Seedat, A amd Roshanmanesh, K. Bongs and M. Holynski, "Magneto-optical trapping in a near-suface borehole," *Plos One* **18**, 7 (2023).

[96] Q. Luo, H. Zhang, K. Zhang, X.-C. Duan, Z.-K. Hu, L.-L. Chen and M.-K. Zhou, "A compact laser system for a portable atom interferometry gravimeter," *Review of Scientific Instruments* **90**, 4 (2019).

[97] L. Earl, J. Vovrosh, M. Wright, D. Roberts, J. Winch, M. Perea-Ortiz, A. Lamb, F. Hayati, P. Griffin, N. Metje, K. Bongs and M. Holynski, "Demonstration of a Compact Magneto-Optical Trap on an Unstaffed Aerial Vehicle," *Atoms* **10**, 32 (2022).

[98] A. Hinton, M. Perea-Ortiz, J. Winch, J. Briggs, S. Freer, D. Moustoukas, S. Powell-Gill, C. Squire, A. Lamb, C. Rammeloo, B. Stray, G. Voulazeris, L. Zhu, A. Kaushik, Y. Lien, A. Niggebaum, A. Rodgers, A. Stabrawa, D. Boddice, S. Plant, G. Tuckwell, K. Bongs, N. Metje and M. Holynski, "A portable magneto-optical trap with prospects for atom interferometry in civil engineering," *Philosophical Transactions of the Royal Society A: Mathematical, Physical and Engineering Sciences* **375**, 20160238 (2017).

[99] F. Theron, O. Carraz, G. Renon, N. Zahzam, Y. Bidel, M. Cadoret and A. Bresson, "Narrow linewidth single laser source system for onboard atom interferometry," *Applied Physics B* **118**, 1–5 (2015).

[100] J. Rudolph, W. Herr, C. Grzeschik, T. Sternke, A. Grote, M. Popp, D. Becker, H. Müntinga, H. Ahlers, A. Peters *et al.*, "A high-flux BEC source for mobile atom interferometers," *New Journal of Physics* **17**, 065001 (2015).

[101] Y. B. Kale, A. Singh, M. Gellesch, J. M. Jones, D. Morris, M. Aldous, K. Bongs and Y. Singh, "Field deployable atomics package for an optical lattice clock," *Quantum Science and Technology* **7**, 045004 (2022).

[102] T. Scholtes, S. Woetzel, R. IJsselsteijn, V. Schultze and H.-G. Meyer, "Intrinsic relaxation rates of polarized Cs vapor in miniaturized cells," *Applied Physics B* **117**, 211–218 (2014).

[103] S. J. Seltzer, *Developments in alkali-metal atomic magnetometry.* PhD thesis, Princeton University (2008).

[104] H. Dang, A. C. Maloof and M. V. Romalis, "Ultrahigh sensitivity magnetic field and magnetization measurements with an atomic magnetometer," *Applied Physics Letters* **97**, 15 (2010).

[105] B. Patton, E. Zhivun, D. C. Hovde and D. Budker, "All-optical vector atomic magnetometer," *Physical Review Letters* **113**, 013001 (2014).

[106] M. E. Limes, E. L. Foley, T. W. Kornack, S. Caliga, S. McBride, A. Braun, W. Lee, V. G. Lucivero and M. V. Romalis, "Portable Magnetometry for Detection of Biomagnetism in Ambient Environments," *Physical Review Applied* **14**, 011002 (2020).

[107] I. K. Kominis, T. W. Kornack, J. C. Allred and M. V. Romalis, "A subfemtotesla multichannel atomic magnetometer," *Nature* **422**, 596–599 (2003).

[108] J. Osborne, J. Orton, O. Alem and V. Shah, "Fully integrated standalone zero field optically pumped magnetometer for biomagnetism," in *Steep dispersion engineering and opto-atomic precision metrology XI*, **10548**, 89–95, SPIE (2018).

[109] I. M. Savukov, S. Seltzer, M. Romalis and K. Sauer, "Tunable atomic magnetometer for detection of radio-frequency magnetic fields," *Physical review letters* **95**, 063004 (2005).

[110] C. Deans, L. Marmugi, S. Hussain and F. Renzoni, "Electromagnetic induction imaging with a radio-frequency atomic magnetometer," *Applied Physics Letters* **108**, 103503 (2016).

[111] D. Hunter, M. S. Mrozowski, A. McWilliam, S. J. Ingleby, T. E. Dyer, P. F. Griffin and E. Riis, "Free-induction-decay magnetometer with enhanced optical pumping," *arXiv preprint arXiv:2307.11600* (2023).

[112] V. Gerginov, M. Pomponio and S. Knappe, "Scalar magnetometry below 100 $fT/\sqrt{Hz}$ in a microfabricated cell," *IEEE Sensors Journal* **20**, 12684–12690 (2020).

[113] D. Sheng, A. Kabcenell and M. V. Romalis, "New Classes of Systematic Effects in Gas Spin Comagnetometers," *Physics Review Letters* **113**, 163002 (2014).

[114] Y. Ding, W. Xiao, Y. Zhao, T. Wu, X. Peng and H. Guo, "Dual-Species All-Optical Magnetometer Based on a Cs-K Hybrid Vapor Cell," *Physics Review Applied* **19**, 034066 (2023).

[115] J. E. Dhombridge, N. R. Claussen, J. Iivanainen and P. D. Schwindt, "High-sensitivity rf detection using an optically pumped comagnetometer based on natural-abundance rubidium with active ambient-field cancellation," *Physical Review Applied* **18**, 044052 (2022).

[116] H. Yang, Y. Wang and N. Zhao, "Manipulation of spin polarization of rubidium atoms by optical pumping with both D1 and D2 beams," *The European Physical Journal D* **74**, 1–5 (2020).

[117] Z. Wang, X. Peng, R. Zhang, H. Luo, J. Li, Z. Xiong, S. Wang and H. Guo, "Single-Species Atomic Comagnetometer Based on Rb 87 Atoms," *Physical Review Letters* **124**, 193002 (2020).

[118] Y. Yang, T. Wu, J. Chen, X. Peng and H. Guo, "All-optical single-species cesium atomic comagnetometer with optical free induction decay detection," *Applied Physics B* **127**, 1–11 (2021).

[119] S. Dyer, A. McWilliam, D. Hunter, S. Ingleby, D. Burt, O. Sharp, F. Mirando, P. Griffin, E. Riis and J. McGilligan, "Nitrogen buffer gas pressure tuning in a micro-machined vapor cell," *Applied Physics Letters* **123**, 7 (2023).

[120] S. Ingleby, P. Griffin, T. Dyer, M. Mrozowski and E. Riis, "A digital alkali spin maser," *Scientific Reports* **12**, 12888 (2022).

[121] R. Dawson, C. O'Dwyer, M. S. Mrozowski, E. Irwin, J. P. McGilligan, D. P. Burt, D. Hunter, S. Ingleby, M. Rea, N. Holmes, M. J. Brookes, P. F. Griffin and E. Riis, "Portable single-beam cesium zero-field magnetometer for magnetocardiography," *Journal of Optical Microsystems* **3**, 044501–044501 (2023).

[122] W. E. Bell and A. L. Bloom, "Optically driven spin precession," *Physical Review Letters* **6**, 280 (1961).

[123] T. Scholtes, V. Schultze, R. IJsselsteijn, S. Woetzel and H.-G. Meyer, "Light-narrowed optically pumped Mx magnetometer with a miniaturized Cs cell," *Physical Review A* **84**, 043416 (2011).